Radiation hardness of superconducting magnet insulation materials for FAIR

Strahlenhärte von Isolationsmaterialien der supraleitenden Magnete für FAIR

Vom Fachbereich Material- und Geowissenschaften der Technischen Universität Darmstadt

zur Erlangung des akademischen Grades eines Doktors der Naturwissenschaften (Dr. rer. nat.) genehmigte Dissertation von Tim Seidl (Dipl.-Chem.) aus Gelnhausen

März 2013 – Darmstadt – D17

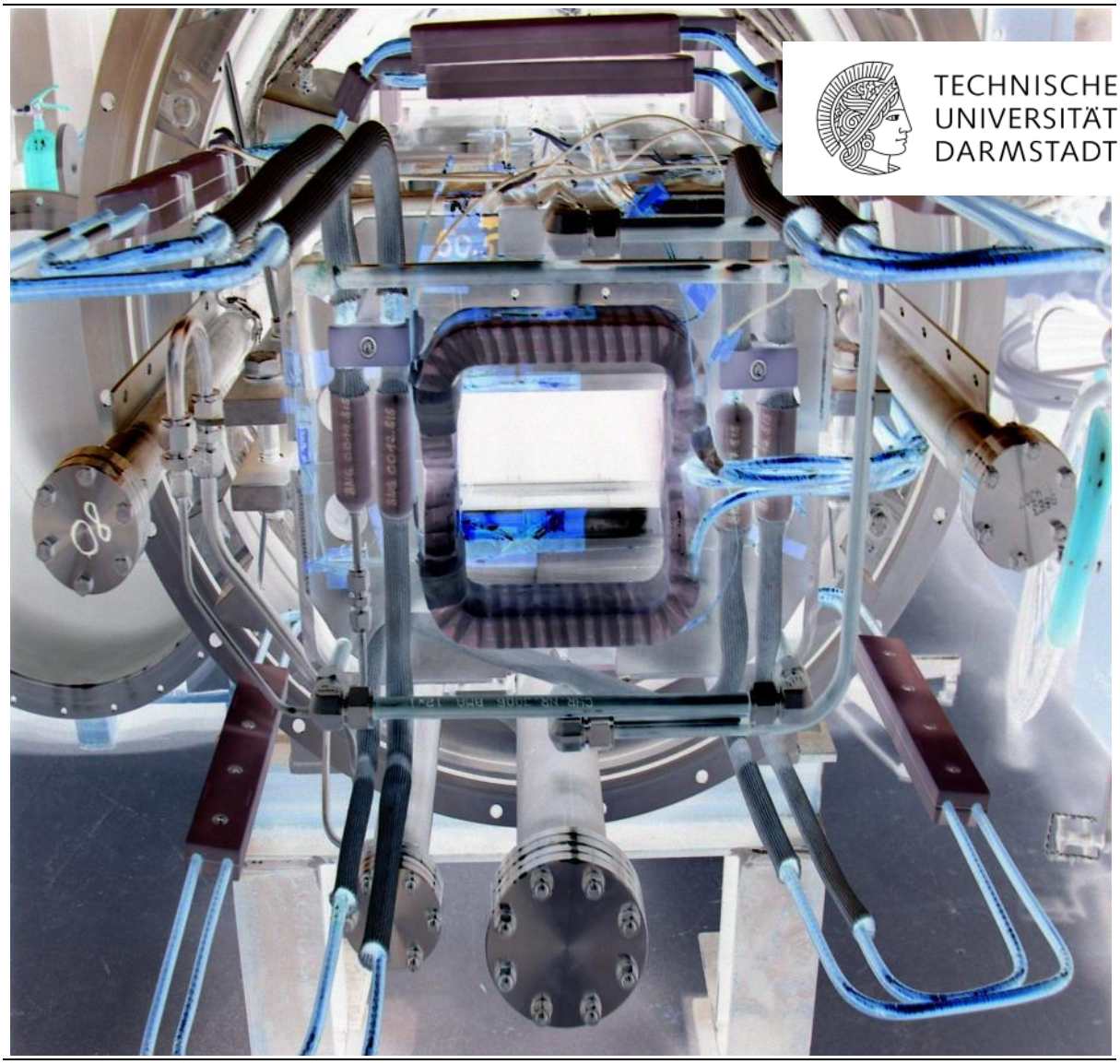

Radiation hardness of superconducting magnet insulation materials for FAIR

Strahlenhärte von Isolationsmaterialien der supraleitenden Magnete für FAIR

Dem Fachbereich Geo- und Materialwissenschaften der Technischen Universität Darmstadt vorgelegte Dissertation von Tim Seidl aus Gelnhausen

1. Gutachten: Prof. Dr. Wolfgang Ensinger
2. Gutachten: Prof. Dr. Christina Trautmann

Tag der Einreichung: 19.12.2012

Tag der Prüfung: 18.02.2013

Darmstadt – D 17

Erklärung zur Dissertation

Hiermit versichere ich, die vorliegende Dissertation ohne Hilfe Dritter nur mit den angegebenen Quellen und Hilfsmitteln angefertigt zu haben. Alle Stellen, die aus Quellen entnommen wurden, sind als solche kenntlich gemacht. Diese Arbeit hat in gleicher oder ähnlicher Form noch keiner Prüfungsbehörde vorgelegt.

Darmstadt, den 23.02.2013

_____

(Tim Seidl)

Abstract

This thesis focuses on radiation degradation studies of polyimide, polyepoxy/glass-fiber composites and other technical components used, for example, in the superconducting magnets of new ion accelerators such as the planned *International Facility for Antiproton and Ion Research* (FAIR) at the *GSI Helmholtz Center of Heavy Ion Research* (GSI) in Darmstadt. As accelerators are becoming more powerful, i.e., providing larger energies and beam intensities, the potential risk of radiation damage to the components increases. Reliable data of the radiation hardness of accelerator materials and components concerning electrical, thermal and other technical relevant properties are of great interest also for other facilities such as the Large Hadron Collider (LHC) of CERN.

Dependent on the position of the different components, induced radiation due to beam losses consists of a cocktail of gammas, neutrons, protons, and heavier particles. Although the number of heavy fragments of the initial projectiles is small compared to neutrons, protons, or light fragments (e.g. α particles), their large energy deposition can induce extensive damage at rather low fluences (dose calculations show that the contribution of heavy ions to the total accumulated dose can reach 80 %). For this reason, defined radiation experiments were conducted using different energetic ion beams (from protons to uranium) and gamma radiation from a Co-60 source. The induced changes were analyzed by means of in-situ and ex-situ analytical methods, e.g. ultraviolet-visible and infrared spectroscopy, residual gas analysis, thermal gravimetric analysis, dielectric strength measurements, measurements of low temperature thermal properties, and performance tests. In all cases, the radiation induces a change in molecular structure as well as loss of functional material properties. The amount of radiation damage is found to be sensitive to the used type of ionizing radiation and the long term stability of the materials is discussed within the focus of its application.

Zusammenfassung

Thema dieser Arbeit sind Bestrahlungsstudien an Polyimid, Polyepoxy/Glasfaser-Kompositen und anderen technischen Komponenten, die in supraleitenden Magneten neuer Teilchenbeschleunigern wie der geplanten *International Facility for Antiproton and Ion Research* (FAIR) am *GSI Helmholtz Center of Heavy Ion Research* (GSI) in Darmstadt ihren Einsatz finden. Durch den Zuwachs an Energie und Intensität von zukünftigen Teilchenbeschleunigern erhöht sich das potentielle Risiko von Strahlenschäden in diversen Beschleunigerkomponenten. Zuverlässige Daten über die Strahlenresistenz von Materialien und Komponenten hinsichtlich technisch relevanter Eigenschaften sind auch für andere Beschleunigerzentren wie z.B. den Large Hadron Collider (LHC) des CERNs von zentraler Bedeutung.

Abhängig von der Position der verwendeten Bauteile induzieren Strahlverluste eine Strahlenbelastung bestehend aus einer Mischung von Gammas, Neutronen, Protonen, und schweren Partikeln. Die schweren Partikel induzieren extensiven Schaden bei relativ niedriger Fluenz, obwohl ihre Anzahl im Vergleich zu leichteren Partikeln klein ist (Dosisrechnungen zeigen, dass der Anteil der durch Sekundärstrahlung induzierten Dosis bis zu 80 % betragen kann). Aus diesem Grund wurden definierte Bestrahlungsexperimente mit energetischen Ionenstrahlen (von Protonen bis Uran) und Gammastrahlung aus einer Co-60 Quelle durchgeführt. Die Analyse der induzierten Materialänderungen erfolgte mittels verschiedener in-situ und ex-situ Methoden, wie UV/Vis- und Infrarotspektroskopie, Restgasanalyse, Thermogravimetrischer Analyse, Durchschlagsspannungs-Messungen, Messungen der thermischen Eigenschaften bei tiefen Temperaturen und Funktionstests. In allen Fällen führte die Bestrahlung zu einer Veränderung der molekularen Zusammensetzung und einem Verlust an funktionellen Eigenschaften, wobei die Stärke der induzierten Veränderungen sensitiv zur Art der ionisierenden Strahlung ist. Die erhaltenen Ergebnisse werden im Fokus zur Applikation diskutiert.

CONTENTS

Abbreviations

AC	Alternating Current (In European Union a line frequency of 50 Hz is standard whereas in the Northern American Area 60 Hz is used)
AGOT	Type of Nuclear Graphite from the *National Carbon Company*
ASTM	Analytical Thermal Spike Model
ATR	Attenuated Total Reflection
BADCY	Bisphenol-A-dicyante
CERN	“Conseil Européen pour la Recherche Nucléaire” European Organization for Nuclear Research, Geneva, Swizz
CR	Cryogenics
C(N)T/C(N)T´s	Carbonanotubes
CTD	Composite Technology Development, Inc.
DC	Direct Current
DETDA	Diethyl-toluol-diamine
DGEBF	Diglycidylether of Bisphenol F
DS	Dielectric Strength
EGA	Evolved Gas Analysis
FAIR	Facility for Antiproton and Ion Research
Formvar™	Polyvinyl formal
FRP	Fiber reinforced plastics
G10 (CR)	Standard for glass fiber reinforced polyepoxy given by National Electrical Manufacturers Society
G11 (CR)	Standard for glass fiber reinforced polyepoxy given by National Electrical Manufacturers Society
GANIL	Grand Accélérateur National d'Ions Lourds (Caen, France)
GC	Gas Chromatography
GFRP	Glass fiber reinforced plastic
GSI	GSI Helmholtz Center of Heavy Ion Research (Darmstadt, Germany)
HMI	Hahn Meitner Institute in Berlin
IHEP	Institute of High Energy Physics, Chinese Academy of Sciences
IR	Infrared

ISL	Ionenstrahllabor (Ion beam laboratory) existing at the Hahn Meitner Institute (HMI) at Berlin. End of operation in 2006.
ITEP	Institute for Theoretical and Experimental Physics (Moscow, Russia)
ITER	International Thermonuclear Experimental Reactor
ITSM	Inelastic Thermal Spike Model
JINR	Joint Institute for Nuclear Research in Dubna/Russia
MPS	Methacryloxypropyltrimethoxy-silane
MS	Mass Spectrometry
NEMA	National Electrical Manufacturers Society
NIST	National Institute for Standards and Technology
ODA	Oxydianiline
PC	Polycarbonate
PE	Polyethylene
PET	Polyethylene terephthalate
PI	Polyimide
PMDA	Pyromellitic dianhydrid
PTFE	Polytetrafluoroethylene
PVA	Polyvinyl alcohol
PVDF	Polyvinylidene Fluoride
QMS	(Quadrupole) Mass Spectrometer
RGA	Residual Gas Analysis
sc	Superconducting
SDBS	Structural Database of Organic Compounds
SEM	Scanning electron microscopy
T_G	Glass transition temperature
TG(A)	Thermal Gravimetry / Thermal Gravimetric Analysis
TGDM	Tetraglycidyl diaminodiphenyl methane epoxy
TRC	Thermal Relaxation Calorimetry
TU	Technical University

1 Introduction

1.1 Motivation

This study is motivated by the planned *Facility of Antiproton and Ion Research* (FAIR). This new facility will cover a range of unique high-energy physics experiments in the fields of nuclear structure and matter physics, atomic and plasma physics, physics with antiprotons, as well as biological and material science [1], [2]. First presented in 2001 at the *GSI Helmholtz Center of Heavy Ion Research* (GSI) in the Conceptual Design Report [3] the Baseline Technical Report was prepared with the contribution of 2500 scientists and engineers from 45 countries and accepted by the International Steering Committee for negotiation of FAIR funding [1]. Recently (Oct. 2010) the international civil agreement between 9 countries was signed setting the final course of the facility.

Fig. 1.1 Picture of GSI today (left) and artificial graphic of the planned FAIR facility (right) [4]

FAIR will consist of a complex accelerator system including two superconducting synchrotron accelerator structures SIS 100 and SIS 300 having 100 Tm and 300 Tm of maximum magnetic rigidity using the old GSI facility as an injector (pre-accelerator). The circumferences of both synchrotrons will be 1100 m and their magnetic lattices will be

provided by new fast cycling superconducting (sc) magnets. Superconducting magnets are used to minimize costs due to their low construction and operation costs.

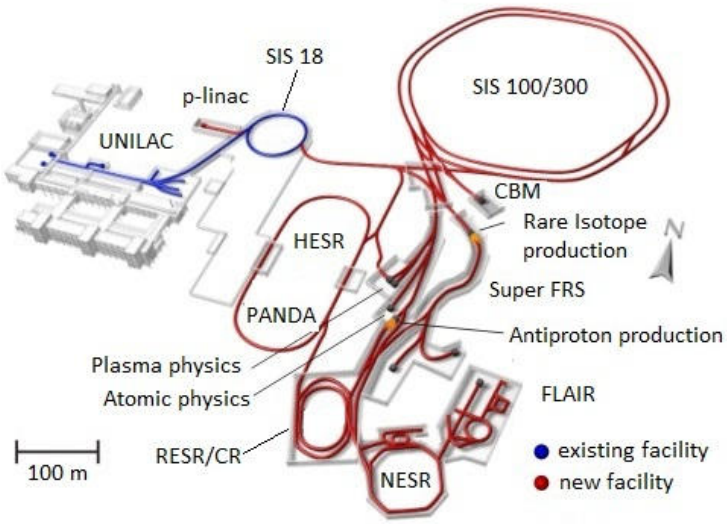

Fig. 1.2 Scheme of the existing accelerator facility of the GSI Helmholtz Center of Heavy Ion Research (left, blue) and the planned FAIR (red, right).

To meet the scientific goals of FAIR, the new facility has to provide high precision and intense particle beams which will be 2 orders of magnitude higher in intensity than the existing GSI facility. Additionally, the energy of heavy ion beams will increase by a factor of 10 (Table 1.1) [5].

Table 1.1 Overview of scientific topics and their demands at FAIR

Research Field	Energy	Peak Intensity	Average Intensity
Radioactive Ion Beams	0.4-1.5 GeV/u all Elements	$5x10^{11}$ ions/pulse	$3x10^{11}$ ions/sec
Antiprotons	29 GeV	$4x10^{13}$ ions/cycle	-
Dense Nuclear Matter	34 GeV/u Uranium	-	$2x10^{9}$ ions/sec
Plasma Physics	0.4-1 GeV/u	$1x10^{12}$ ions/pulse	-
Atomic Physics	1-10 GeV/u	-	$1x10^{9}$ ions/sec

This increase in energy and intensity will be a challenge in accelerator technology, especially for magnet design and vacuum technology. Beam losses will influence the dynamic vacuum of the machine as well as produce a secondary radiation field [6] which will alter materials and functional devices. Especially, materials sensitive to ionizing radiation are of primary concern. For example, the long-term reliability of insulation materials under such extreme

conditions is an issue of vital importance and therefore the topic of this study. A simple insulation failure would cause serious costs and long machine down-times of the accelerator.

1.2 Superconducting Magnet Design for FAIR

The planned synchrotrons (SIS 100 & 300) will consist of hundreds of magnets which will have to handle ion beams of very high intensity. This requirement can only be met by high cycling times and short ramping times. For the required beam rigidities and space constraints dipoles with fields up to 6 T are necessary which can only be provided by superconducting coils [5].

Despite common accelerators using superconducting magnets with a low ramping rate (e.g. the Large Hadron Collider at the CERN), the FAIR magnets will have to feature fast ramping rates such as 4 T/s up to 2 T and 1 T/s up to 6 T for SIS 100 and SIS 300, respectively.

The only facility so far using fast ramped superconducting magnets is the Nuclotron at the Joint Institute for Nuclear Research (JINR) in Dubna. Inspired by the good performance, GSI decided to build Nuclotron-type dipoles for the SIS 100 and started a big R&D phase [7], [8]. The optimization of these magnets led to the successful building and testing of the first three dipole and one quadrupole prototypes in the end of 2008 [9], [10]. For SIS 300 so far dipoles similar to the RHIC arc dipole [11] are foreseen. These magnets are of the cos(θ) type and use Rutherford cables with NbTi as superconductor in the coil. Figure 1.3 shows the schematic view of the cross section of the SIS 100/300 ring as well as the corresponding dipoles.

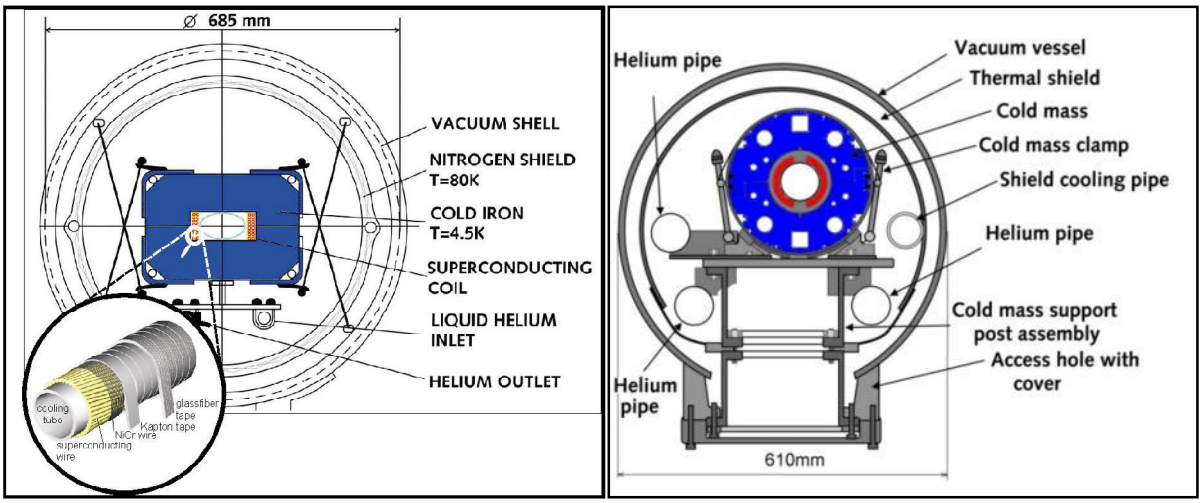

Fig. 1.3 Schematic cross section of the superconducting dipoles for SIS 100 (left) and SIS 300 (right).

1.3 Magnet Materials

Besides superconducting (sc) magnets also warm (room temperature) magnets will partly be used at FAIR. Therefore room temperature and low temperature properties of all materials are of importance. However, the focus of this thesis lies in the radiation hardness of superconducting magnet insulators and some technical components, based on material-analytic and performance characterization.
Superconducting magnets usually are composed of a variety of construction materials [12], such as:

-the superconductor itself, for example: NbTi, Nb_3Sn (coil wires)
-the stabilizer of the superconductor: Cu, Ag
-the solder which connects the sc strand and the stabilizer
-steel conduit for the liquid helium coolant and mechanical support of the coil
-the electrical insulation typically consisting of fiber reinforced resin thick enough to withstand the turn to turn ground voltages
-the superinsulation used for reducing heat losses
-various electronics and cabling, e.g. temperature sensors, quench detection and protection [13]

Basic design rules usually include careful application of material, electrical, and cryogenic science. The most important factor is matching the thermal expansion of all materials used, in order to guarantee tolerable stress limits followed by tightness against hydraulic and electrical leaks [14]. The electrical leak tightness is a very crucial point since vacuum flashovers can cause tremendous damage because of the high amount of stored energy and their discharge power [15].
Obviously the properties of the materials used should be well characterized and their long term stability should be predictable. In the special case of accelerator institutes (like Conseil Européen pour la Recherche Nucléaire (CERN), GSI) or magnets for fusion (for example International Thermonuclear Experimental Reactor (ITER) [16], [17]) not only the pristine material properties are of concern but also the radiation hardness of various components (digital cameras, temperature sensors) and magnet materials, including insulators and superconducting alloys.
Since effects in superconducting materials were part of a different PhD thesis [18], the focus in this thesis lies in the radiation damage of insulators such as polyimide (Kapton HN, Du

Pont de Nemours, Kaneka Texas), glass-fiber/plastic composites (G11-type, Isovolta AG, Gatex GmbH), specially glued polyimide joints (Pixeo/Apical, Kaneka Texas), Cernox HN temperature sensors as well as impregnated glass-fiber/plastic voltage breakers as described in the following chapter. Critical material properties such as dielectric strength and thermal properties at low temperature were measured as crucial material properties for the later application.

1.4 FAIR Relevant Materials

Glass-fiber reinforced plastics (GFRP´s)

Glass-fiber reinforced plastics, mainly used as structural support of the superconducting coil, may also act as electrical insulation.

Epoxy/glass-fiber composites

Glass-fiber reinforced plastics (GFRP´s) are composite materials consisting of a woven glass-fiber support surrounded by a matrix of polymer. The material properties of such composites are significantly influenced by (i) the properties of the fiber (ii) the matrix polymer and (iii) the interface between fiber and matrix [19]. The fiber, usually more strong in tensile strength, hereby reinforces an elastic polymer. Such composite systems try to combine the properties of both materials [20]. Due to the variation of fillers and matrices different material properties can dominate the composite. A full review about the influence of fillers and matrices is not the scope of this chapter but some properties of the composite systems used within this study shall be briefly introduced.

In Table 1.2 the properties of two types of glass fibers namely E-glass and S2-glass are summarized, whereas in Table 1.3 the different chemical compositions are contrasted [21], [22]. Next to glass-fibers, a broad range of products is found, to reinforce polyepoxy/cyanatester matrices. In this way, for example, the mechanical properties, thermal properties and temperature expansion can be tailored over a wide range [23], [24].

Table 1.2 Material properties of E- and S2-glass fibers

	Density (g/cm^3)	Elongation at fracture / %	Spec.- Heat capacity (kJ/kgK)	Thermal conductivity (W/mK)
E-glass	2.5-2.6	4.8	0.8	1-1.3
S2-glass	2.45	5.5	0.8	1.3-1.4

Table 1.3 Compounds used for glass fiber synthesis and their content in E- and S2-glass fibers

Compound	Content in % for E-glass	Content in % for S2-glass
SiO_2	53-55	64-66
Al_2O_3	14-15	24-25
B_2O_3	6-8	----
CaO	17-22	0-0.1
MgO	<5	9.5-10
K_2O/Na_2O	<1	0-0.2
other oxides	~1	<1

One GFRP widely used for superconducting magnets is named “G11CR” in which CR stands for cryogenic. This name is used in cryogenic engineering as it describes a standard but in fact is a trade-name for a specific material introduced by Monsanto Company. “G11” is a standard for industrial laminating thermosetting products given by the American National Electrical Manufacturers Association (NEMA LI1). The European standards which meets the American G11 standard is for example the EPGC308 standard given by the European Norm (EN 60893) were EP stands for epoxy resin systems and GC for glass clothing (woven glass fiber matrices). Some important properties of the composite tested in this study Gx_11.3303 Isoval HKB (G11/EPGC306/308) provided by Gatex GmbH are given by the manufacturer datasheet:

Table 1.4 Material properties of Gx_11.3303 composite (G11-type GFRP) Gatex GmbH

Composite	Density (g/cm^3)	Dielectric strength DIN 53481 (kV/mm)	Thermal conductivity DIN 52612 (W/mK)
Gx_11.3303	1.7-1.9	40	0.3

In general the matrices of these composites are made of an epoxy resin which contains one or more epoxy groups per molecule (see Fig. 1.4). This reactive side-group is used to crosslink the material with a curing agent to create a thermosetting material. Due to the high reactivity of the epoxy group many different curing agents with versatile properties can be used. Because of their good wettability these thermosetting materials are suitable for bonding, casting, and laminating allowing application as surface protection, adhesive, and matrix for composite materials. The reasonable ease of manufacturing at room temperature and ambient atmosphere and especially the price of the products (~5-10 €/kg) distinguishes the polymer system from other high performance polymers such as polyaramides (Kevlar™) and

polyimides (Kapton™). The first report about phenolic polyepoxides was published in 1934 by P. Schlack from "IG Farben" and still today most of the epoxy resins used in industry are phenolic epoxies' for example on the basis of epichlorohydrin and bisphenol. Typical curing agents include cyclic anhydrides of di- or tetra-carboxylic acids, aliphatic di- or polyamines, polymercaptanes and di-cyanides. Fig. 1.4 shows the typical curing mechanism of epoxy resins with an amine curing agent used in this study to synthesize thin foils of polyepoxy matrix in order to analyze the ion induced degradation of the polymer matrix without fibers. The curing follows an easy mechanism: The amine attacks as nucleophile the sterically less hindered carbon atom of the epoxy. In this way a secondary amine as well as a hydroxyl group is formed. This secondary amine is more reactive than a primary amine and able to add a second epoxy. Less favored as last reaction, the hydroxyl-group itself can add an epoxy. The combination of these three reactions highly cross-links the material [25][26][27].

Cyanatester/epoxy composite

Cyanatester matrices for composites are increasingly used in many high performance applications in electronics and aerospace applications. They exhibit good mechanical, electrical and thermal properties over a wide temperature range as well as high performance in other important fields such as low humidity uptake [28]. There exists a broad variety of different cyanatesters bearing different chemical structures and different properties. A popular candidate often used is Bisphenol A Dicyanat (BADCY) which is commonly homopolymerized by applying high temperature (Fig. 1.5), [29]. It was proved that cyanatester composites show enhanced radiation hardness against ionizing radiation such as gamma and a combination of gammas and neutrons ("reactor irradiation") compared to classical epoxy systems even if they were blended with epoxy to reduce production costs [30], [31], [32]. In 2009 commercialization of these products started for their application in superconducting magnets by Composite Technology Development, Inc. (CTD), [33].
In this thesis a hot pressed cyanatester/epoxy/S-glass prepreg from Isovolta AG was used to compare its radiation hardness with classical resin/e-glass systems related to heavy ion induced damage.

Diglycidylether of Bisphenol F (DGEBF)

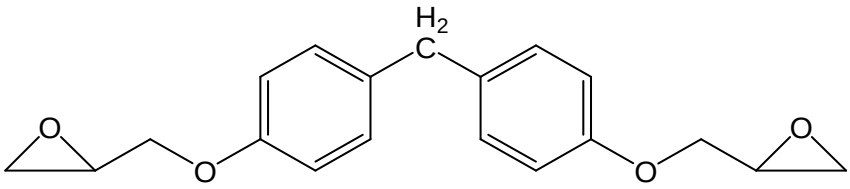

Diethyltoluoldiamin (DETDA; 2,4- & 2,6-Isomer)

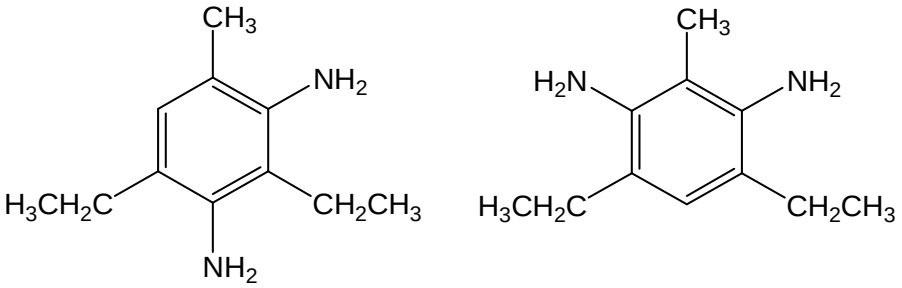

The three main reactions in epoxy/amine systems

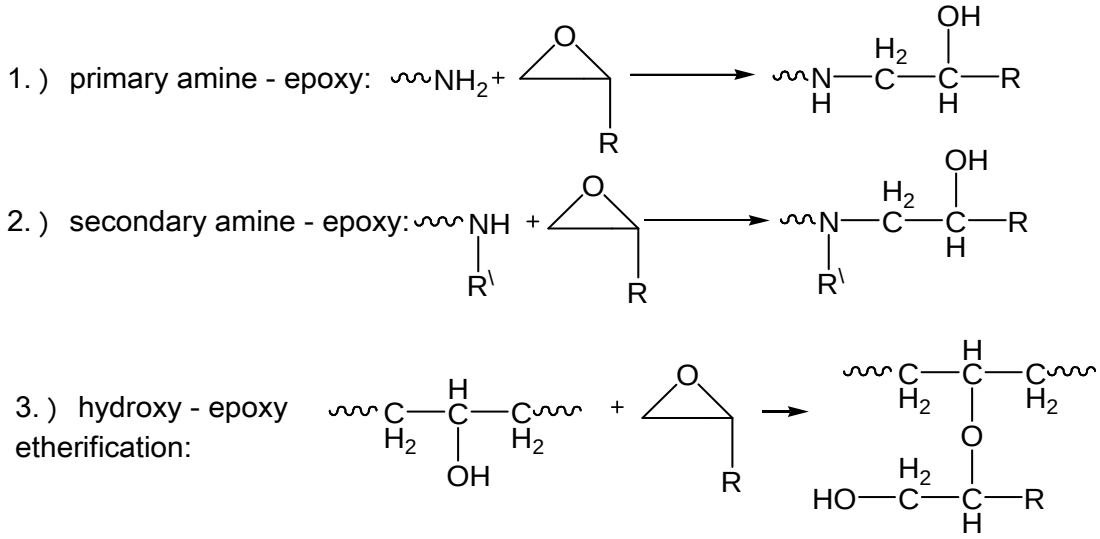

Fig. 1.4 Used polyepoxy and amine curing-agent and the main reaction steps of the curing

BADCY

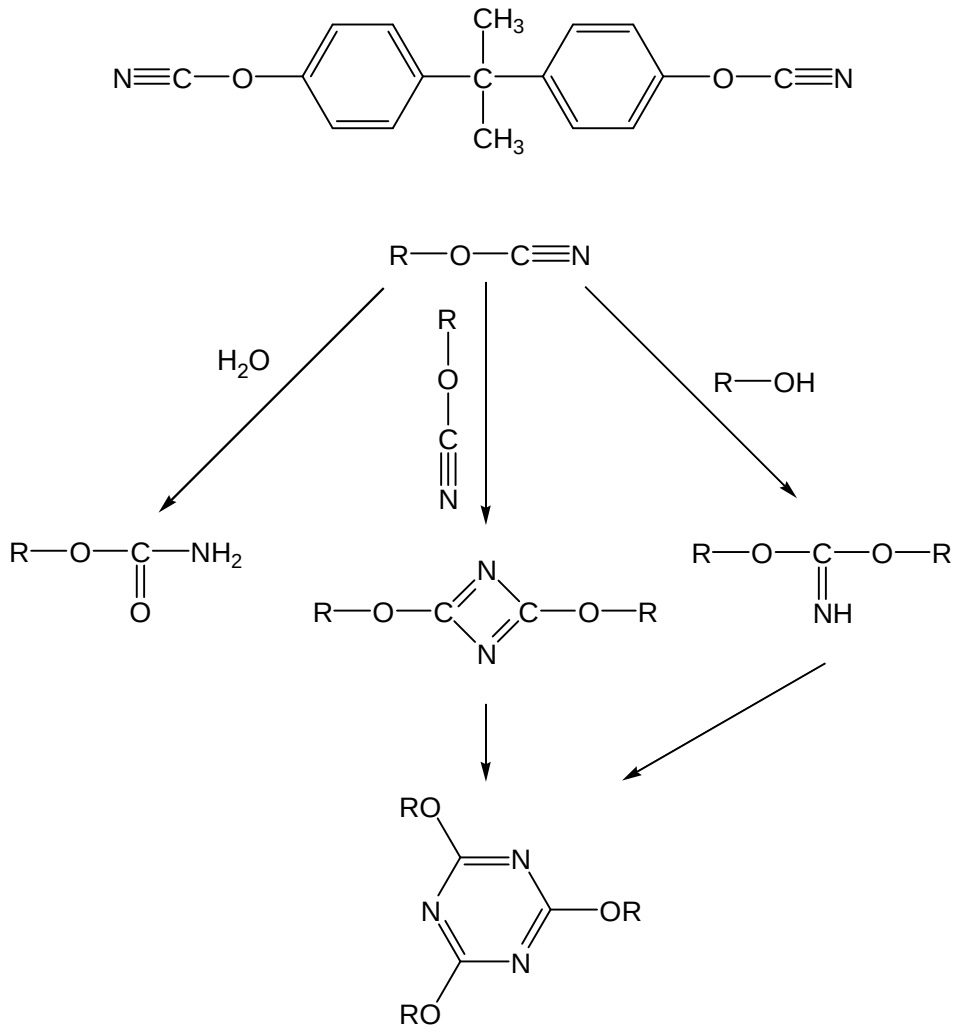

Fig. 1.5 Chemical structure of the monomer BADCY and the possible reaction path during thermal polymerization of cyanatesters [34].

Radiation hardness of glass-fiber reinforced plastics

There are extensive studies about radiation damage of GFRP`s mainly started in the 1980´s because of the start of bigger fusion projects like ITER and the building of high power ion accelerators such as CERN. However the broad variety of different composite types and the large number of material properties to be tested makes direct comparisons difficult. This chapter will summarize some important issues and discuss results available in the literature.
Most studies on radiation hardness of insulators for superconducting materials focus on changes in mechanical properties induced by radiation, where the type of radiation used in most cases is gamma or neutron radiation or a mixture of both (reactor radiation). To our knowledge there are only a few studies dealing with ion-radiation induced changes in dielectric strength and thermal properties of such materials ([35], [36]) and no study so far has dealt with heavy ion induced changes on macroscopic material properties of GFRP´s.
Within glass-fiber reinforced plastics, mainly the type of fiber and type of used polymer system (resin+curing agent) may be varied followed by fiber loading and addition of filler materials. So far many different types of composites have been tested and some trends will be summarized briefly:

Influence of composite type

In general aromatic polymers matrices give a more radiation stable composite compared to aliphatic systems [37]. Therefore polyimide composites are in principle to favor but in most cases not practical due to their poor machining properties as well as difficult manufacturing. After polyimide composites, cyanatesters and bismaleimide composites and mixtures of cyanatester/epoxy composites have been found to be more radiation stable than pure cured epoxy composites [30]. Within epoxy systems usually full aromatic structures (aromatic resin cured with an aromatic diamine curing agent) give a better radiation resistance as confirmed with G11-type composite (as used in this thesis) compared to G10 which uses the same bisphenol resin but an aliphatic curing agent [38]. Secondly the type of epoxy functionality influences the radiation hardness and for example tetra-functional epoxy systems (e.g. TGDM) are found to perform better compared to tri-functional and bi-functional epoxy [37], [39].
Still today epoxy systems are widely used because of their overall good performance, machinability and their cost. Standard epoxy/E-glass composite may cost ~5-10 €/kg while an advanced cyanat ester/S-glass composite can be in the order of 90 €/kg.

Composites using boron free glass-fibers

Next to the variety of different properties of different fiber materials [40] several studies found that boron in the form of boron oxide present in some types of glass fibers (e.g. E-glass) undergoes a nuclear reaction due to neutron capture and α-decay ($^{10}B(n, \alpha)^{7}Li$). This α-decay damages the interface between polymer matrix and fiber causing an enhanced sensitivity of these composites to radiation [41], [42]. In cases were radiation induced debonding or delamination takes place, S-glass (being free of boron oxide) is found to show less debonding giving those composites greater radiation hardness together with their better fundamental strength [43]. It should be noted that in some studies this effect is found to have only minor importance leaving an unclear picture of this effect [38].

Influence of irradiation temperature

Irradiation campaigns have been performed at low temperatures such as 4.2 K (liquid helium), 77 K (liquid nitrogen), and at room temperature. At low temperatures, radiation induced outgassing of radiolytic degradation products are known to be trapped and accumulate inside composite materials. Produced radicals show different lifetimes and diffusion properties at low temperature. Therefore some studies on the influence of irradiation temperature on the radiation induced changes of mechanical properties were performed. They show that the irradiation temperature has only minor effects on the degradation behavior [44], [45] even so the material itself initially exhibits enhanced properties when tested at low temperatures. Because of this, most irradiation experiments within this study (see chapter 4) were performed at room temperature to simplify experimental set ups. In some cases were low temperatures were mandatory (e.g. outgassing studies at low temperature) irradiation experiments at cryogenic temperature were carried out. It should be noted that in the case of swift heavy ion (SHI) irradiation of polyethylene (PE) low irradiation temperatures were found to increase the production yield of special radiolytically synthesized chemical compounds (e.g. alkynes). This result was assigned to a greater creation time of SHI induced defects compared with the diffusion time of mobile species to escape from the bulk material [46].

Influence of radiation type

Depending on the type of application in FAIR components, composite materials will be exposed to different types of irradiations or irradiation spectra. Radiation hardness tests therefore should be performed close to real conditions. In the case of glass-fiber reinforced plastics it is found, that the type of radiation (gamma, electrons and neutrons) has no significant influence on material property degradation [44]. This result is different for polymers where fast neutrons degrade some polymers faster than gamma radiation from a Co^{60}-source [47].

No comparative study so far exists for high-energy heavy ions. For FAIR, at which heavy fragments are expected to contribute to the radiation spectrum, comparative tests are indispensable, because it is known for many material classes (e.g. polymers, magnetic alloys) and biological systems, that the type of radiation and its energy deposition can have crucial effects on its destructive power [48], [49], [50].

Polyimide

Polyimides are an important class of polymers because of their outstanding properties such as high dielectric strength, mechanical stability and resistance against temperature, radiation and many solvents [51]. Especially aromatic polyimides are applied in high temperature and radiation environments such as accelerator magnets or space research. Polyimide type polymers are commercially available in many different industrial forms such as films, cable insulations and powders. Polyimides can be synthesized out of a great variety of monomers and different synthesizing methods and strategies [52]. This chapter will focus on Kapton type polyimide (Kapton™ HN, Apical™ AV), which is widely used as insulation in accelerator magnets (structure shown in Fig. 1.6).

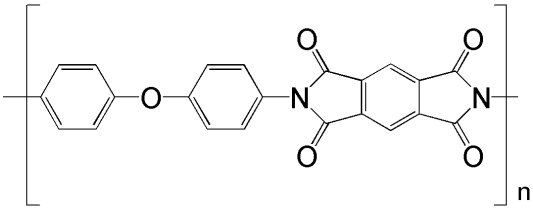

Fig. 1.6 Chemical structure of Kapton-type polyimide

Kapton is a trademark for the first commercially available film which was introduced by Du Pont in the late 1960´s. It is synthesized in a two-step process via polyamic acids (Fig. 1.7). In the first step a polyamic acid is synthesized via the reaction of a diamine and a

dianhydrate in a dipolar approtic solvent. The polyamic acid serves as a soluble polymer precursor which in the second step is thermally cyclized.

In the case of Kapton and Apical AV the used monomers are pyromellit dianhydride (PMDA) and 4,4'- diaminodiphenylether forming pyromellitimide. Kapton HN from Du Pont de Nemours and Apical AV from Kaneka Texas exhibit the same chemically structure and quite similar properties as contrasted in Table 1.5.

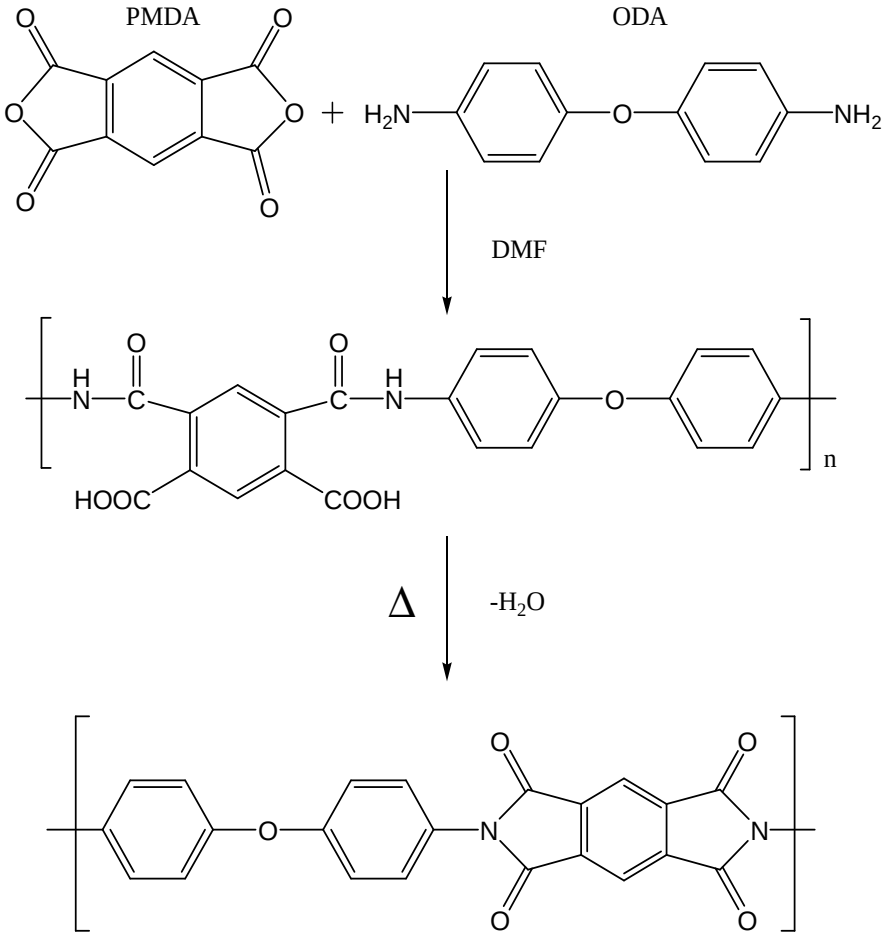

Fig. 1.7 Synthesis of Kapton-type polyimide

Table 1.5 Material properties of Kapton HN and Apical AV type polyimide

	Tensile Strength (MPa)	Dielectric strength (kV/mm)	Therm. Cond. (W/mK)	Density (g/cm^3)
Kapton HN	231	240	0.12	1.42
Apical AV	165	236	0.12-0.2	1.42

Radiation hardness of polyimide

This chapter summarizes the main results concerning radiation induced changes of material properties of polyimide relevant to magnet design, such as mechanical and dielectric strength and thermal properties. Radiation induced effects on the chemical structure will be discussed in chapter 5.1 together with the results of this thesis.

Polyimides are prominent candidates for magnet insulators in radiation environment such as accelerators or fusion magnets [53]. With a focus on low temperature and room temperature irradiation/testing it has been found that polyimides such as Kapton are about 5 times more radiation hard compared to classical epoxy systems and lose about 40 % of their mechanical strength at about 100 MGy of gamma radiation [54]. In the case of gamma and neutron irradiation, a decrease in mechanical properties takes place at lower doses than changes in electrical properties [55]. Electrical strength after irradiation is often found to decrease whereas electrical properties such as conductivity and dielectric constant are found to be increased [56]. In the special case of ion irradiation this loss of mechanical properties is accelerated [57], [58] and the increase in electrical conductivity is found to be dependent on the stopping power of the used ion [50], [59]. In the work of D. Severin [58] a dose limit for heavy ions is given at about 1 MGy whereas about 100 MGy for gamma radiation is postulated [60]. The effects on the electrical conductivity of polyimide are found to be remarkably sensitive to heavy ions. Thus the postulate, that mechanical properties are decreased before any electrical properties change is not valid anymore and motivates the measurements on the dielectric strength in chapter 5.1. Concerning thermal properties at low temperatures no study has so far treated radiation induced changes of polyimides or other polymers. Since this is a critical point for design criteria first measurements were conducted within this thesis.

1.5 FAIR Relevant Technical Components

Additionally to the explorations of ion induced changes in polymers and glass-fiber reinforced plastics, the performance of some accelerator components were tested according to their technical performance after radiation exposure. Since these accelerator components do not belong to a certain class of the previous described materials their composition and usage in accelerator magnets is described briefly.

Axial insulation breaks ("Voltage breaker")

Axial insulation breaks are needed to insulate all cryogenic supply lines which are on the ground potential of the winding of each magnet. The position of the voltage breaker inside the SIS 100 FAIR prototype magnet is shown in Fig. 1.8. The insulation breaks have to guarantee leak tightness against the liquid helium inside as well as withstanding the high voltage of the coil (several kV).

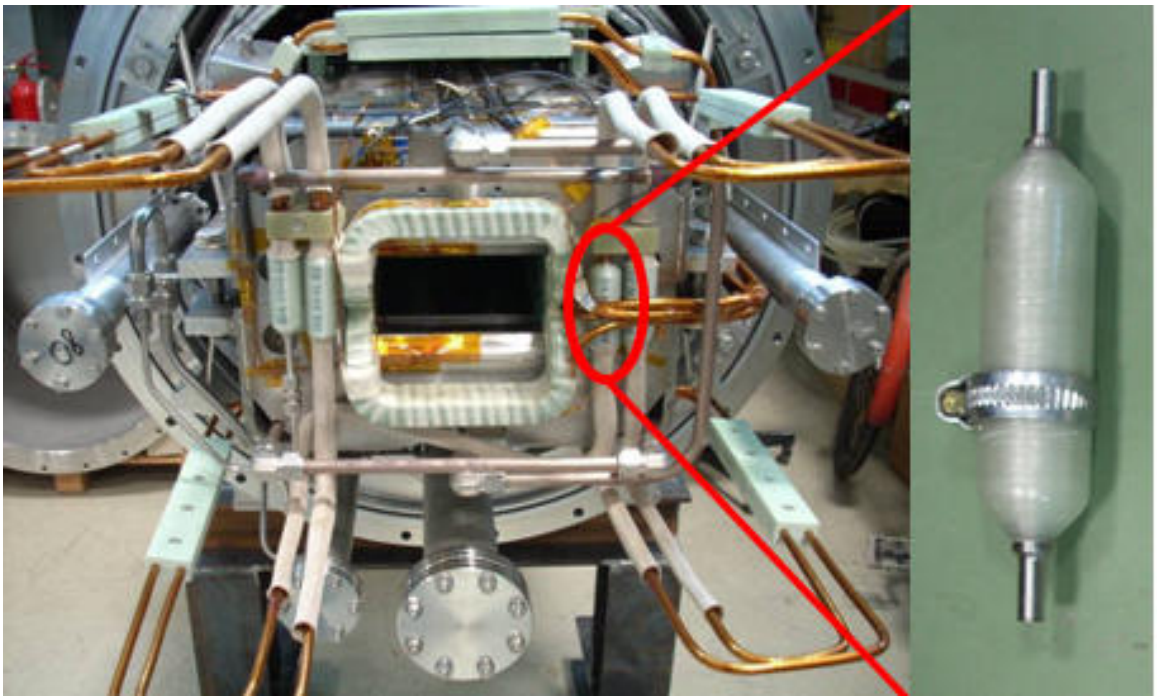

Fig. 1.8 Picture of the first SIS 100 dipole prototype (left) and the axial insulation break magnified in the picture (right)

The foreseen voltage breakers of the SIS 100 FAIR magnets consist of two stainless steel tubes which are surrounded by a G11-type glass-fiber reinforced plastic (indicated in the technical drawing, Fig. 1.9). The manufacturing process is a filament winding technique which is followed by a special sealing with a polymer coating. This sealing guarantees tightness against the leakage of liquid helium but is also a weak link regarding the radiation damage. G11-type GFRP is used because via the fiber content its thermal expansion can easily be controlled to match the thermal expansion of the used stainless steel tubes [14].

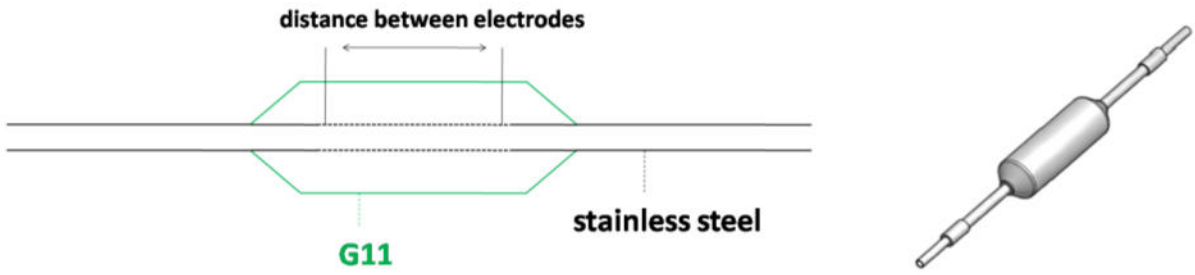

Fig. 1.9 Scheme and composition of the axial insulation break (left) and 3D drawing (right)

The composition of the polymer coating is not revealed by the producing company. Therefore, the voltage breaker was tested against ion radiation damage by means of testing the leak-tightness of helium gas at room temperature (RT) and cryogenic temperatures as well as after thermal cycling between these.

Cernox™ temperature sensor

Cernox™ temperature sensors belong to the class of semiconducting resistance thermometers which are useful low temperature sensors because of their negative temperature coefficient of resistance [61]. Usually they are oxynitride thin films (for example from zirconium) which are sputtered onto a sapphire substrate [62], [63], [64]. They are a popular choice to be used within superconducting magnets because of their good long term stability and low magnetic field induced error, compared to, for example, carbon glass sensors (which at low temperature have a higher sensitivity compared to Cernox™). Regarding the radiation resistance, oxynitrides are expected to be radiation hard because of their inorganic structure and were successfully tested against gamma radiation of up to 1 MGy [65]. So far no data exist on ion irradiated Cernox™. Tests on this material are described in chapter 4.4.

Pixeo glued polyimide specimen

In some parts of the SIS 100 sc magnets, polyimide insulation is foreseen to be fixed with specially designed polyimide glue (namely Pixeo^{TM} provided by Kaneka Texas). This glue belongs to the chemically attaching glues being a kind of uncured polyimide which is cured under high pressures at about 300°C in a polycondensation-reaction. Two layers of polyimide insulation can be attached in this way via a thermal process. In order to investigate the irradiation hardness of this glue connection, special peel test specimen provided by Kaneka Texas Company were irradiated and subsequently analysed by the company. In literature so far only some epoxy resins and classical glues were tested against gamma radiation and found to be sensitive to irradiation [66]. Since polyimide is known to be rather radiation stable, this special gluing technique is also expected to exhibit rather high radiation resistance.

1.6 Dose Estimations for the Superconducting Coil of FAIR Magnets

In order to estimate which particle spectra will hit the magnet coil, detailed calculations were performed using the SHIELD code [67]. This Monte Carlo code can be used to simulate how energetic charged particles are transported through condensed matter and which secondary particles are created along their trajectory taking into account nuclear reactions. The most prominent case of beam losses expected at FAIR is due to ions which lose one electron and thereby lose a stable orbit. They hit the stainless steel beam tube and induce a secondary spectrum of different ions, protons and neutrons. The fragmentation is in principle isotropic, using the producing ion as inertial frame, but, choosing the magnet coil as laboratory frame, have a preference in the forward direction of the beam. Figure Fig. 1.10 shows the energy spectrum of different fragmented nuclei which are produced when one 1 GeV/u uranium ion hits the beam tube under grazing incidence of about 1° (17 mrad) taken from [68].

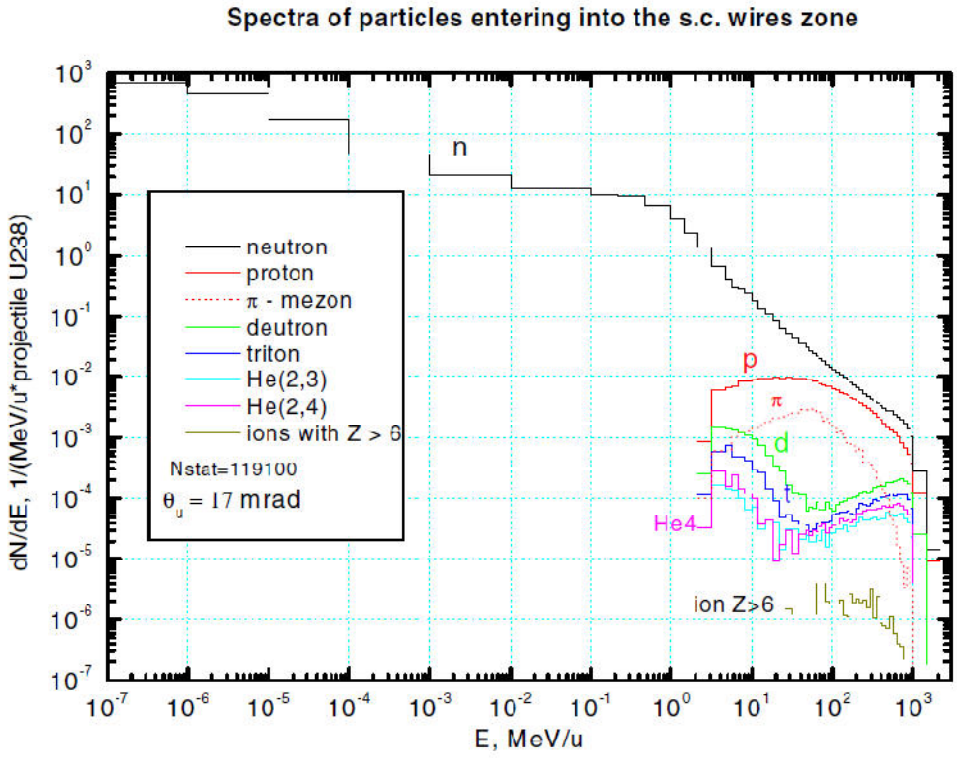

Fig. 1.10 Energy spectra of different fragmented nuclei which hit the closest superconducting wire [68].

The most prominent fragments in the energy regime >3 MeV/u are neutrons and protons. Heavy ions with atomic number Z>6 are about 0.1 % of the fragments produced (particles having lower energies than 3 MeV/u are neglected in Fig. 1.10 because of their low penetration depth they do not reach the superconducting coil). Because of the different penetration depths and stopping powers of the different particles the dose absorbed by the

magnet coil components is strongly dependent on the geometrical position of the "target" and the angle of lost beam.

The influence of the "sample/target position" is indicated in Fig. 1.11 showing the dose introduced by one uranium ion of 1 GeV/u which is lost at an angle of 1° grazing incidence to the beam tube. The calculation was performed for three slices of "target" each 2 mm thick and consisting of G11-type GFRP positioned one behind the other, as indicated in the scheme. The result clearly demonstrates that the first 2 mm of G11 (Pos. 1) will absorb a dose about an order of magnitude higher than the last 2 mm (Pos. 3).

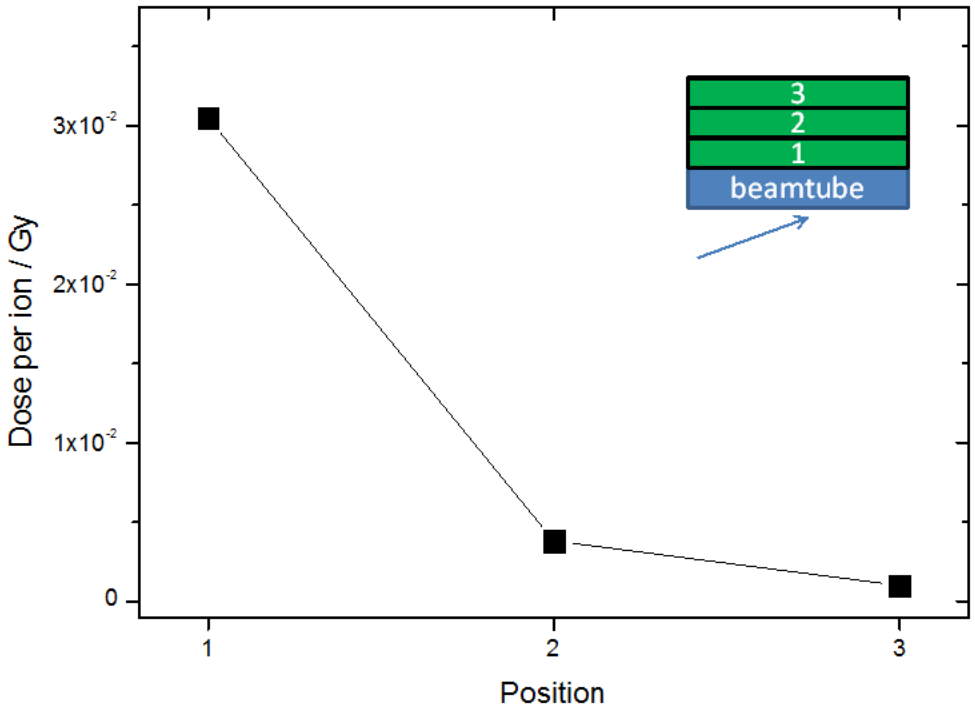

Fig. 1.11 Results of dose simulation for G11-type composite samples at different positions. Calculations are performed for 1 GeV/u uranium ions lost under an angle of about 1°.

Exploring the contribution of different particles (i.e. light and heavy fragments) on the absorbed dose we performed calculations using different beam loss angles and thicknesses of polyimide and G11-type GFRP as target. The results are summarized in Table 1.6. For the expected case of beam losses having an angle of about 1° the results demonstrate that heavy ions, having a Z>6 induce ~76.5 % of the dose in the first layer (~20 μm) of the insulation. However, in the first 2 mm of the coil only 55 % of the dose is created by heavy fragments. Concerning the beam loss angle it is found, that a higher beam loss angles (2.8° instead of 1°) increase the deposited dose into the magnet coil by a factor of ~3.6. For a beam loss angle of 4° the greatest amount of dose is deposited by the primary ions (54 %) which are not stopped in the beamtube. The results of the latter calculation are not presented because of its improbability in the later application.

Table 1.6 Results of the SHIELD simulation of the secondary radiation field of the superconducting magnet coil for different angles of beam loss. Calculations were performed for 1 GeV/u uranium-ions irradiation of stainless steel

Angle of beam loss: 1°					
Polyimide (20 μm thick)			G11 (2 mm thick)		
Type of particle	Dose per ion (Gy)	Dose (%)	Type of particle	Dose per ion (Gy)	Dose (%)
Protons	1.4×10^{-9}	8.3	Protons	1.1×10^{-9}	17.1
Z=2-6	2.3×10^{-9}	13.6	Z=2-6	1.65×10^{-9}	25.7
Z=6-90	1.3×10^{-8}	76.5	Z=6-90	3.5×10^{-9}	54.5
Angle of beam loss: 2.8°					
Polyimide (20 μm thick)			G11 (2 mm thick)		
Type of particle	Dose per ion (Gy)	Dose (%)	Type of particle	Dose per ion (Gy)	Dose (%)
Protons	1.5×10^{-9}	3.5	Protons	1.2×10^{-9}	5,1
Z=2-6	2.6×10^{-9}	6	Z=2-6	1.9×10^{-9}	8.1
Z=6-90	3.9×10^{-8}	90	Z=6-90	2×10^{-8}	86

This means that every material in the magnet coil, each of which exhibit different levels of sensitivity towards radiation damage, will absorb a different amount of dose caused by different particle spectra. This mirrors the challenge of giving a true lifetime expectation of the magnet coil, also keeping in mind that different types of radiation show different efficiencies in producing radiation damage, and that most of the numbers needed for simulations or calculations are not available. To better understand ion induced changes of material properties the following two procedures were followed (i) directly exposing samples to ion beams of different energy losses and (ii) performed irradiations close to the future situation at FAIR by mounting the samples behind a steel target. By bombardment of this steel target the spectra of secondary particles is produced.

2 Interaction Between Energetic Charged Particles and Solid Matter

2.1 Energy Loss and Range of Ions

When passing through condensed matter, charged energetic particles with a kinetic energy of several MeV/u lose their kinetic energy mainly via two processes (i) the nuclear energy loss and (ii) the electronic energy loss.

Equation 1
$$\left(-\frac{dE}{dx}\right) = \left(-\frac{dE}{dx}\right)_{nu.} + \left(-\frac{dE}{dx}\right)_{el.}$$

The interaction cross section is a function of energy. In the case of (i) low energy particles (E<0.01 MeV/u), elastic collisions dominate (nuclear energy loss) while at (ii) higher energies, electronic excitation and ionization occur. The particles used in irradiation experiments within this study are in an energy regime above 1 MeV/u and therefore the electronic energy loss is responsible for the induced material changes. Quantitatively the electronic energy loss at high energies is described by the so called Bethe-Bloch equation [69], [70]:

Equation 2
$$\left(\frac{dE}{dx}\right)_{el.} = \frac{4\pi \cdot e^2 \cdot Z_{eff}^2 \cdot Z_t \cdot N}{m_e \cdot v^2}\left[ln\left(\frac{2m_e \cdot c^2 \cdot \beta^2}{I}\right) - \beta^2 - \delta - U\right]$$

with e being elementary charge, Z_{eff} the equilibrium effective charge of the ion, Z_t the atomic number of the target atoms, N the density of target atoms, m_e the electron mass, v the ion velocity, β the velocity in the unit of the speed of light and I the ionization energy of the ion and δ and U being correction factors inner shell electron contribution and relativistic effects.

Summarizing Equation 2, the electronic energy loss is a function of ion velocity, the atomic number of the projectile ions and target atoms and the targets density. These dependences are visualized in Fig. 2.1 by SRIM 2010 [71] calculations for different ions with similar energy in polyimide and in Fig. 2.2 for one ion energy in different target materials. The non-

linear behavior of the energy loss should be noted. In contrast to photons which lose their energy as a negative exponential function, charged particles show first an increase in energy loss rate and later have a maximum at the so called Bragg peak.

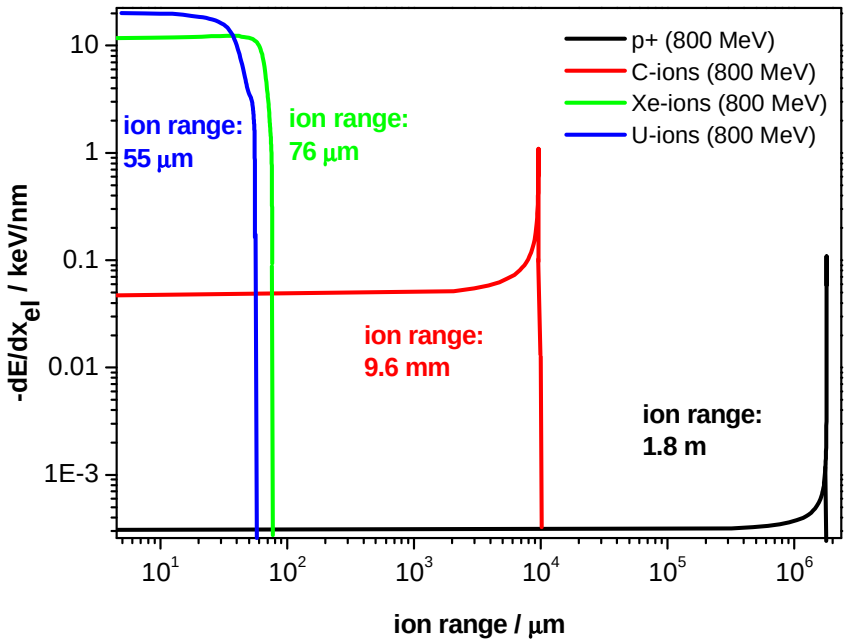

Fig. 2.1 Electronic energy loss of different ions in polyimide versus the ion range calculated with SRIM 2010

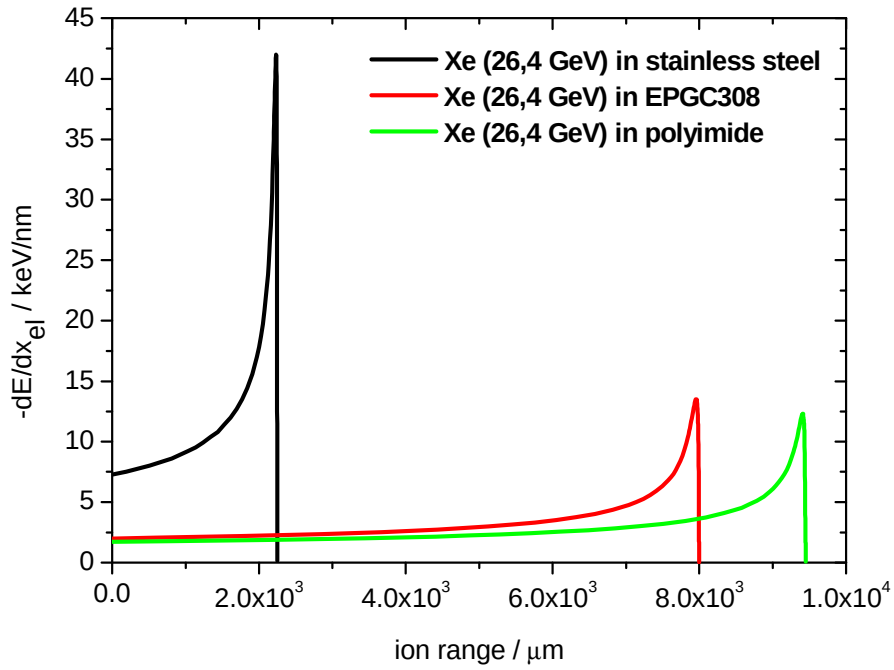

Fig. 2.2 Electronic energy loss of xenon-ions in different "target"-materials versus the ion range calculated using SRIM2010

The range of the ions is directly connected to their specific energy loss and the initial energy of the particle. Ions of initial energy E_0 moving through a solid target material by a distance x lose the energy E as follows:

Equation 3 $$E = E_0 + \Delta E, with\ \Delta E = \left(-\frac{dE}{dx}\right)\Delta x$$

The distance in the target material is given by:

Equation 4 $$dx = -\left(\frac{dE}{dx}\right)^{-1} dE$$

The total range R (projected range) of the ion integrated over all energies between E_0 and zero is given by [72]:

Equation 5 $$R = \int_0^{E_0} \left(\frac{dE}{dx}\right)^{-1} dE$$

Ion projectiles at such high energies first transfer their energy to the electrons of the target [73], [74]. This initiates a cascade of secondary electrons (δ-electrons) which spreads radially. The range of δ-electrons depends on various parameters such as the initial ion energy and the target density and is analyzed more precise by J. Schou [75]. Thereafter, a complex mixture of ionization processes is followed. The dE/dx_{el} is the linear energy transfer and does not characterize the local energy density, which depends on the velocity of the ion [49]. Fig. 2.3 shows the radial dose distribution deposited by δ-electrons calculated for different ions and energies in polyimide according to [76]. The localized energy dissipation is responsible for the fact that in most insulators a so called “latent ion track” with a few nanometer in diameter is produced. Typically the track is found as a modified region characterized by severe material changes. It is shown, that depending on the stopping power, different track morphologies appear. At low stopping powers separated damage zones appear along the ion trajectory, whereas at higher electronic energy loss the damage zones start to percolate creating a homogeneously affected cylinder. In polymeric materials, being more sensitive to radiolysis compared to inorganic insulators, these damage zones often show drastic changes in physical as well as chemical properties. This latent track is surrounded by a shell of less damaged material which in the case of polymers can be in the range of hundreds of nanometers [77][78].

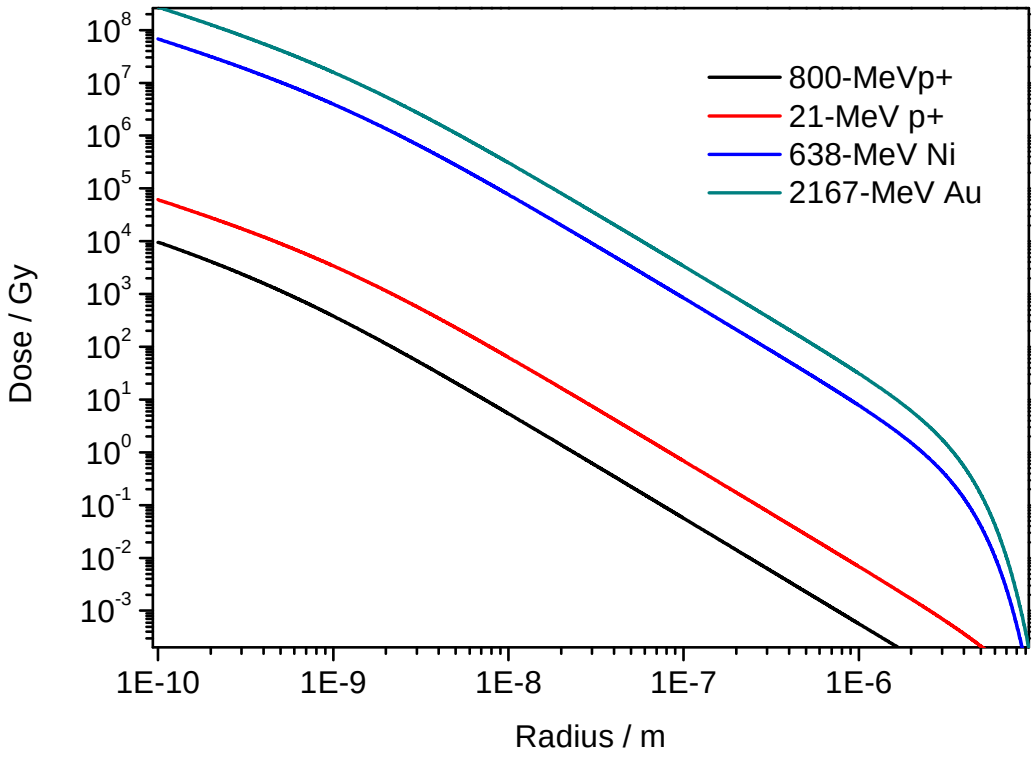

Fig. 2.3 Radial dose distributions by δ-electrons of different ions in polyimide. Calculations were performed after the model of Katz et al. [76].

2.2 Track formation processes

Even though ion track formation has been studied for many years a full understanding of the complex degradation processes still remains to be achieved. The main theoretical models can be classified into two groups:

Coulomb Explosion Model

Primary ionization processes leave a cloud of ionized atoms while the corresponding δ-electrons are emitted to farther distance [72]. In a conductive material these electron holes are neutralized quickly while in insulators the stored electrostatic energy starts to initiate atomic motion and is the driving force for an atomic collision cascade. This mechanism was suggested during a time where no tracks were found in metals [79]. After tracks were observed in metals many attempts were used to calculate if the electrostatic forces are high enough to produce atomic motion in metals [80]. Presently, no Coulomb explosion description is available that describes empirical results appropriately or gives sufficient predictions.

Thermal Spike Model

In the thermal spike model the diffusion of deposited energy is described by heat equations. The region of ionization can be envisioned as a narrow cylinder which is rapidly heated to a high temperature and quenched again [81]. There are two different thermal spike models often used for swift heavy ion induced changes in materials. The inelastic thermal spike model (ITSM) and the analytical thermal spike model (ASTM) [82] [83] [84]. The principle of both models is similar. The energy is first deposited on the electrons which transfer it to the lattice via electron-phonon coupling. The track formation is coupled to a melting of the material following by a fast cooling which leads to amorphous phase transformation. Usage of this model, first applied to inorganic insulators, has been extended to different materials and in the special case of polymers it agrees well with experimental data of ion track radii (e.g. [85], [86], [87]).

2.3 Critical Material Properties of Magnet Insulators

Dielectric Strength

Insulators used in accelerator magnets especially superconducting magnets which operate at cryogenic temperatures have to meet various demands [88]:

-They have to give the conductor mechanical support under often high mechanical stress in a wide temperature field.
-Insulating properties such as resistivity and dielectric strength must be sufficient.
-Thermal conductivity must be high enough to remove losses to a cooled surface.
-Thermal contraction should fit to other materials such as stainless steel or copper.

Electrical characteristics of an accelerator magnet or especially superconducting magnet are of minor interest during regular operation but important during a fast dump or "quench" of the magnet. In most cases the strength and reliability of a magnet is controlled by the electrical insulation [89].
For insulating materials the dielectric strength is an important parameter; it is defined as the maximum electrical field which a material can withstand without failure of insulating properties. To compare different materials of different thickness the unit is normalized by the thickness of the material and given in kV/mm.
Dielectric breakdown in polymers has been studied for decades and many theories have been proposed trying to explain observed phenomena. However, still many problems remain unsolved. Summarizing the main theories, the electrical breakdown is characterized by the electrical, mechanical and thermal properties of the investigated material as well as its chemical structure, manufacturing quality and type of electrode material. In general the electrical breakdown is accompanied by the destruction of molecular structure and formation of a conductive trails ("treeing") [90]–[92]. It can be divided into "tree inception" and "tree propagation" [93]–[95]. In polymeric high voltage insulations the tree inception time is mainly dependent on the conductor (i.e. the electrode or cable core), whereas the tree propagation time is dependent on the material properties of the insulator [96]. Depending on the type of material and the number of pre-existing defects the formation of a conductive path may be slow, but once a percolation path exists the breakdown suddenly appears in an abrupt and damaging way. Quick charge movement initiates electrical heating (Joule

heating) leading to electrical and thermal damage usually destroying the insulator along its path.
The factors which influence the dielectric strength of materials are versatile and some trends important for accelerator magnet design are summarized briefly:

Influence of the insulator thickness or multiple layer insulation

Increasing the insulation thickness is possible in two ways (i) choosing a thicker insulator or (ii) multiple winding of an insulator. In both cases the dielectric strength is found to be dependent on the thickness in a nonlinear relation [97], [98]. Doubling the thickness of an insulator is not doubling the dielectric strength. Empirically it is found that the dielectric strength of most insulators is found to be proportional to the specimen thickness to the power of 0.5 [99]. The reason is ascribed to the increased probability of having a critical defect within the material, starting the tree inception.

Influence of the temperature and environment

Insulators at very low temperatures usually exhibit a higher dielectric strength in the case of liquid nitrogen and cryocooling inside a vacuum chamber [100]. Despite this, in liquid helium a lower dielectric strength is found [100], [101]. At FAIR the sc magnet insulators will be cooled inside a vacuum vessel by stainless steel tubes. The used insulators will therefore show a better performance as indicated by room temperature values.
In addition to the temperature and manufacturing quality, the applied type of test greatly influences the result of dielectric strength measurements. In typical dielectric strength measurements a voltage is ramped (dV/dt) until breakdown of the sample. For high ramping rates usually a higher dielectric strength is found. The reason for this is that during the measurement itself the electrical fields degrade the material. At high ramping rates the electrical degradation is biased, resulting in a higher observed dielectric strength.
Tests carried out under DC and AC (60 Hz) conditions at a fixed ramping speed show that for most polymers the AC dielectric strength is found to be lower than in the DC case. While under DC conditions, it is mainly the space charge formation that guides the breakdown of the material, under AC voltage so-called partial discharges additionally degrade the material. Standard test methods (ASTM D 149-91) are usually performed under AC conditions while the condition inside a ramped magnet follows more the DC case. In this work both types of tests were used whenever applicable.

Statistical behavior of the dielectric breakdown and Weibull Analysis

Statistical characteristics of insulators are important for lifetime estimations and asset management as they are useful tools to evaluate the reliability of a given insulation [102]. The breakdown strength of polymeric insulators is found to have a larger dispersion compared to liquids or gases [103]. This effect is ascribed to the existence of internal weak points in the polymer such as voids or inhomogeneities. One distribution commonly used to analyze breakdown strength data is based on a model of weakest links: the so called Weibull distribution [104], [105]. The Weibull distribution is one of the extreme value distributions without a definite physical implication. In its two parameter form it is written and linearized as follows:

Equation 7: $$F(x) = 1 - e^{-\left(\frac{x}{\alpha}\right)^{\beta}} \Leftrightarrow \ln\left[\ln\left(\frac{1}{1-F(x)}\right)\right] = \beta\ln(x) - \beta\ln\alpha$$

were F is the cumulative distribution function, x for example the breakdown voltage or time to breakdown and α and β are fit parameters. α denotes the value at which 63 % of the samples fail (characteristic lifetime), and β is the so-called Weibull shape parameter. The two variables give information about the spread and type of the distribution and can be used to recognize different failure mechanisms. β values <1 are usually associated with an instant mortality failure mode which is typical for defects in the manufacturing process. $\beta=1$ is the special case where the Weibull distribution has the shape of an exponential distribution which mirrors a constant failure rate. An explanation for constant failure rates are original design inefficiencies, insufficient redundancies or even misuse. β values <1 are typical for wearout modes. For β between 1 to 3, scattering in the failure data increases, making failure predictions problematic whereas at higher values the failure value becomes more predictable. For β between 3.2-3.6 the Weibull distribution has a shape similar to a normal distribution.

Thermal Properties at Low Temperature

Material properties at low temperature are important for any cryogenic engineering. The most important properties of the used insulators of a cryostat are the thermal expansion, the thermal conductivity, and the heat capacity. Because of the difficulties of low temperature measurement techniques there is only a small amount of data available regarding irradiation effects on low temperature properties of polymers and fiber polymer composites. Within this work first measurements were carried out concerning ion induced effects on the thermal conductivity and heat capacity of polyimide and G11-type epoxy/glass-fiber composite. Therefore these quantities are introduced briefly with a special focus on the used material class.

Low temperature thermal conductivity of polymers and fiber/plastic composites

The thermal conductivity of polymers is in general low compared to other materials. For the case of electrically non-conductive materials, the thermal conductivity is due to the phonon scattering at defects and statistical changes in the polymer´s density [106]. It is denoted as follows:

Equation 8 $$\lambda_{th} = {}^{1}\!/_{3}\, C_v\, u\, \Lambda$$

were C_v is the volumetric heat capacity, u the velocity of sound and Λ the phonon mean free path.

For amorphous polymers the mean free path of the phonons is nearly temperature independent and is in the order of atomic bond lengths [106]. At very low temperature the thermal conductivity of amorphous polymers is proportional to T^2, whereas in semi-crystalline polymers different behaviors are observed [107]–[109][110]. For amorphous polymers, in the temperature regime between 2 and 20 K, a plateau region is found [111][112]. This plateau region is universal for glassy materials and found for many different glasses and polymers [113]. Many different theories have been proposed to explain this behavior. One is the explanation of the simultaneous existence of long-range and short-range correlations [114].

Polyimides analyzed within this study show a proportionality to T without an observed plateau which is often explained by small crystalline regions within an amorphous matrix of the X-ray amorphous polymer [115]. Since radiation is commonly known to induce glass formation rather than crystallization it is important to measure the thermal conductivity of

irradiated polyimide in order to see whether a plateau is formed or not and if the conductivity is increased or decreased.

Thermal conductivity of polymer/glass-fiber composites

Compared to metals, fiber reinforced plastics (FRP´s) have the great advantage of low specific weight and low thermal conductivity at a high stiffness. Therefore they are commonly used as structural support and thermal insulation in low temperature applications such as superconducting magnets. In FRP´s the thermal conductivity is strongly influenced by the type of fiber and the fiber arrangements which often results in anisotropy of the composite´s thermal conductivity [116]. Overall, epoxy matrices show a lower thermal conductivity as compared to mineral-glass, carbon- and polyaramid-fibers over the whole temperature range [117]. At room temperature carbon fiber composites show the highest value of thermal conductivity whereas reinforcement of glass fibers yields the lowest. At low temperature, however, carbon and glass-fiber reinforced plastics show quite similar values. The trend of decreasing thermal conductivities at low temperature is in both cases present [40].

Low temperature specific heat of polymers and fiber composites

The specific heat determines how much energy is needed to heat a material to a given temperature. To calculate the specific heat, the various excitations that arise during thermal energy transfer have to be considered. For crystalline insulators, the most important excitations are lattice vibrations. According to the Debye model, a dependence of the specific heat with T^3 is found. This implies a strong decrease of the specific heat at low temperatures. However, disordered or glassy materials, where atoms can “tunnel” between different positions, due to small energy differences, an additional contribution is found which follows aT^n, where a is a constant and n is a value close to one [118]. Disordered insulators therefore often show a high specific heat at low temperatures, having a so-called excess specific heat at temperatures between 5-20 K. An explanation was found by Kanaya et al. who proved that the density of states of polyethylene shows an excess peak which could be explained by assuming a tunneling model [116]. The materials analyzed in this study are glassy solids (polyimide and glass-fiber reinforced plastics). The Experiments conducted to investigate the influence of ion irradiation on low temperature specific heat are discussed in chapter 5.2.

3 Material Synthesis and Experimental Methods

3.1 Synthesis of Amine Cured Polyepoxy Films

Thin cured polyepoxy films were synthesized as follows: The epoxy resin CPR862 (Bis F), having 165-173 gram per equivalent of epoxy, was mixed with DETDA (Ciba HY5200, Ethacure 100 Curativ, specific weight: 178.28 g/Mol) in a weight ratio of 100:26. The solution was stirred for at least one hour and degassed in an ultra sonic bath for about 30 minutes.

Following this procedure 2-3 drops of the solution were squeezed between two polypropylene plastic sheets which were fixed between two glass plates. To leave some distance between the two polypropylene sheets, thin polyimide foils ($\sim$25 μm in thickness) were put in between as space holders. The "sandwich" was cured at 100°C for 24 hours resulting in 18 +/- 5 μm thick polyepoxy films which were carefully striped from the polypropylene surface.

3.2 UV/Vis Spectroscopy

UV/Vis spectroscopy measures the absorption of electromagnetic waves of a sample in the ultraviolet to the visible light regime (typically between 190 and 900 nm). In this energy regime the valence electrons of molecules are excited into higher states. It is used to quantify and identify molecules and gives information about the absorption edge and band gap of a material. In organic molecules typical absorption bands and their characteristic excitation wavelengths can be classified with respect to the contributing molecular orbital. They are briefly summarized in Table 3.1.

Table 3.1 Absorption of typical organic chromophores (isolated)

Chromophor	Transition	Example	Maximum absorption wavelength (nm)
C-H	$\sigma \rightarrow \sigma^*$	CH_4	122
C-C	$\sigma \rightarrow \sigma^*$	C_2H_6	135
-O-	$n \rightarrow \sigma^*$	H_2O	167
-O-	$n \rightarrow \sigma^*$	H_3C-OH	183
C=C	$\pi \rightarrow \pi^*$	C_2H_4	165
C=O	$n \rightarrow \pi^*$	C_2H_4O	293
C=O	$\pi \rightarrow \pi^*$	C_3H_6O	187
C=O	$n \rightarrow \pi^*$	C_3H_6O	273

In case of hyperconjugation of olefins or polyenes a bathochromic shift of the absorption is found. With increasing conjugated chain length the difference in energy between the highest occupied molecular orbital (HOMO) and the lowest unoccupied molecular orbital (LUMO) of the $\pi \rightarrow \pi^*$ absorption decreases.

For polymers the HOMO/LUMO band gap is comparable to the valence and conduction band in semiconductors. Thin films of polyimide show 4 absorptions having their maxima at 218, 276, 334 and 378 nm [119], whereas thick films (>1 μm) show only one broad transition from total absorbance in the UV at wavelength <450 nm to high transmittance (80 % in the case of 12 μm thick films) at wavelength >550 nm [120][58].

In ion-irradiation studies the UV/Vis spectroscopy is commonly used as an analytical tool to follow the ion induced formation of carbon clusters [121][122] which causes the coloration of the material.

In this work, UV/Vis absorption measurements were performed in transmission configuration using an ATI UNICAM double beam spectrometer (UV4). Spectral resolution was set to 2 nm.

3.3 Infrared Spectroscopy

Electromagnetic radiation interacts with molecules having a natural or induced dipole moment. In the infrared regime the transferred energy excites vibrations and rotations of the molecule and the chemical bonds. In the infrared absorbance spectra of solid matter, rotational modes can be neglected because molecular groups are hindered to rotate freely and vibrational bands dominate. The number of possible vibration modes of a molecule depends on the number of atoms (N), its shape, and its degrees of freedom (3N-6 normal modes for nonlinear molecules). For polymer molecules consisting of thousands of atoms, spectra might be expected to be extremely complicated. Due to the nature of repeating monomer units being chemically equal this is not the case and spectra are usually not more complicated than organic molecules having a structure similar to the repeating unit [123]. The frequency of absorbance bands is connected to the atoms, the type (strength) of bonds and the environment of the vibrating bonds. The latter case is called molecular interaction and describes the influence between neighboring molecules.

The several absorption bands found for different functional groups in organic molecules are classified in so called group vibrations and are used for identification of organic molecules and their structure. Common absorption bands in the mid-IR ($\tilde{\nu}$~4000-400 cm^{-1}) relevant for this work are briefly summarized in Table 3.2 according to the literature [124]. It should be noted that the wavenumber regime <1500 cm^{-1} is called fingerprint region because many functional groups show their skeletal vibrations.

Table 3.2 Overview of some functional groups and their typical IR absorption bands

Wavenumber region of absorption band/ cm^{-1}	Functional group
3600-2800	-OH
3400-3200	-CH
3050-3150	unsaturated -CH
2960-2700	saturated -CH
2280-2100	triple bond
1800-1700	carbonyls
1700-1600	carbon double bonds
<1500	finger print region

Usually the analysis of the fingerprint region cannot be interpreted as precisely as the region above 1500 cm^{-1} due to strong overlapping of various absorption bands, but can often be useful for comparative analysis for substance analysis.

Suppression of Background Undulations

In the case of IR measurements in transmission geometry, background undulations can emerge and may disturb appropriate analysis of data (Fig. 3.1, black line in marked box). These undulations are caused by interferences of light reflected at the two surfaces of the sample. Suppression of these undulations can be performed via tilting the sample into the Brewster angle and using a polarized beam. The polarization of a reflected beam has its maximum at the Brewster angle interference effects are suppressed using an appropriate polarized IR beam (Fig. 3.1, red line). A typical polarizer in IR measurements is Grid-polarizer made of an IR transparent material such as CaF_2 or ZnSe sputter-coated with an aluminum or gold-grid.

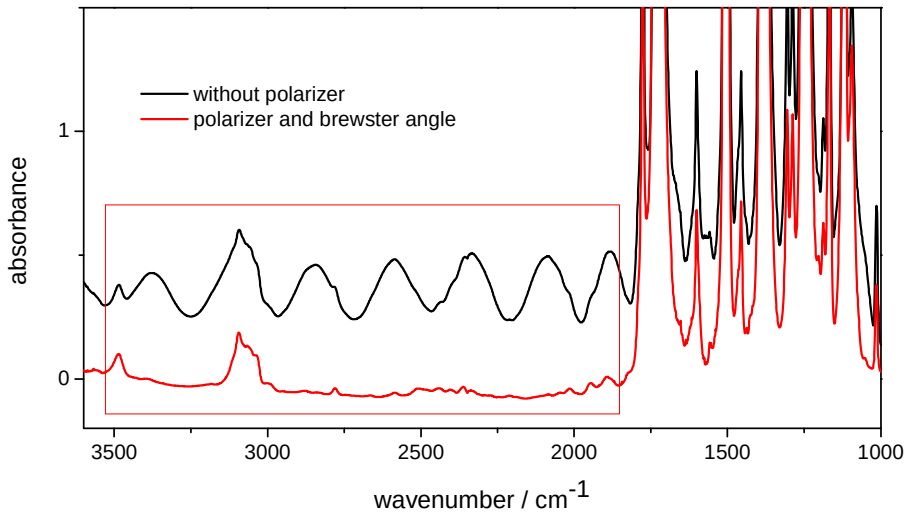

Fig. 3.1 Infrared spectrum of polyimide under standard geometry (black line) and spectrum using a polarized beam and Brewster´s angle

Attenuated Total Reflection Spectroscopy

The Attenuated Total Reflection (ATR) spectroscopy belongs to the reflection methods used in IR spectroscopy. Its usage is (i) to analyze the surfaces of samples or (ii) to measure powders and liquids without special preparation techniques such as nujol mule, pressing a KBr pellet or usage of a cuvette.

ATR-IR spectroscopy is based on the total reflection at the interface of a non IR absorbing material with high refractive index and a material having lower refractive index. Surface plasmons are created with wave front perpendicular to the surface of the reflecting plane.

When the material with light refractive index shows IR absorption, this wave is absorbed and the total reflection shows attenuation [125]. In this way, IR absorption spectra provide information from the surface of the sample. The penetration depth of IR-radiation in polymers is typically in the range of a few micrometers. The intensities in ATR are strongly dependent on the measured material. The quality of the spectra depends on its refractive index and the surface contact area between sample and the ATR-material. Glass-fiber composite materials cannot be studied using infrared spectroscopy in transmission mode due to the strong infrared absorption of the glass fiber and its large thickness. To access beam-induced changes of the polyepoxy matrix thin polyepoxy foils were synthesized. However, the glass-fibers of a composite may influence the degradation behavior of the composite´s polymeric matrix. To compare ion beam induced changes in the chemical structure of the matrix with and without fibers, the ATR-FT-IR spectroscopy was used to verify the results obtained from the transmission measurements.

IR Spectra of the Used Materials

Polyimide:

Fig. 3.2 shows the IR spectrum of non-irradiated Kapton H type (PMDA-ODA) polyimide.

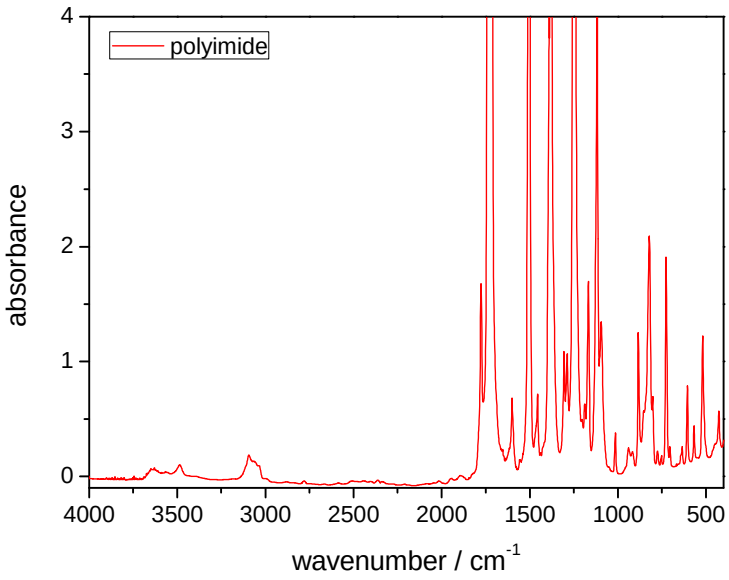

Fig. 3.2 Infrared spectrum of 12 μm Kapton-type polyimide in transmission geometry

In the wavenumber regime between 3750-3000 cm^{-1} several weak bands are found which are interpreted as O-H (3700-3500 cm^{-1}) and N-H stretching (3500-3300 cm^{-1}) bands from non-reacted amines and/or polyamic acids as well as the more intense C-H stretching modes (3300-3000 cm^{-1}) derived from the aromatic hydrocarbons. In the lower wavenumber region the first two intense peaks appear at 1776 and 1726 cm^{-1}. Both bands are assigned to the carbonyl group stretching vibration. The splitting into two bands, where the first band always show a lower intensity, is typical for carbonyls within cyclic imides and cyclic anhydrides and is explained in terms of an in-phase and out-of-phase coupling between the two carbonyls in the ring [126]. Isoimides which are a side product of the cyclization of polyamic acids show a carbonyl absorption in the range between 1820-1795 cm^{-1} [127]. In our spectra no significant amount of an isoimide band is found. In the case of crystalline polyimides a splitting of each carbonyl bands into two bands often occurs, which allows the argumentation that in the case of Kapton-type polyimide no significant amount of crystalline fraction is present due to the absence of this second splitting [128]. In the regime of lower wavelength, various bands are found and assigned to the double bond vibrations of the phenyl rings (1625-1400 cm^{-1}) as well as vibrations belonging to carbon-nitrogen bonds of the imide ring (1119 cm^{-1}) and the

aromatic ether vibrations (1380-1300). Spectral assignments are briefly summarized in Table 3.3 and done according to the literature [119], [128]–[133][134]. It should be noted that assignments in the fingerprint region (<1500 cm^{-1}) are difficult and can be misinterpreted due to overlapping of bands.

Table 3.3 Tentative assignments of the absorption bands of polyimide

wavenumber / cm^{-1}	tentative assignment
3637	ν(OH)
3563	ν(OH)(NH)
3485	ν(OH)(NH)
3094	ν(CH) arom.
3065	ν(CH) arom.
3036	ν(CH) arom.
1776	ν(C=O) in-phase
1726	ν(C=O) out-of-phase
1601	ν C_6H_5
1585	ν C_6H_5
1504	ν C_6H_5
1455	ν C_6H_5
1382	ν(CN)$(OC)_2$NC
1305	ν C_6H_5
1284	ring stretching arom. ether
1245	ν_{as} (COC) arom. ether
1187	ν C_6H_5
1166	ν C_6H_5
1119	imide $(OC)_2$NC
1094	imide $(OC)_2$NC
1013	ν 1,2,4,5-C_6H_2
884	(γ 1,2,4,5-C_6H_2)(*)
821	(γ 1,2,4,5-C_6H_2)(*)
752	(δ imide ring)(*)
726	ν C_6H_5
704	(δ imide ring)(*)
634	ν C_6H_5
605	ν C_6H_5
567	(δ imide ring)(*)
518	(δ imide ring)(*)
426	ν (amide) polyamic acid*

(*)=probative assignments

Amine cured polyepoxy

Fig. 3.3 shows the infrared spectrum of amine cured polyepoxy obtained as described in chapter 3.1. The spectrum shows in the high wavenumber regime two strong and broad

absorptions of the alcoholic hydroxyl groups (3600-3100 cm^{-1}) as well as weak and strong symmetric and antisymmetric vibrations of aromatic (>3000 cm^{-1}) and aliphatic (<3000) C-H bonds, respectively. The bands above 3000 cm^{-1} probably suffer some interference due to the methylene stretching of left over oxirane rings (uncured epoxy starting material) [135]. In any case, these bands show weak signal intensities and are not used for further analysis/interpretation. In the regime 1700-800 cm^{-1} several strong absorption bands appear. The bands between 1680-1509 cm^{-1} are assigned to the vibrations deriving from the aromatic double bonds and probably contribution from carbon-nitrogen bond vibrations. The band at 1452 cm^{-1} is assigned as a deformation of aliphatic methylene whereas bands at 1242 and 1113 cm^{-1} are ascribed as the asymmetric C-O-C vibrations of the aromatic ether linkage. The band at 821 cm^{-1} may be interpreted as deformation of the aromatic ring or the oxirane ring. Distinguishing between these two bands is not possible, but after the curing procedure only a small amount of left over epoxy is expected because of the extent of curing agent. Assignments are summarized in Table 3.4 and were performed according to the literature [135]–[141].

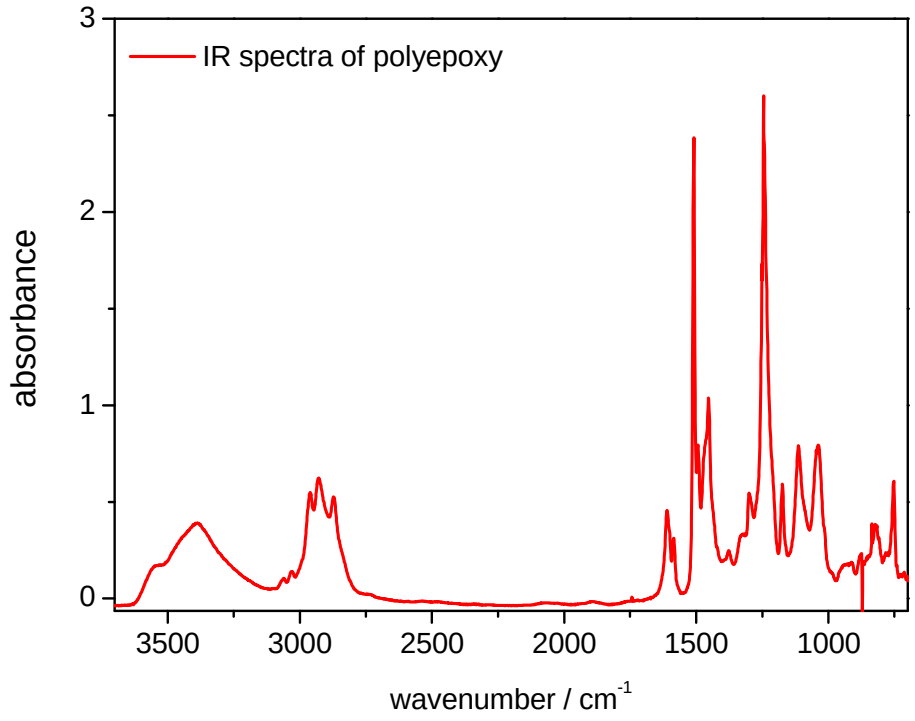

Fig. 3.3 Infrared spectrum of 18 μm thick polyepoxy film measured in transmission geometry

Table 3.4 IR absorption band assignments of amine cured polyepoxy foils

wavenumber / cm^{-1}	tentative assignment
3585	ν(OH)
3385	ν(OH)
3099	ν(CH) arom.
3060	ν(CH) arom.
3029	ν(CH) arom.
2961	ν(CH) aliphatic
2928	ν(CH) aliphatic
2872	ν(CH) aliphatic
1610	ν C_6H_5
1585	ν C_6H_5, (CNC)
1509	ν C_6H_5
1452	δ(CH) aliphatic
1242	ν_{as}(COC) arom. ether
1113	ν_{as}(COC) arom. ether
821	δ(CH) bisphenyl (terminal epoxy)

ATR-IR Spectra of G11-Type Epoxy/Fiber Composite

Fig. 3.4 shows the obtained ATR spectrum of glass-fiber reinforced polyepoxy of the G11-type used in this study. The spectrum is shown without wavenumber intensity correction (such as Kramer-König) which is commonly used to correct the fact that absorption intensities of ATR spectra have a wavenumber dependence which comes mainly from the difference in refractive indices between the ATR crystal and the analyte. Since radiation may change the refractive index as well as the chemical structure (and other properties) no correction was included.

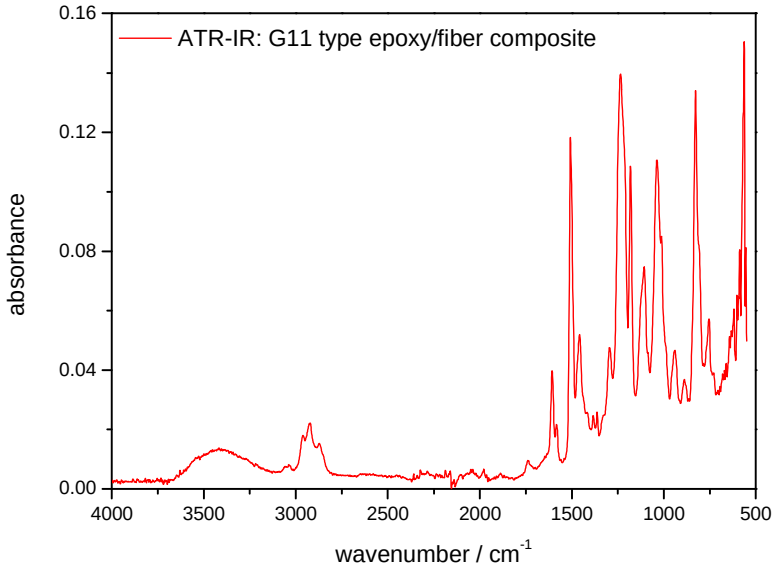

Fig. 3.4 ATR-IR spectrum of G11-type glass-fiber reinforced plastic

The spectrum shows similar features as the synthesized cured polyepoxy films measured in transmission. However, some differences are found. At high wavenumbers only one broad hydroxyl absorption band is found at 3422 cm^{-1} (in the case of cured polyepoxy films two absorption bands were found at 3585 and 3385 cm^{-1}). The reason for this may be a different amine hardener concentration in the synthesis-protocol as well as usage of different temperatures (which are company secrets). Given by the three main reactions of epoxy curing with amine hardeners (see page 8) this could mean that in the case of synthesized epoxy, some non-reacted secondary amine hydroxyl groups are present while in the case of the commercial composite the curing reaction is complete. The next difference is found in a variety of additional bands at 1739, 1293, 1180, 1036, 940, 755 and 562 cm^{-1}. These bands are assigned to the coupling-agents which are typically added for better adhesion/connection between the glass fibers and the polymeric matrix. Typical coupling-agents for glass-fiber composites contain silane coupling agents which form covalent bonds with the glass-fiber. Therefore most of the mentioned bands originate from carbonyl groups (1739 cm^{-1}), e.g., from methacryloxypropyltrimethoxy-silane (MPS) one of the standard coupling agents with Si-O-Si vibrations and various hydrocarbon vibrations [142]–[145]. Since the used coupling agent is not known a clear assignment is impossible.

Table 3.5 ATR-IR absorption bands of G11-type GFRP and tentative assignments

wavenumber / cm^{-1}	tentative assignment
3422	ν(OH)
3057	ν(CH) arom.
3035	ν(CH) arom.
2960	ν(CH) aliphatic
2924	ν(CH) aliphatic
2872	ν(CH) aliphatic
1739	ν(C=O) coupling agent (*)
1606	ν C_6H_5
1581	ν C_6H_5, (CNC)
1507	ν C_6H_5
1457	δ(CH) aliphatic
1293	coupling agent (*)
1234	ν_{as}(COC) arom. ether
1180	ν (SiOSi) coupling agent (*)
1113	ν_{as}(COC) arom. ether
1036	ν (SiOSi) coupling agent (*)
940	coupling agent (*)
824	δ(CH) bisphenyl (terminal epoxy) (*)
755	coupling agent (*)
562	coupling agent (*)

(*) = probative assignments

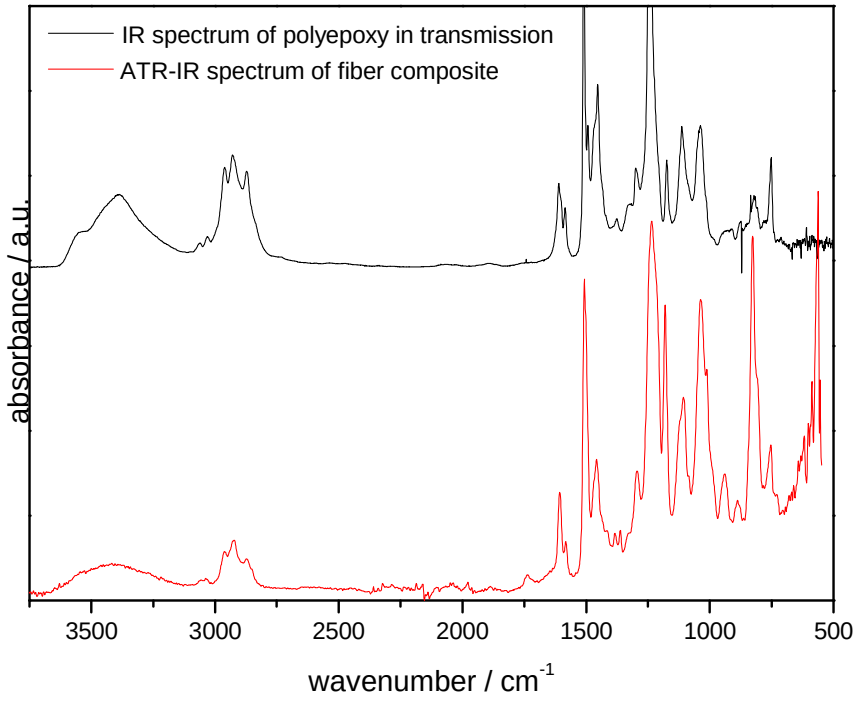

Fig. 3.5 IR spectra of thin cured polyepoxy films measured in transmission mode and commercial epoxy/fiber composite measured with ATR-IR

Instrumentation

Ex situ FT-IR: Infrared measurements were performed using a Nicolet FT-IR spectrometer (Magna-IR 550 with TGS detector). If not otherwise noted the spectra were collected using 16 co-added scans with a resolution of 2 cm^{-1}.

In situ FT-IR: A description of the IR set-up used for in situ FT-IR measurements at the M-Branch can be found in chapter 4.4.

ATR-FT-IR: A single reflection diamond ATR accessory (Specac Ltd., Golden Gate) was used to measure IR absorbance of G11-type epoxy/fiber surfaces.

Polarizer: For suppressions of interferences of reflections a KRS 5 Grid polarizer supplied by LOT Oriel in Darmstadt was used.

3.4 Evolved Gas Analysis (EGA) and Ion Induced Residual Gas Analysis (RGA)

Evolved gas analysis is a technique to follow and determine the formation of volatile species during the degradation (e.g. combustion) of materials. It involves several techniques and/or coupling of techniques such as Thermal Gravimetry (TG) coupled with IR/MS or Pyrolysis-GC-MS. EGA is especially applied to determine degradation mechanisms by means of analyzing the different reaction pathways semi-quantitatively and qualitatively. The method is divided into techniques using continuous mode and intermittent mode. In the first case the gaseous sample is directly introduced into the detector system via an interface while in the latter case the analyzing species are trapped (for example at low temperature) and after accumulation are introduced into the detector system [146]. In this work Thermal Gravimetry (TG), coupled with a quadrupole mass spectrometer (QMS), was used to determine the decomposition products of non-irradiated and irradiated polyimide, qualitatively. Whereas ion induced outgassing was measured in combination with in-situ IR spectroscopy (as described in chapter 4.4) to directly analyze the radiolytic gaseous species of polyimide and G11-type polyepoxy.

Thermal Gravimetry Coupled with Mass Spectrometry

TG analysis measures the weight of a given sample while heating and is a standard characterization method of polymers. Coupling this analyzing technique with a mass spectrometer introduces the opportunity of following and characterizing the evolved gases during each step of the pyrolysis. Both techniques can give useful information about (i) the chemical structure of the analyzed sample and (ii) the involved degradation mechanisms. This method is commonly used in polymer science to determine the thermal stability of a given polymer. Thermal degradation of polymers occurs when the temperature is high enough to break primary bonds. Some polymers tend to form back into monomer (chain depolymerization or unzipping) while others create a great amount of different degradation products (random degradation). Thermal degradation is characterized by the following values which can be extracted from TG curves and the corresponding mass spectra:

$T_{(d,0)}$: Temperature of initial decomposition. Temperature at which the weight loss starts to become measurable. (The typical value of 5% was used in this study.)

$T_{(d,1/2)}$ Temperature of half decomposition. In a non isothermal experiment the temperature at which the weight loss reaches 50 % of its final value.

$T_{(d,max)}$ Temperature of the maximum rate of decomposition. Taken from the derivative of the TG curve.

$E_{(act,d)}$ The average activation energy of the degradation process.

In TG-MS measurements the combustion gases of the thermal degradation are introduced into a mass spectrometer (usually a quadrupole mass spectrometer) for further analysis (see Fig. 3.6). Identification of gaseous degradation products in combination with the temperature of gas evolution is used to give information about the underlying degradation mechanism on a molecular level. Other techniques exist such as coupling with an IR spectrometer and/or a gas chromatograph coupled with a mass spectrometer, such as Pyrolysis-GC-MS, but were not used in this study.

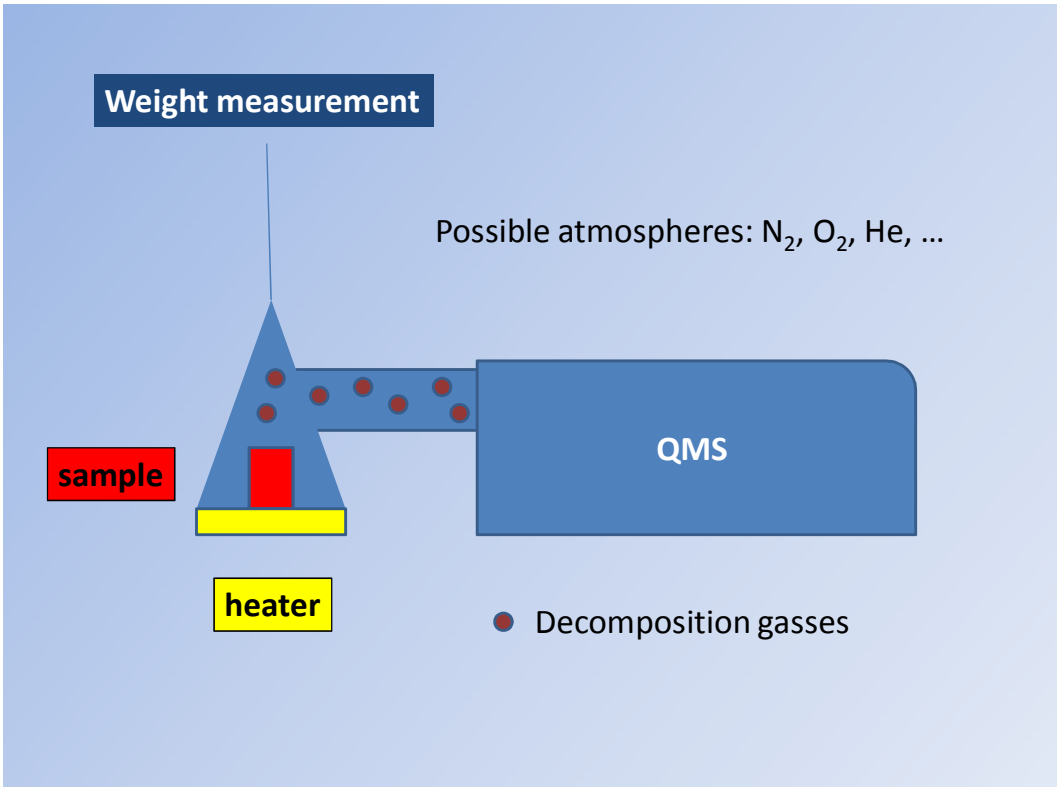

Fig. 3.6 Schematics of TGA-MS set up

Radiation Induced Residual Gas Analysis

Residual gas analysis is a standard tool to follow radiation induced degradation processes in organic materials [147]. Usually, for gamma induced degradation a quartz vessel is irradiated and the outgassing products are accumulated, later to be injected into a GC-MS or other gas analyzing tool which allows identification and quantification of the outgassing products [148], [149]. In ion induced degradation studies this is usually not possible due to the low penetration depth of the ions, therefore experiments are performed in-situ or on-line during the irradiation via a quadrupole mass spectrometer in the irradiation chamber. In some cases the irradiated sample is additionally connected to a cryostat to accumulate the outgassing products via freezing volatile species at low temperature [58]. Subsequent heating allows the separation of different combustion gases in dependence of their boiling point under the specific pressure of the chamber. In contrast to the useful opportunity of identifying ion induced degradation products the quantification is difficult because of interferences due to overlapping mass peaks and the usually unknown pumping speed of the system for different gases in different pressure regimes. In cryogenic irradiation experiments, for example, the chamber´s gas pressure is dependent on the amount of outgassing analyte. However, the boiling point of gases depends on the pressure. This leads to problems with the clear separation, since the outgassing of one species will increase the pressure of the chamber and other species with a lower boiling temperature will also start to gas out of the material. In this thesis ion induced outgassing was therefore used qualitatively. A detailed description of the experimental set up can be found in chapter 4.4.

3.5 Measurements of Thermal Conductivity at Low Temperature

The apparatus used to measure the thermal conductivity of polyimide foils is based on the method of unidirectional heat flow according to reference [150]. A sample holder was prepared fixing the specimen between two copper blocks as shown in Fig. 3.7. The upper copper block (B in Fig. 3.7) can be heated via a resistor. The temperature of both blocks is measured using silicon diodes (T-sensors). This holder was mounted on the cold finger of a Gifford-McMahon refrigerator (see Fig. 3.9).

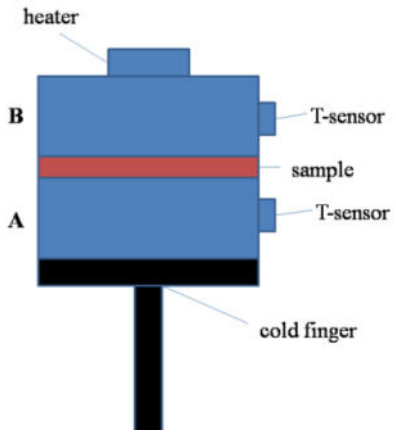

Fig. 3.7 Schematic view of the apparatus used for measuring the thermal conductivity of polyimide foils. Note that for better clarity no cabling or thermal shielding is shown in the figure.

Steady state measurements on 125 μm polyimide specimen were performed inside the cryochamber at a pressure of 2×10^{-4} Pa and mean temperatures between 6 and 100 K.

Thermal conductivity was measured in "through thickness direction" and calculated using equation 9. The thermal gradient applied to measure the thermal conductivity was in the range of 1-3 K as shown in Fig. 3.8. The procedure included the change of base temperature via heating the cold finger of the cryostat. After a constant base temperature was reached the heater of copper block B was turned on efficiently heating the upper copper block. Again after reaching a steady state the heater of the copper block was turned off while the heater of the cooling finger was powered with more voltage to reach the next base temperature.

Equation 9:
$$\lambda_{th} = \dot{Q} \times \frac{A}{l} \times \Delta T$$

with λ_{th} being the thermal conductivity in W/mK, $\dot{Q}$ the heat flow in Watt, A the sample area in square meter, l the thickness of the sample in meter and ΔT the applied temperature gradient in Kelvin.

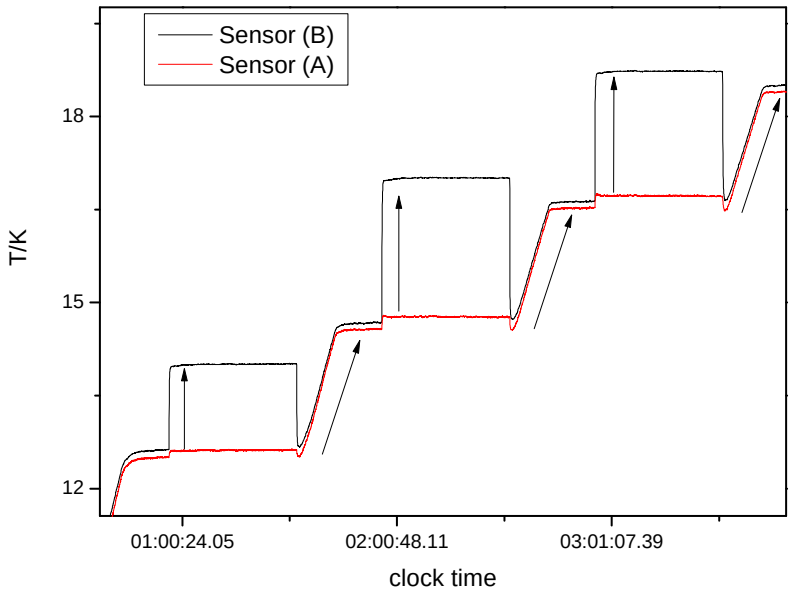

Fig. 3.8 Example of used temperature program during low T thermal conductivity measurement

A reproducibility test was performed (see chapter 5.1) by cutting 3 similar samples out of one non-irradiated polyimide foil. The reproducibility in all 3 measurements was better than 10 %. The thermal properties of the holder itself are known from reference measurements without sample.

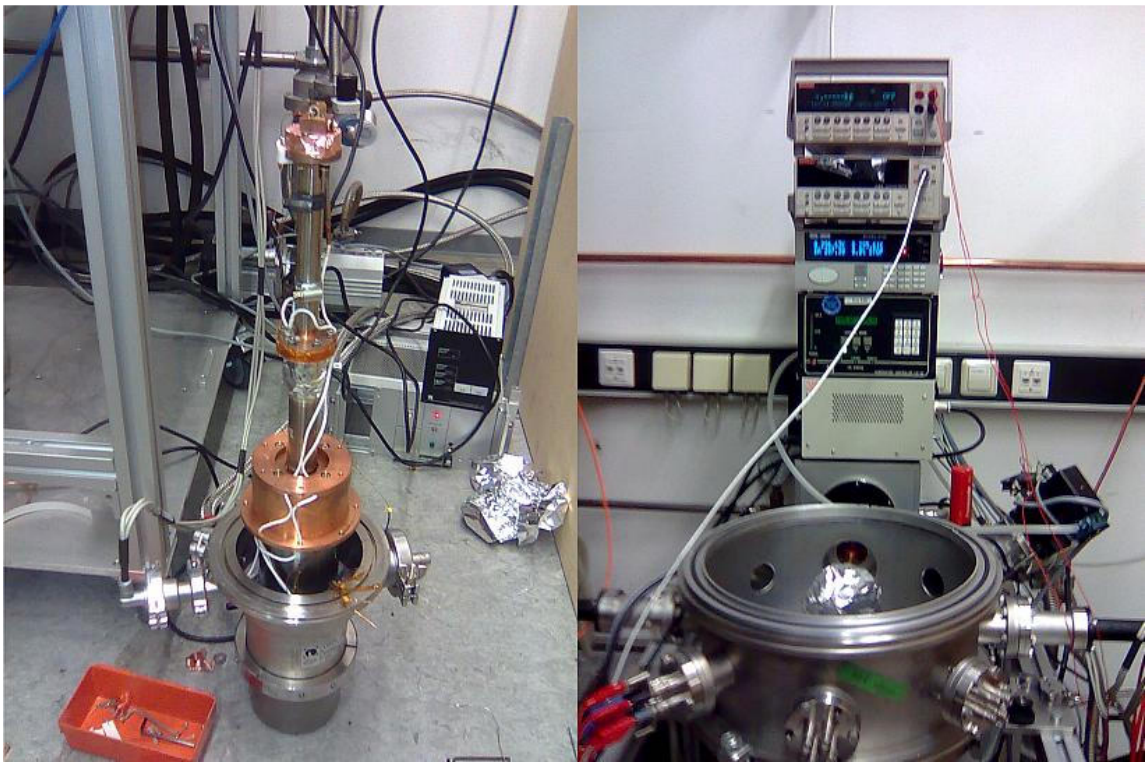

Fig. 3.9 Photographs of the cooling finger (left) and the vacuum chamber of the cryostat (right)

3.6 Specific Heat Measurements at Low Temperature

Specific heat was measured on a commercial Physical Property Measurement System (PPMS) from Quantum Design. The PPMS is an automated measurement device combining multiple measurement options of material properties such as Hall effect, electrical resistivity, thermal conductivity and last but not least specific heat. It can operate at temperatures ranging from 1.9 to 400 K.

In this device the method used to determine the specific heat is based on thermal relaxation calorimetry (TRC). This method measures the specific heat of a sample by recording the heat response of a sample/holder assembly [151]. The sample of unknown heat capacity is attached with conductive grease to a calorimeter platform. The calorimeter platform consists out of a 3x3 mm^2 alumina square with a thin film heater and a bare Cernox^{TM} sensor. Thin wires are used to link the platform electronically and thermally to the bath of the cryostat. The measurement can be divided into two steps. (i) Measuring the calorimeter assembly comprising out of the platform, the heater, the sensor and the conductive grease without sample (so called addenda) and (ii) the measurement of the same assembly with the sample. Assuming a good thermal connection between the sample and the platform the specific heat is determined through a special fitting technique described in the literature [152]. The overall accuracy of this set up on referenced standard samples is found to be better than 1 % at temperatures between 100-300 K and <5 % at temperatures down to 1.9 K [153].

Fig. 3.10 PPMS measurement device (left) and the heat capacity sample holder (right)

3.7 Dielectric Strength Measurements

Polyimide:

All dielectric breakdown voltage measurements were performed in ambient atmosphere. The humidity and temperature were 35-45 % and 22-24°C, respectively. The electrodes consisted of cylindrical stainless steel plates of 12 mm in diameter with a rounded edge of 1 mm (Fig. 3.11). To ensure a good electrical contact to the sample, the two electrodes with the irradiated foils (5x5 cm^2) in between were screwed against each other.

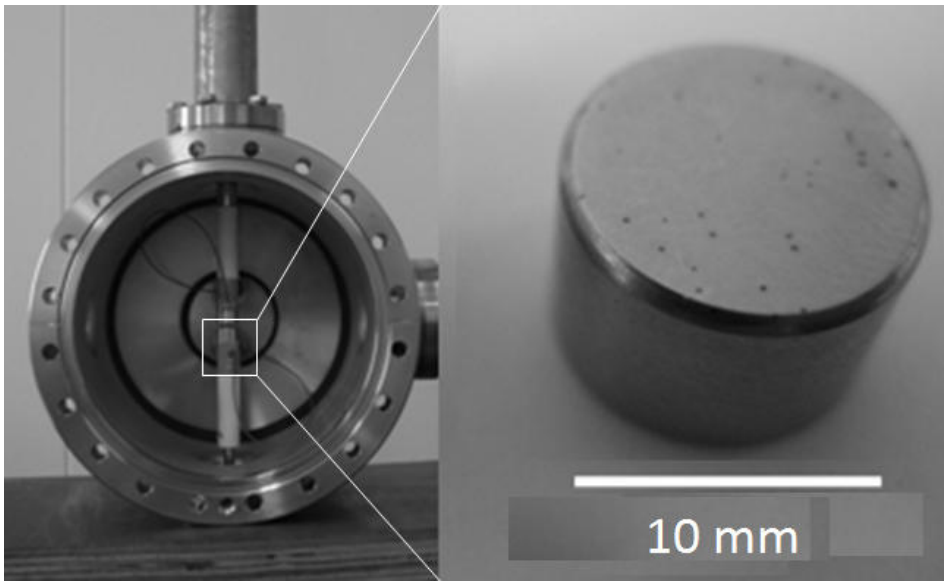

Fig. 3.11 High voltage test set up (left), side and top view of Rogowski-type electrodes with a flat diameter of 10 mm (right)

Dielectric strength measurements were performed by ramping a DC voltage at a rate of 1.2 kV/s and monitoring the breakdown voltage by means of a high voltage probe. The instrumental voltage limit was 18.5 kV. For a 25 μm thick polyimide foil, 18.5 kV corresponds to a dielectric field of 740 kV/mm exceeding the dielectric strength of virgin polyimide by a factor of two. A series resistor limited the breakdown current to 18 mA in order to avoid excessive sample degradation after breakdown. Current measurements were performed by a voltage divider and an oscillocope of $\sim$ 1 μA minimum current limitation.

Voltage breakdown resulted in a clearly visible hole punctured through the sample that was inspected by standard optical and scanning electron microscopy. The majority of holes was found to be inside the flat area of the electrodes indicating that electrical field variations due to the geometry of the electrodes did not influence the measurements.

For non-irradiated samples our measurements yield a dielectric strength of about 365 kV/mm for 50 μm thick foils and 430 kV/mm for 25 μm thick foils. According to the manufacturer, the dielectric strength of Kapton HN measured with standard test methods (AC-Voltage 60 Hz, ASTM D149-91) is slightly lower, 240 kV/mm (50 μm film) and 303 kV/mm (25 μm film) [154]. Higher dielectric strength values obtained when using DC voltage are in agreement with literature [99]. No significant difference in dielectric strength was found between Apical AV and Kapton HN foils in agreement with Hammoud et al. [155].

G11

Glass-fiber reinforced plastics, typically having a dielectric strength in the order of 40-60 kV/mm, were measured at the high voltage laboratory of the Technical University of Darmstadt. Samples of 1-1.5 mm thickness were measured in silicon oil to avoid flash-over because of the high voltages used necessary to break the material. Electrodes were round stainless steel electrodes having a diameter of 15 mm. Two types of test were performed. (i) Using a DC voltage ramping of about 1.2 kV/s and (ii) using a 50 Hz AC voltage ramped at about 1.2 kV/s.

Weibull analysis of dielectric strength data

Weibull analysis as described in chapter 2.3 was performed using probability plotting according to the literature [105], [104] and Excell2007 for Weibull-data determination [156].

4 Irradiation Experiments

As presented in chapter 1.6, the expected radiation field to FAIR magnets and their components is a complex mixture of gamma, neutron and ion radiation. The goal of this thesis was (i) to provide useful engineering data for the magnet design and (ii) to perform systematic research studies trying to gain a better understanding of observed degradation. Therefore irradiations with gammas, neutrons, and protons, light and heavy ions of different energies were performed. In addition several samples were exposed to a secondary radiation field produced via the fragmentation of a high energy uranium beam. The irradiation experiments took place at different institutes and accelerators in Germany and Russia, i.e. GSI Helmholtz Center of Heavy Ion Research (Darmstadt, Germany), TU Munich (Germany), and Institute for Theoretical and Experimental Physics (ITEP, Moscow, Russia).

While heavy ion irradiations at energies limited to several MeV/u leads to minor radiation induced radioactivity, high energy irradiations with light ions, neutrons and secondary field irradiation induce high sample activation. Decay times, necessary to secure safe handling and transport of samples may require years. This chapter summarizes the irradiation conditions of the different experiments and briefly describes the irradiation facilities. Some of the experiments were combined irradiations of several groups and the list of irradiated samples does not only show samples measured within this thesis unless mentioned otherwise.

4.1 Important Units

The definitions of the most important units are briefly introduced:

(Particle) Fluence:

The particle fluence is defined as the number of particles that intersect a unit area.

$$\Phi = \frac{dN}{dA}\left[\frac{ions}{cm^2}\right]$$

(Particle) Flux:

In particle physics the flux is described as the intensity of an ion beam. It is a term referring to the number of particles passing through an area per time unit.

$$Flux = \frac{\Phi}{t}\left[\frac{ions}{s \cdot cm^2}\right]$$

Dose:

The absorbed dose is used to determine the amount of energy deposited in a certain volume of matter. It is defined by its SI Unit in J/kg equivalent to Gray (Gy).

$$D = \frac{E}{m}\left[\frac{J}{kg} = Gy\right]$$

To determine the absorbed dose which an irradiated sample received, one needs to calculate the deposited energy of a certain volume of the sample. This absorbed energy can be calculated taking the energy loss (–dE/dx) vs. depth function of the TRIM2008 program. Taking into account the density and the thickness of the sample, the following equation is used:

Equation 6

$$D = \frac{e \cdot \Delta E \cdot \Phi}{d \cdot \rho}$$

with e being the elementary charge, d the thickness, ρ the density, ϕ the fluence and ΔE the deposited energy.

4.2 Gamma Rays

Polyimide samples (Kapton HN^{TM}) were irradiated with a ^{60}Co-source at the TU Munich. For optical spectroscopy 12 μm foils were used, whereas for dielectric strength measurements samples with a thickness of 50 μm were used. The dose rate of the ^{60}Co-source is known to be about 3 kGy/h from prior calibrations. The irradiation was performed in air.
Gamma exposures applied covered a dose range from 1 to 27.7 MGy. The time for accumulating the highest dose (~28 MGy) is about one year. Table 4.1 summarizes the irradiation experiment.

Table 4.1 List of gamma irradiated samples with dose and performed analysis

Sample Name	Dose (MGy)	Type of Test
G-1 (12&50 μm Kapton HN)	1	IR, UV/Vis, DS-Test
G-2 (12&50 μm Kapton HN)	6.6	IR, UV/Vis, DS-Test
G-3 (12&50 μm Kapton HN)	12.25	IR, UV/Vis, DS-Test
G-4 (12&50 μm Kapton HN)	27.7	IR, UV/Vis, DS-Test

4.3 Protons & Neutrons

All experiments with protons and neutrons took place at the ITEP in Moscow. ITEP consists of a 25 MeV proton LINAC coupled to a synchrotron which provides proton beams up to 10 GeV.

Proton Irradiation with 21 MeV

Irradiation experiments with 21-MeV protons were carried out at the I-2 linear proton accelerator at ITEP, Moscow [157]. A stack of polyimide- and GFRP-samples (see Table 4.2 and Fig. 4.2) were irradiated together with magnetic alloy samples and two “alanine” dose monitors. Sample stacks were mounted on a movable sample holder (Fig. 4.1) allowing

movement of them into and out of the beam via remote control. The irradiation was performed in air at room temperature. The range of the 21-MeV proton beam is about 3.5 mm (calc. with SRIM2010) Important beam parameters are given in Table 4.2.

Table 4.2 List of 21 MeV proton irradiated samples with fluence and dose

Ion species		Protons
Beam energy, MeV		21
Mean flux, $cm^{-2}s^{-1}$		$3x10^{10}$
Sample	Fluence, p/cm^2	Dose, MGy
Dose monitor	$4.0x10^{14}$	1.34
Dose monitor	$2.0x10^{14}$	0.67
Foil stack 1	$2.0x10^{14}$	0.8
Foil stack 2	$4.0x10^{14}$	1.6
Foil stack 3	$8.0x10^{14}$	3.3
Foil stack 4	$2.0x10^{15}$	6.7
Foil stack 5	$4.0x10^{15}$	13.5
Foil stack 6	$8.0x10^{15}$	26.9
Foil stack 7	$2.0x10^{16}$	82

Fig. 4.1 Photograph of the irradiation set up

Beam flux and the respective fluence/dose listed in Table 4.2 are averaged over the irradiation aperture with a diameter of 35 mm. The Beam flux was monitored during the irradiation by means of a current transformer which was calibrated via a Faraday cup. Each of the foil stacks (1-7) consisted of 2x12 μm, 4x25 μm and 12x50 μm Kapton HN type polyimide foils, a magnetic alloy ribbon and two tensile test specimen consisting of G11-type glass-fiber reinforced plastic (G11). The latter two sample types were irradiated by the magnetic design department and the results from these samples are not part of this thesis.

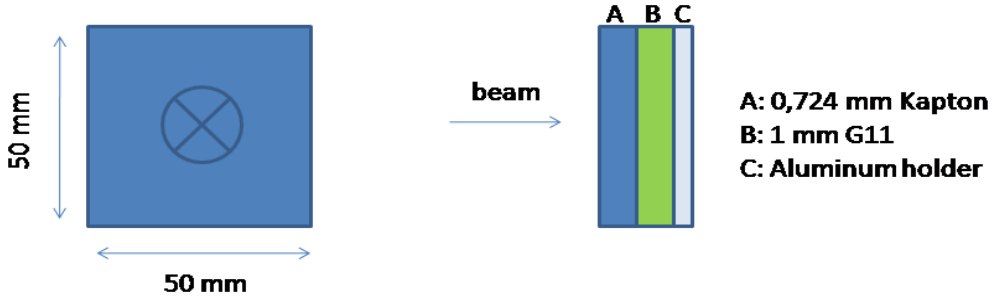

Fig. 4.2 Scheme of the foil stack of samples

Proton Irradiation with 800 MeV

A second irradiation session was carried out at the U-10 synchrotron at ITEP. Two sample stacks consisting of Kapton foils, magnetic alloy ribbons, G11 fiberglass tensile test specimen, and copper alloy wires were irradiated with primary protons of a kinetic energy of 800 MeV. Two fluences were applied ($\phi = 1.26 \times 10^{15}$ and 2.38×10^{16} cm^{-2}) and the thickness of the two stacks was chosen less than the range of the proton beam. The proton beam penetrated through the sample stacks and was stopped in a tungsten target thereby producing fast secondary neutrons and protons (Fig. 4.3).

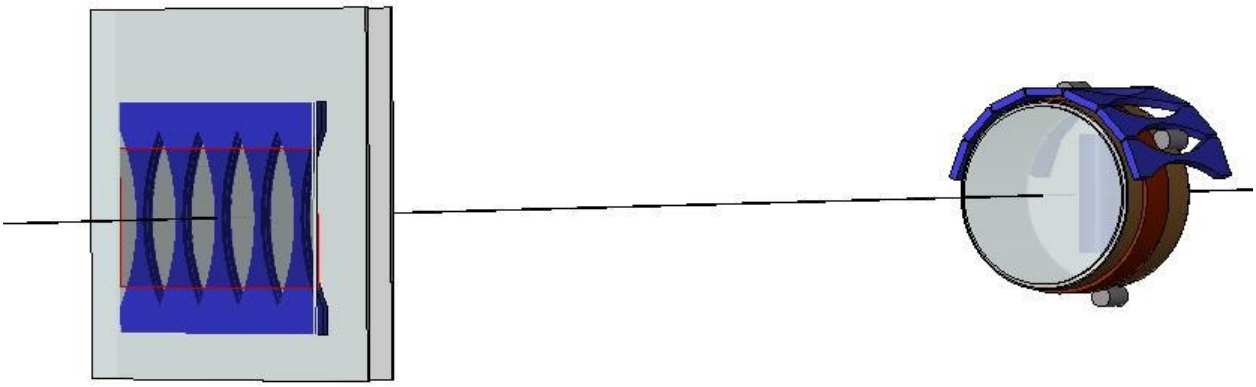

Fig. 4.3 Schematic view of the irradiation configuration of the 800 MeV proton irradiation. The proton beam (coming from the left) penetrates the sample stacks (left) and is stopped in the tungsten cylinder (right).

The two similar sample stacks (designated as P800A and P800B) were assembled in the following manner: Ten 2 mm thick G11 tensile specimen were placed (in two rows, see Fig. 4.4) on a aluminum plate, then ten layers of magnetic alloy, 20 polyimide foils (2x12 μm, 4x25 μm and 12x50 μm Kapton HN type polyimide), and one aluminum foil for proton fluence scoring (50x50 mm^2) were attached. The assembly of the sample P800A is shown in Fig. 4.4. P800A was exposed to the beam with the aluminum foil facing the beam for the entire duration of the irradiation while the sample P800B was placed behind sample P800A and was removed halfway through irradiation time.

The target for the neutron irradiation was a tungsten cylinder (length 33 mm and diameter 44 mm) around which a few layers of polyimide (Kapton) and a copper-alloy wire were coiled. Seven G11 tensile test specimen and three alanine dose monitors were placed above

the polyimide layers. Additionally, at the back side of the tungsten target two G11 compression samples and another dose monitor were mounted.

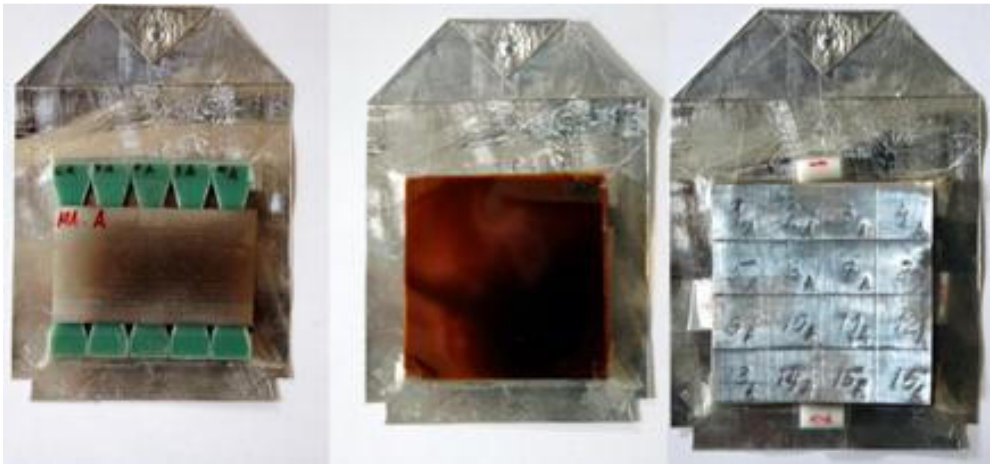

Fig. 4.4 Sample arrangement of the 800 MeV proton irradiation experiment

The total proton fluence applied to the samples P800A and P800B was recorded by the reaction rate of Al(p,x) ^{7}Be and Al(p,x) ^{22}Na reactions. So the amount of radioactivity in the aluminum foil was measured after the irradiation and was recalculated to obtain the fluence.

Table 4.3 Summary of samples irradiated with protons and neutrons

Sample Name	Fluence / cm^{-2}
P800-A	1.26×10^{15} (1.5 MGy)
P800-B	2.38×10^{16} (3 MGy)
N	$\sim2\times10^{16}$

4.4 Heavy Ion Irradiation

All irradiations with heavy ions or fragmented beams, using heavy ions as primary beam, were performed at the GSI Helmholtz Center of Heavy Ion Research in Darmstadt Germany. GSI consists of a linear accelerator (UNILAC) serving as injector of the synchrotron (SIS18). The 120 m long UNILAC can accelerate all elements up to the heaviest naturally occurring element, uranium, with energies up to 11.4 MeV/u and is operated in pulsed mode. Each 20 ms a beampulse with a maximum length of 5 ms is generated. The synchrotron can further accelerate these ions to about 2 GeV/u (~90 % speed of light) [158]. Irradiations took place at several irradiation sites as shown in Fig. 4.5. They are briefly described in the following section.

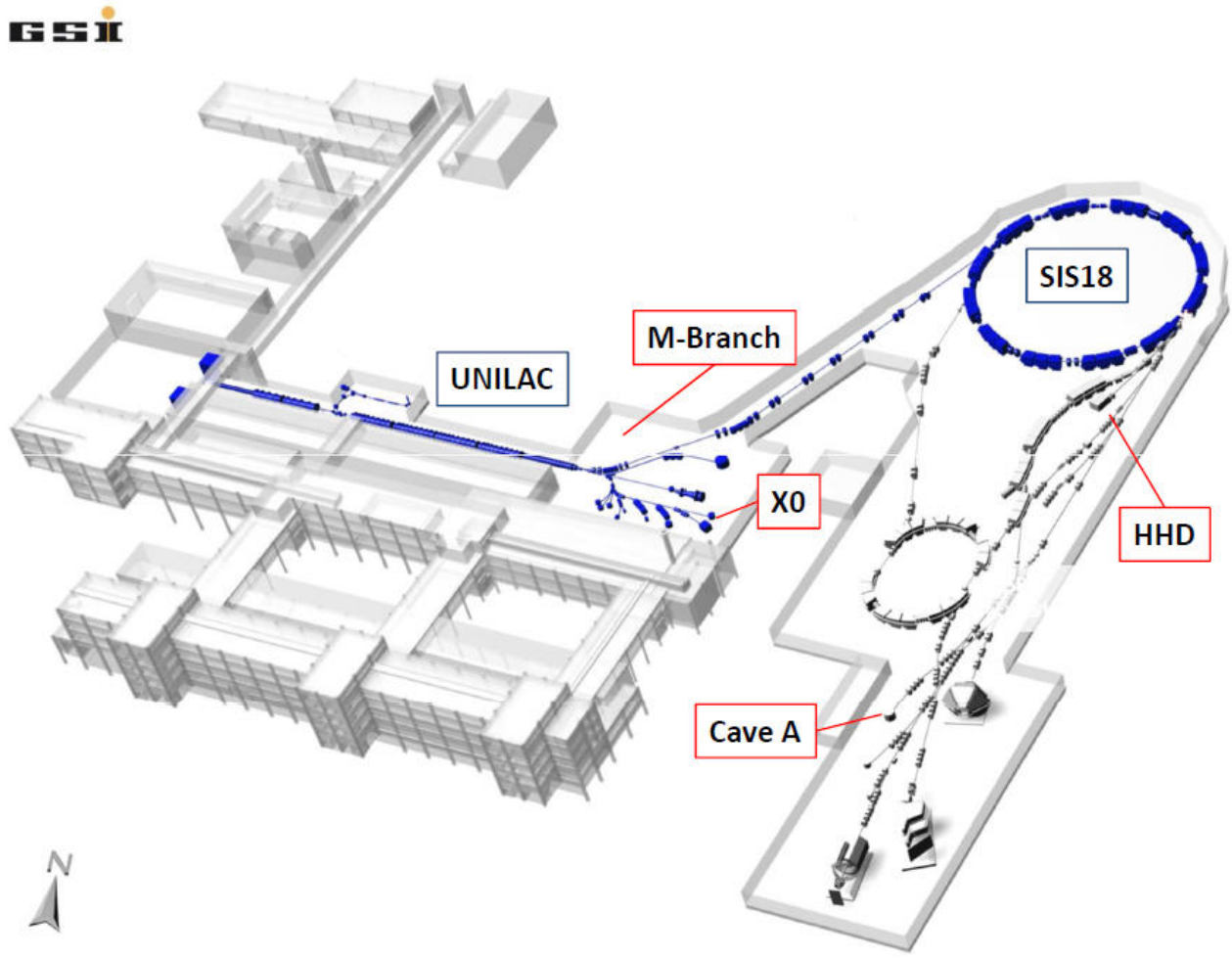

Fig. 4.5 GSI facility and the used irradiation sites (red)

Irradiation Facility X0

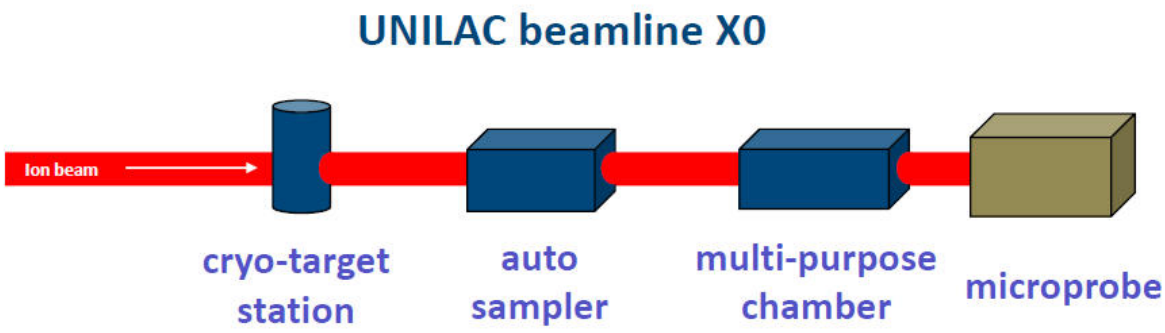

Fig. 4.6 Schematic view of the X0-beamline. The irradiation experiments were conducted at the auto sampler target station

X0 is located at the end of the UNILAC experimental hall. Beamline X0 houses a cryostat, an automated sample exchanger, a multipurpose irradiation chamber as well as the microprobe. Except the heat measurements of the "flux-test" all irradiations with medium energies (C-Au ions, ~11 MeV/u) were performed in the automated sample exchange system. The samples were mounted onto a 5×5 cm^2 aluminum holder which was transported by the automated sample exchange system into the vacuum chamber for the irradiation. All samples were irradiated at room temperature and perpendicular to the sample surface unless otherwise noted. By using quadrupole magnets, the ion beam was defocused so that the 5×5 cm^2 sample area was homogeneously irradiated. The used fluences ranged from 10^4 to several 10^{12} ions/cm^2. The ion flux was limited to be below 2×10^8 cm^{-2}s^{-1} in the case of heavy ion irradiations and below 1×10^{10} cm^{-2}s^{-1} in the case of carbon-ion irradiation. In both cases, the flux was limited in order to avoid macroscopic sample heating. The intensity of the used ion beam was controlled by measuring the electric current of a so-called Faraday cup. For a known charge state and beam spot size this signal can be converted into the absolute ion current. The measured beam current values were used to calibrate a secondary electron transmission monitor (SEETRAM) consisting of three thin metal foils of about 1 micron in thickness [159]. In contrast to the Faraday cup, the SEETRAM is not a beam stopping device, offering the possibility of online flux control. When passing through the SEETRAM, the ion beam loses some energy, thus the initial energy of 11.4 MeV/u is reduced to about 11.1 MeV/u.

In an dedicated experiment (designated as “dose rate test”) a typical aluminum-frame sample holder was mounted inside the multipurpose chamber equipped with polyimide samples for spectroscopic observations. The goal of the experiment was to determine the comparative heat increase between different ion fluxes. Therefore the chamber was equipped with a CaF_2-window allowing the heat to pass the chamber and to be recorded via a pyrometer (having an infrared detector). Details and results of this experiment are discussed in chapter 5.1. Fig. 4.7 shows the scheme of the experiment.

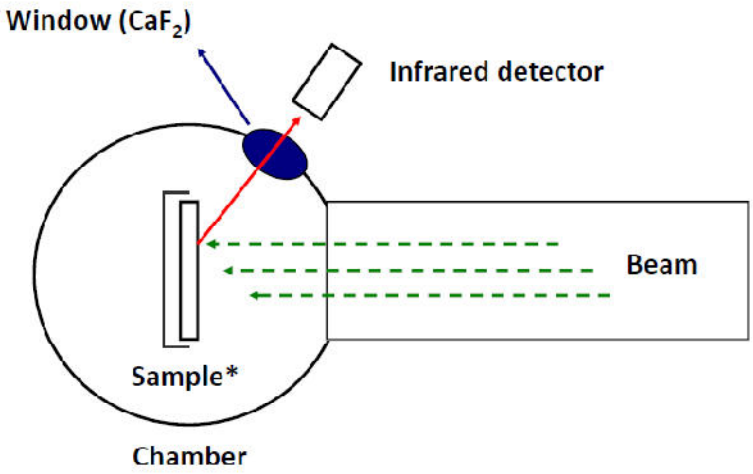

Fig. 4.7 Scheme of the “dose rate test” showing the irradiation chamber, which was equipped with an CaF_2-window allowing the temperature of the irradiated sample to be measured.

Table 4.4 Summary of X0 irradiation experiments with performed analysis.

Material / Ion / Energy	Max. dose (MGy)	Type of Test
Pixeo/C-ions/11MeV/u	2.2	Tensile-test
Polyimide/C-ions/11MeV/u	4.5	IR, UV/Vis, DS-Test
Polyimide/Ni-ions/11MeV/u	50	DS-Test, thermal conductivity, heat capacity
Polyimide/Ru-ions/11MeV/u	17	IR, UV/Vis, DS-Test
Polyimide/Ta-ions /11MeV/u	80	TG-MS, DS-Test
Polyimide/Au-ions /11MeV/u	10	IR, UV/Vis, DS-Test

Irradiation Facility M3

The M3-beamline at the M-branch is a new target station installed at the UNILAC at GSI in 2008. The M-Branch provides ion beams up to a maximum energy of 11.4 MeV/u for materials research. The facility with state-of-the-art in-situ instrumentation and analytical tools was financed by combined funds from partially transferred research budget of "Ionenstrahllabor" (ISL) and from the GSI, the Helmholtz Association (Impuls- und Vernetzungsfond), and a BMBF project of several German universities (Verbundprojekt: "Hochauflösende in-situ Charakterisierung struktureller Veränderungen in Festkörpern induziert durch hochenergetische Schwerionenstrahlung", Project No. 05KK7RD1) [160],[161],[162].

The set-up of target station M3 is shown in Fig. 4.8. The ions first pass an aperture consisting of a variable pair of x-y-slits for ion beam shaping. Afterwards, a SEETRAM, a Faraday cup, and a luminescence screen with a CCD camera for beam diagnostic are available. Beamflux monitoring can be performed by the SEETRAM and current measurements on the x-y-slits. After the beam diagnostic unit a high temperature chamber allows heating experiments up to 1100 K. The multipurpose diagnostic chamber (Fig. 4.9) placed at the end of M3 contains a sample holder arrangement connected to the cooling finger of a closed cycle refrigerator. Temperatures down to 10 K can be reached.

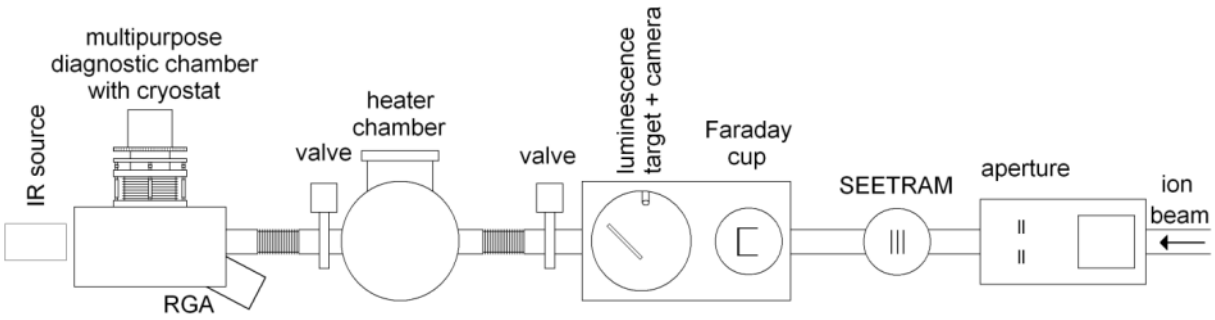

Fig. 4.8 Schematics of target station M3: Ions have to pass the aperture for ion beam shaping, a beam diagnostic unit providing a SEETRAM, a Faraday cup, a luminescence screen, and a heater chamber to reach the multipurpose diagnostic chamber. Reprinted with permission of [162].

The nearly free-standing sample holder unit can be moved 90 mm up and down and can be rotated around +/- 180°. For in-situ investigations of ion beam induced effects on condensed matter the chamber can be coupled with a FT-IR spectroscopy system and a RGA system.
For FT-IR spectroscopy a NICOLET 6700 FT-IR spectrometer of ThermoFisher Scientific is used. The spectrometer was placed outside the analysis chamber -45° with respect to the ion

beam normal (Fig. 4.10). The IR detection unit was separated from the casing of the spectrometer and installed outside the chamber at +135° with respect to the ion beam (Fig. 4.10). The infrared transparency is ensured by using two flanges including 4 mm thick ZnSe windows. In front of the first IR window a KRS-5 IR polarizer can be mounted.

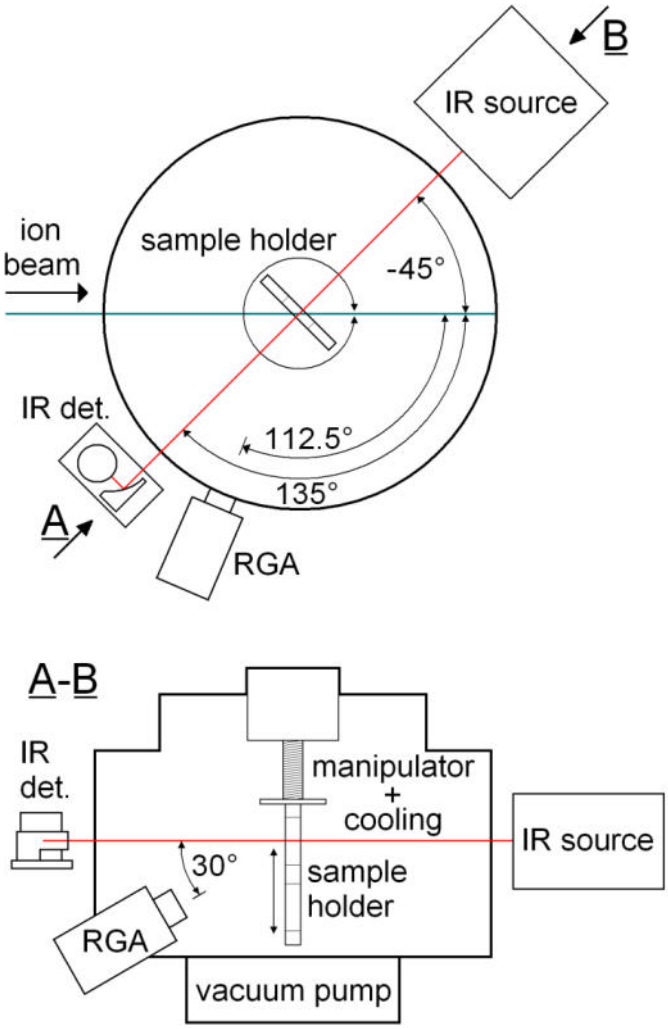

Fig. 4.9 Schematics of the multipurpose chamber at target station M3. IR source and detection unit are placed outside of the chamber. The angle between IR radiation and ion beam normal is -45°. The RGA is mounted near the IR detection unit and tilted down 30°. The sample holder can be moved up and down and is rotatable. Reprinted with permission of [162].

Even though the infrared beam has to pass through the KRS-5 IR polarizer, two ZnSe windows, the sample, and some air between the gaps of the IR source and the IR detector, IR spectra with very good signal intensity are obtained for polymer samples with sufficient thickness (1-25 μm).

For residual gas analysis a Microvision Plus quadrupole mass spectrometer (QMS) of MKS Instruments provides a mass range from 1 to 200 amu and a detection range from 6.7×10^{-10} to 6.5×10^{-2} Pa. The RGA is located 112.5° compared to the ion beam and tilted

30° downwards. If not otherwise mentioned electron impact (EI) was used at an accelerating voltage of 70 eV.

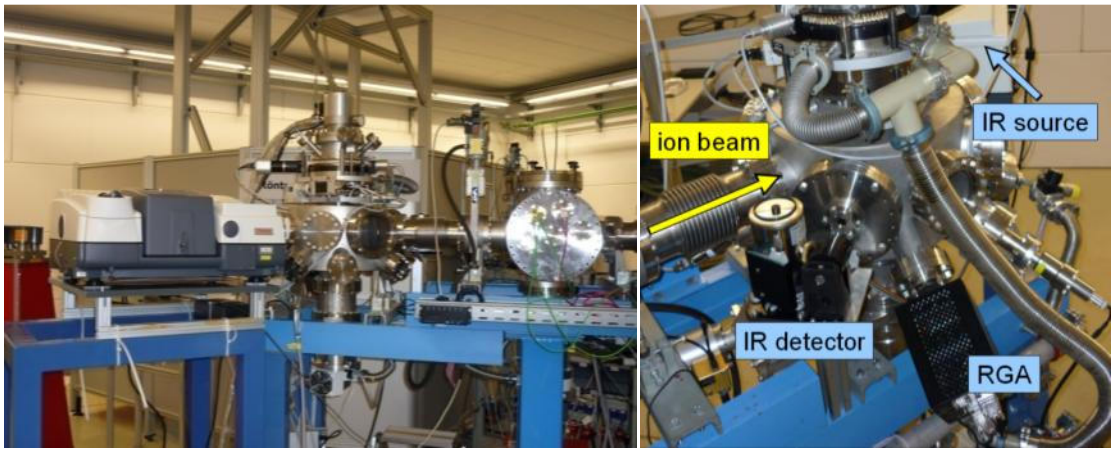

Fig. 4.10 Photographs of the target station at beamline M3 showing the IR spectrometer (left) and the IR detector and RGA (right)

In this thesis the first experiments at the M3-beamline are presented after successful commissioning in 2007. Polyimide and cured polyepoxy films were irradiated with 4.5 MeV/u Au ions as presented in chapter 5.1.

Table 4.5 List of in-situ measurement experiments at the M3 beamline

Material (MeV/u)	Max. fluence (cm^{-1}) / dose (MGy)	Type of Test
Polyimide (Kapton HN)	1×10^{12} / 10	In-situ IR/MS
Amine cured polyepoxy	1×10^{12} / 8	In-situ IR/MS

Irradiation Facility Cave A at SIS18

Cave A, equipped with several beam diagnostics such as a calibrated SEETRAM and an ionization chamber, was used for irradiation experiments of epoxy/fiber composites. Epoxy fiber composites typically have a thickness of >1 mm. To irradiate this material homogeneously the penetration depths of ions accelerated at the UNILAC are not high enough. All irradiations took place in air after the beam passed a 100 μm thick aluminum window and 45 cm of air.

Table 4.6 List of samples irradiated at Cave A and performed analysis

Material / Ion / Energy	Max. fluence (cm^{-1}) / dose (MGy)	Type of Test
G11 / Xenon/ 200 MeV/u	2×10^{10} / 0.038	DS-Test (DC)
G11 / Xenon/ 200 MeV/u	1×10^{11} / 0.19	DS-Test (DC)
G11 / Xenon/ 200 MeV/u	2×10^{11}/ 0.38	DS-Test (DC)
G11 / Xenon/ 200 MeV/u	1.2×10^{12} / 2.3	DS-Test (DC), C_p-Low-T
G11 / Au/ 400 MeV/u	1×10^{10} / 0.02	DS-Test (AC)
G11 / Au/ 400 MeV/u	1×10^{11} / 0.2	DS-Test (AC)
G11 / Au/ 400 MeV/u	1×10^{12}/ 2	DS-Test (AC)
Cy/Ep-Comp. / Au/ 400 MeV/u	1×10^{10} / 0.02	DS-Test (AC)
Cy/Ep-Comp. / Au/ 400 MeV/u	1×10^{11} / 0.2	DS-Test (AC)
Cy/Ep-Comp. / Au/ 400 MeV/u	1×10^{12}/ 2	DS-Test (AC)

Irradiation Facility: HHD Beam Dump

The HHD beam dump, located at the exit of the SIS18 synchrotron, is a stainless steel beam dump surrounded by concrete walls. It is installed as a security cave, where the beam can be dumped whenever no experimental cave is using it, or for accelerator experiments where the experiments are not performed in a cave.

Within this study this facility was used for direct irradiation on a SIS 100 magnet voltage breaker using a high intensity Ar beam, as well as for the production of secondary particle fields via the fragmentation of an intense 1 GeV/u Uranium beam inside a stainless steel target. For these purposes various modifications to the existing beam dump beam line were performed. As can be seen in Fig. 4.11, the beam tube, which was directly connected to the beam dump, was partly removed and equipped with a stainless steel vacuum window. For remote controlled sample positioning, two moving axes and several analog and digital cameras were installed. Several scintillator-based ion beam profiler were installed for beam adjustments. The beam flux was measured via a calibrated beam transformer and the position of the beam was measured with profile grids.

Fig. 4.11 Installations of the irradiation set-up at the HHD beam dump of SIS 18. Upper pictures show the beam dump before installation. Bottom pictures show the dump after removing of the beam tube and the installations of moving axis, light targets, and the sample holder, which can be moved into the beam dump.

Table 4.7 Fluence, dose and used ion beam of the voltage breaker irradiation experiment

sample / ion / energy (MeV/u)	max. fluence (cm^{-1}) / dose (kGy)	type of test
Voltage breaker / Ar / 400	3×10^{13} / 630	leakage test

Irradiation experiment with secondary radiation

As mentioned at beginning of this chapter the HHD beam dump was used to perform an experiment with a secondary radiation beam, which was produced via stopping of a 1 GeV/u uranium beam inside a stainless steel target (angle of incidence: 2.4°). The irradiation set up (Fig. 4.12) consisted of a V-shaped stainless steel target with various samples for mechanical, electrical and performance testing. Since part of the samples get radioactive and have to "cool down" until 2015 they will be part of a different thesis. Table 4.8 summarizes the samples which were measured within this thesis. For a more detailed description of the experiment as well as for the dose calculations see [163],[164], [165], [166].

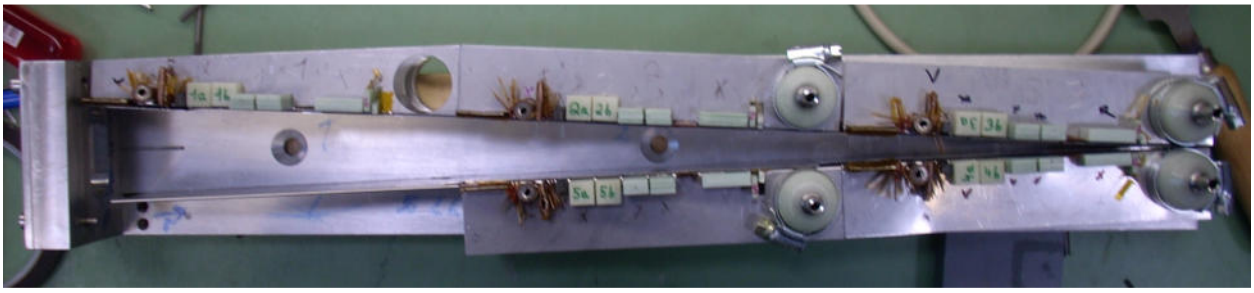

Fig. 4.12 V-shaped stainless steel target-holder filled with samples from the top

Table 4.8 List of samples, measurements and calculated dose of the secondary radiation experiment at HHD

Sample	Dose (MGy)	Type of Test
Pixeo glued polyimide	3.5	Tensile Test
Pixeo glued polyimide	4.2	Tensile Test
Pixeo glued Polyimide	5.6	Tensile Test
Cernox T-sensor	0.1	Performance Test
Cernox T-sensor	2.7	Performance Test
Cernox T-sensor	3.2	Performance Test
Cernox T-sensor	5.2	Performance Test
Cernox T-sensor	6.1	Performance Test

5 Results & Discussion

5.1 Polyimide

"Dose Rate Test": Exclusion of Temperature and Dose Rate Effects

Quite a number of studies show that environmental conditions such as pressure [167], atmosphere [168]), temperature [46],[169],[170],[171], and the dose rate [172],[173],[174] influence the induced changes of ion irradiated materials. To avoid misinterpretation of data due to the existence of an unknown high temperature (ion induced macroscopic heating) or dose rate effect, we measured the temperature rise as well as the ion induced coloration of polyimide foils in a dedicated experiment (the set up is described in chapter 4.4). Different fluxes were used while holding the pulse length and frequency constant (Table 5.1). This way the dose rate was changed by more than one order of magnitude. Earlier experiments of dose rate effects used gamma rays and low energy (keV regime) ion irradiation [172],[173],[174]. These radiation sources usually do not have a pulsed structure like the linear UNILAC at GSI. At present little is known about the influence of repetition rate nor pulse length of high energy heavy ion irradiation on the induced changes in matter. A complete study with a large parameter set was not possible due to the limited beamtime.

Table 5.1 Irradiation beam parameters of the "doserate-test" performed at X0 beamline. 11.1 MeV/u Xe-Ions.

	Exp.1	Exp.2	Exp.3	Exp.4
Flux ($cm^{-2}s^{-1}$)	4×10^{7}	1.2×10^{8}	3.5×10^{8}	6×10^{8}
pulse frequency (Hz)	5	5	5	5
pulse length (ms)	4.5	4.5	4.5	4.5
max. Fluence ($ions/cm^{2}$)	2×10^{11}	2×10^{11}	2×10^{11}	2×10^{11}
temp. at max. fluence (°C)	RT	RT	42	58

In each irradiation experiment three different fluences were applied (A: 1×10^{10}, B: 1×10^{11} and C: 2×10^{11} ions/cm^2). During beam exposure the temperature was recorded online with a pyrometer (chapter 4.3). Fig. 5.1 shows the temperature rise during (i) the maximum fluence of Exp. 2-4 and (ii) all irradiation steps during Exp. 4. It can be seen, that starting from Exp. 2 a temperature increase of the sample becomes significant. At the maximum flux/fluence the sample temperature is in the order of 60°C.

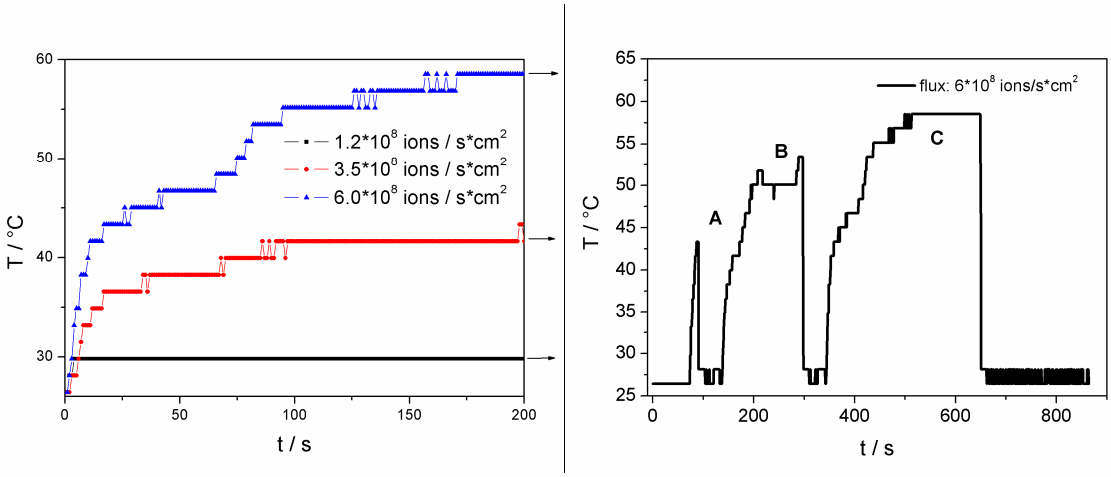

Fig. 5.1 Temperature increase of the polyimide samples during irradiation using different fluxes of the highest fluence (left) and of the three different fluences of the highest flux used (right).

The ion induced coloration of the samples was measured by means of UV/Vis spectroscopy. Fig. 5.2 shows a plot of the cut off wavelength (measured at 5 % transmittance, see page 69) of all irradiated samples against the ion fluence for all four experiments. It can be stated that in the observed flux and temperature regime no significant influence on the coloration of polyimide is found. The reason for this can be explained by the high thermal resistance, the absence of phase transitions in the observed temperature regime as well as the high glass point (T_G=360-410°C) of polyimide. Nevertheless in further heavy ion irradiation campaigns the flux was limited to 2×10^8 ions/cm^2, to avoid heating of the samples.

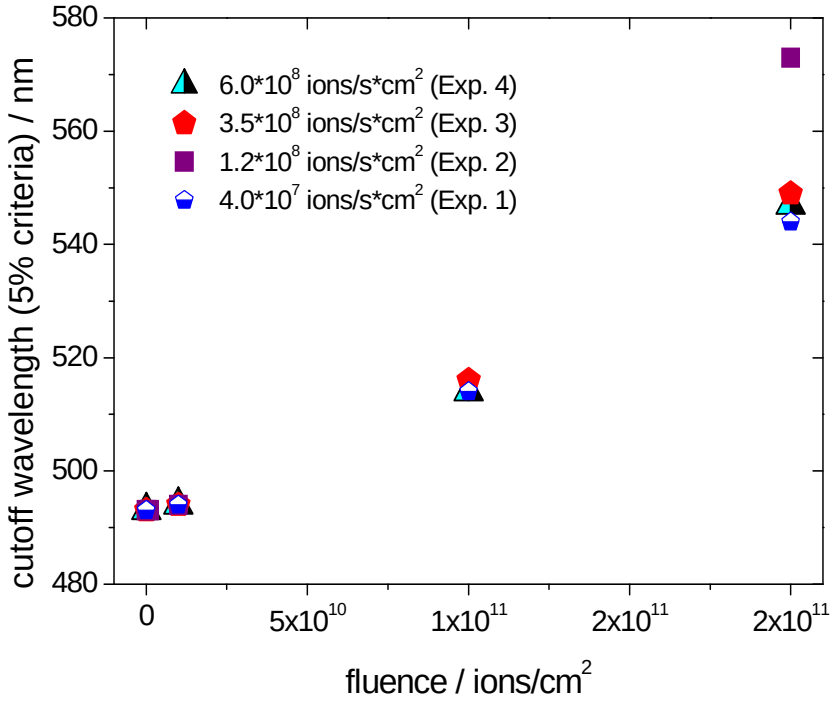

Fig. 5.2 Cutoff wavelengths 12-μm polyimide irradiated according to Table 5.1.

Color change in polyimide induced by 21 MeV proton irradiation (UV/Vis)

Classical polyimides like Kapton (PMDA-ODA) have an amber to orange color deriving from intra- and intermolecular charge transfer complexes between the electron rich (amine-phenyl fragment) and the electron accepting (diimide fragment) structural units [51], [175], [176] [177].

Ionizing radiation such as UV, gamma and neutron radiation is known to induce a blue shift of the absorption edge in UV/Vis spectra of polyimide [176], [178] (see as example Fig. 5.3 measured in this work) while for ion irradiations in all cases a red shift is observed and the magnitude of shift depends on the stopping power of the used particle beam [120], [122], [179]–[181].

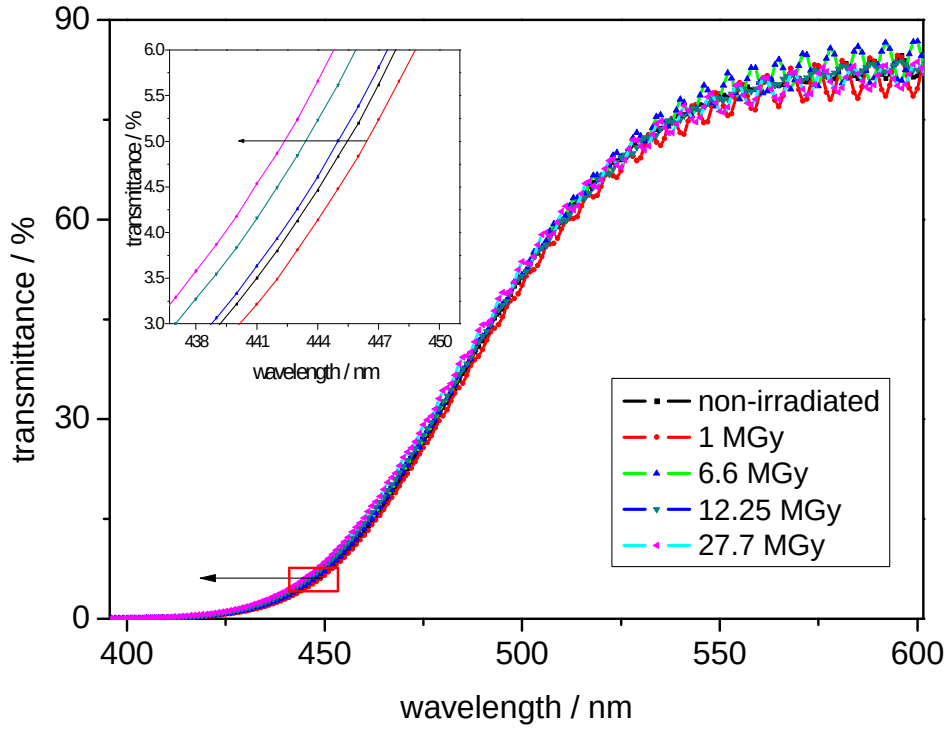

Fig. 5.3 UV/Vis spectra of gamma-irradiated 12-μm polyimide. The Arrow in the magnified inset indicates the shift at 5% of transmittance (absorption edge).

The particle beams used in literature range from protons, light and heavy particles of very low energy (<1 MeV/u) up to high energy irradiations of ions from carbon to uranium. Since no data concerning changes of the optical absorption is found for high energy proton

irradiation this part of the irradiated 12 μm polyimide foils was measured by UV/Vis spectroscopy to complete the mosaic of different radiation types.

Fig. 5.4 shows the UV/Vis spectra of 12 μm polyimide foils irradiated with 21 MeV protons. While in the case of 800 MeV proton irradiation as well as the irradiation experiment with neutrons no significant changes in the UV/Vis spectrum were observed, the irradiation with 21 MeV protons (Fig. 5.4) resulted in a small red shift similar to other particle beams. The electronic energy loss of 21 MeV protons in polyimide is one order of magnitude than for 800 MeV protons.

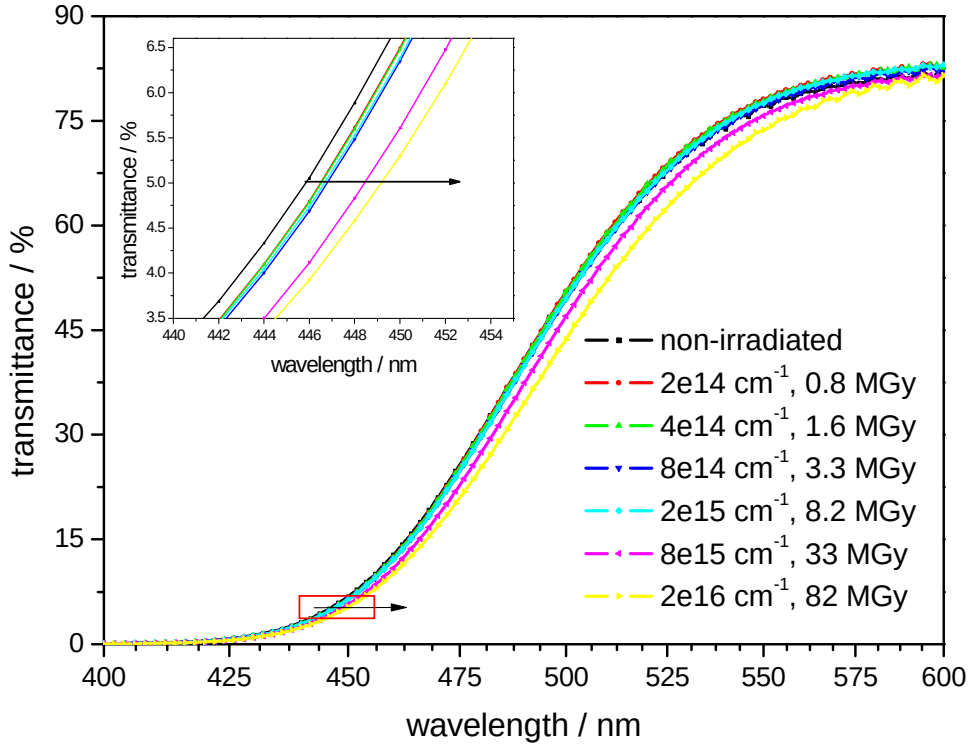

Fig. 5.4 UV/Vis spectra of 12-μm polyimide irradiated with 21 MeV protons. Arrow in the magnified inset indicates the shift at 5% of transmittance (absorption edge).

Interpretation of the changes of optical absorption in irradiated Kapton

The blue shift induced by UV/gamma/neutron radiation is explained by chain scission leading to a destruction of the donor-acceptor charge transfer complexes while the red shift of ion induced degradation is ascribed to the formation of unsaturated conjugated bonds and the production of carbon clusters which start to overlap at high fluences to form amorphous

carbon (note that for low energy ion bombardment additional graphite like islands were observed [179], [180]). The latter pathway of ion induced degradation shares a similarity to thermal degradation of Kapton-type polyimide which forms amorphous carbon at temperatures above 600°C that crystallizes at higher temperatures to graphite [182]. The similarity between ion induced degradation and thermal degradation seems (at least in case of Kapton-type polymer) to provide supportive arguments for the thermal spike model (as described in chapter 2.2 .A temperature spike around the projectile path seems to be a reasonable model to interpret ion induced changes in polyimide. However, the model predicts a temperature spike with thousands of degrees Celsius were graphitic structures should form, but never were observed. An additional argument against this analogy is the carbon structure synthesis in polyimide samples, irradiated with high energy light ions, which are found to produce carbon structures in a two-hit process (anticipated by the increase in electrical conductivity [59]). This means that at the very beginning of the irradiation a kind of precursor forms which only changes to carbonaceous structures when a ion hits the same location. This speaks against a thermal spike since in both hits the induced temperature is similar and should not lead to carbon cluster synthesis in a thermal decomposition type of mechanism.

We therefore consider that the ion induced degradation follows a different mechanism. It should be noted that this interpretation can only be used for Kapton-type polyimides. Different polymers may decompose following individual degradation mechanisms. For example gamma induced degradation of fluorine containing polyimides can lead to a red shift in absorption spectra [183] in contrast to the observed blue shift found for polyimide.

Ion induced changes in chemical structure of polyimide (IR/RGA)

For decades, infrared spectroscopy has been widely used as one of the standard characterization methods for studying ion induced changes in polymers. For polyimide, it is found, that high energy heavy ion radiation induces special features not found in case of gamma, UV or thermal degradation: The formation of terminal alkynes, the synthesis of carbon clusters, and other oxidative degradation products. In this chapter the results of high energy proton and neutron irradiated samples are presented as well as first in-situ FT-IR and MS studies carried out at the M3-Branch of GSI´s UNILAC. For protons and neutrons, no data of FT-IR is found in literature while the latter case presents in-situ measurements which allow exclusion of any post-degradation effects or errors deriving from inhomogeneities of the sample. Results are discussed and compared with the existing data from the literature.

IR spectra of proton and neutron irradiated samples

In the case of 800 MeV proton and neutron irradiation no difference in IR-spectra between the irradiated and non-irradiated samples is detected. This means that for the irradiation dose up to 3 MGy, no significant degradation products are found, but may appear at greater dose. Samples irradiated with a great dose of energetic ions became highly radioactive and had to cool down for about 2 years before the analysis. Application of greater doses was therefore unreasonable.

One of the IR spectra of the 21-MeV proton irradiated polyimide samples is displayed in Fig. 5.5. Additionally to the decrease in all absorption band intensities found for non-irradiated polyimide (which typically appears when polymers are degraded by ionizing radiation) an increase of a broad band in the regime 3750 cm^{-1}-3000 cm^{-1} appears. This band is identified as hydroxyl vibration of alcohols and/or carboxylic acids and is not present in the case of heavy ion irradiation experiments in vacuum. It should be noted that in contrast to the results derived by measurements on swift heavy ion irradiated samples at the UNILAC the proton irradiations took place in atmosphere with the sample being exposed to humidity and oxygen. A growth of hydroxyl vibration bands indicates oxidative degradation products coming from reactions of the polymer with oxygen or humidity and has also been observed in irradiation experiments of polyimide with heavy ions in oxygen atmosphere [184].

Comparing the efficiency of ion induced changes between light and heavy ion particles shows that heavy ions, which have an electronic energy loss orders of magnitude higher than the used proton beam, induce extensively more damage.

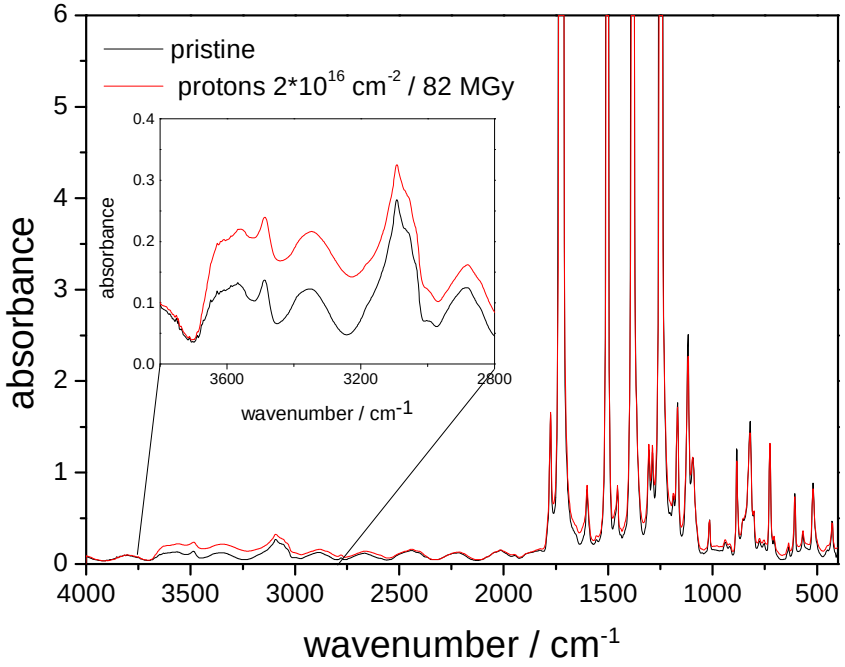

Fig. 5.5 FT-IR spectra of non-irradiated and 21 MeV proton irradiated 12-μm polyimide. For a better visibility only the spectra of non-irradiated polyimide and the greatest dose are presented. The inset shows a zoom in the wavenumber range of 3750 cm^{-1}-2800 cm^{-1}.

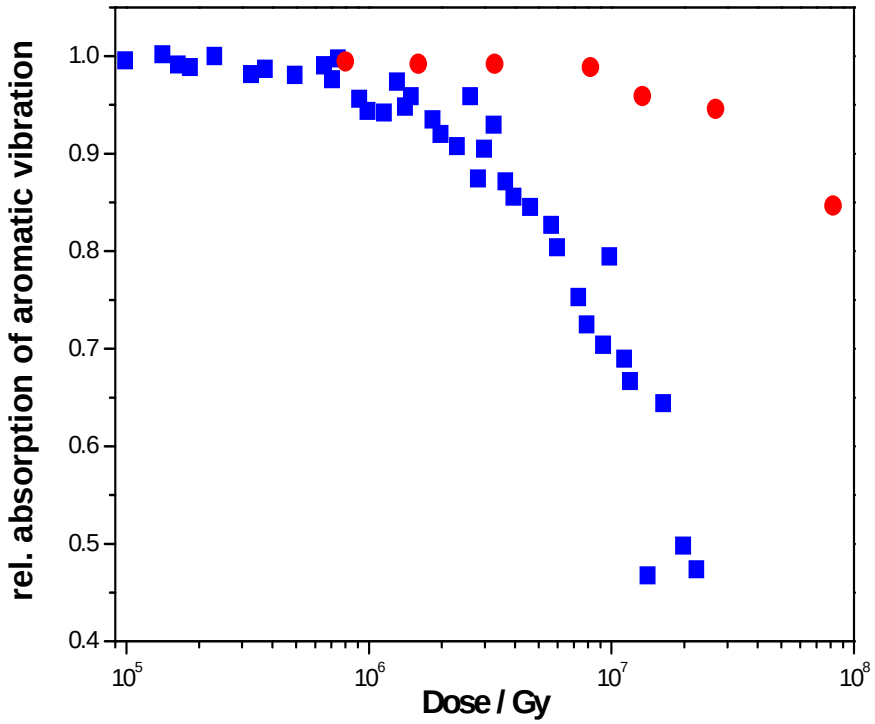

Fig. 5.6 Comparison of the relative absorption of the aromatic vibration band at 726 cm^{-1} of proton (red dots) and heavy ion irradiated polyimide (blue squares, adopted from [58]).

Plotting of the relative changes against the dose (in Fig. 5.6 for example the relative decrease of the vibrational band intensity at 726 cm^{-1} of proton irradiated samples is plotted together with the data measured by Severin et. al. [58], [120]) shows the efficiency of heavy ions producing structural degradation that is by a factor of ten higher.

In situ infrared spectroscopy of polyimide irradiated with 4.5 MeV/u Au ions:

Fig. 5.7 shows the infrared spectra of 12-μm polyimide recorded before and after the irradiation with 4.5 MeV/u Au ions of the maximum fluence (1×10^{12} ions/cm^2). In the spectra the typical ion induced degradation of polyimide becomes visible: nearly all IR bands decrease due to the degradation of the molecular structure of the polymer. New absorption bands appear which are due to the ion induced production of unsaturated hydrocarbons, nitriles, isocyanides and alkynes, as well as oxidative degradation products such as carboxylic acids and alcohols [184] [185]. Fig. 5.8 shows the IR spectra of the sample irradiated with different fluences in the wave number range from 3000 cm^{-1} to 2700 cm^{-1}. In this region the rise of 4 new peaks is observed. These new bands are identified as saturated carbon-hydrogen bonds and/or carboxylic acids. So far only one of these peaks was mentioned in literature, presumably due to their low intensities [184]. The in-situ measurement provides a good technique to investigate such small changes in the IR spectrum, due to its high signal to noise ratio obtained by the significant suppression of background effects.
Semi-quantitative exploration of the relative changes of band areas of degrading bands is shown in Fig. 5.9. Due to overlapping bands no clear trend can be found and all bands, although belonging partly to the same functional groups of the polymer, show slightly different degradation behaviour. As mentioned in other studies the polyimide group frequencies seem to degrade faster but the spectra show strong scattering which makes a true statement difficult. However, it can be stated that the degradation in principle follows an exponential decay typically observed for single impact processes i.e. a certain change is already induced in the material at the first impact of an ion. These results are discussed and interpreted in greater detail together with the complimentary mass spectroscopic observations.

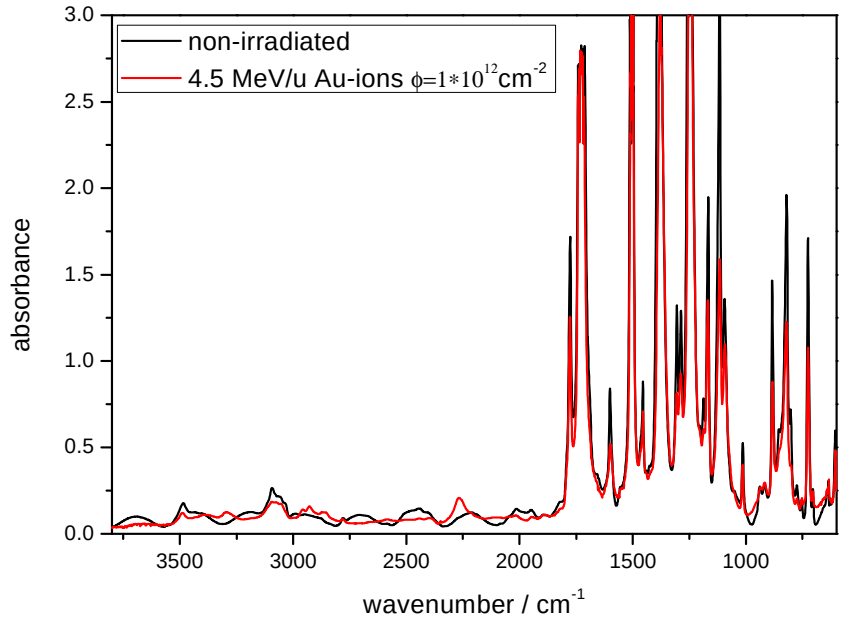

Fig. 5.7 IR spectra of non-irradiated and Au-ion irradiated ($\phi=1\times10^{12}$ cm^{-2}) polyimide. Reprinted with permission of [162].

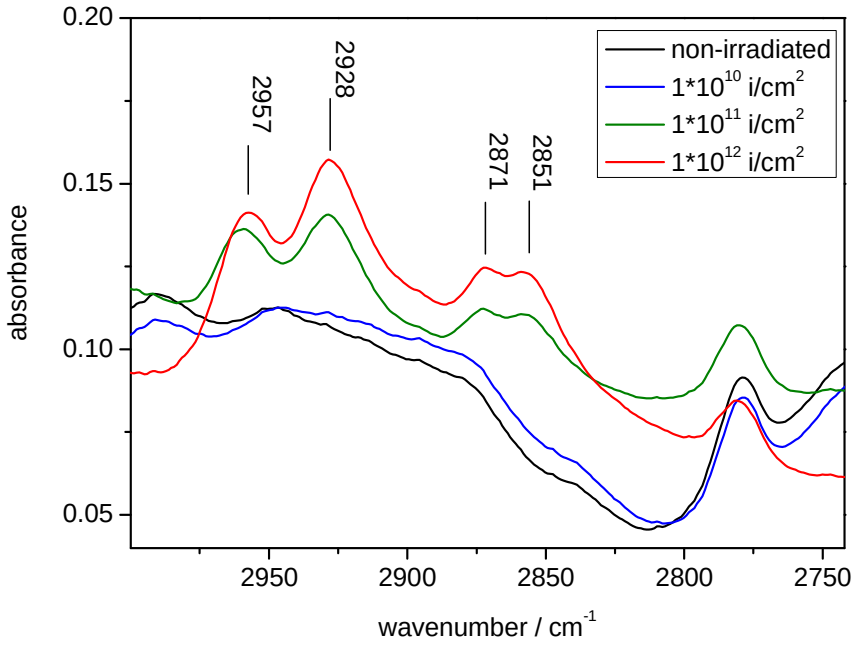

Fig. 5.8 IR spectra of Au-ion irradiated polyimide in the regime 3000-2700 cm^{-1}

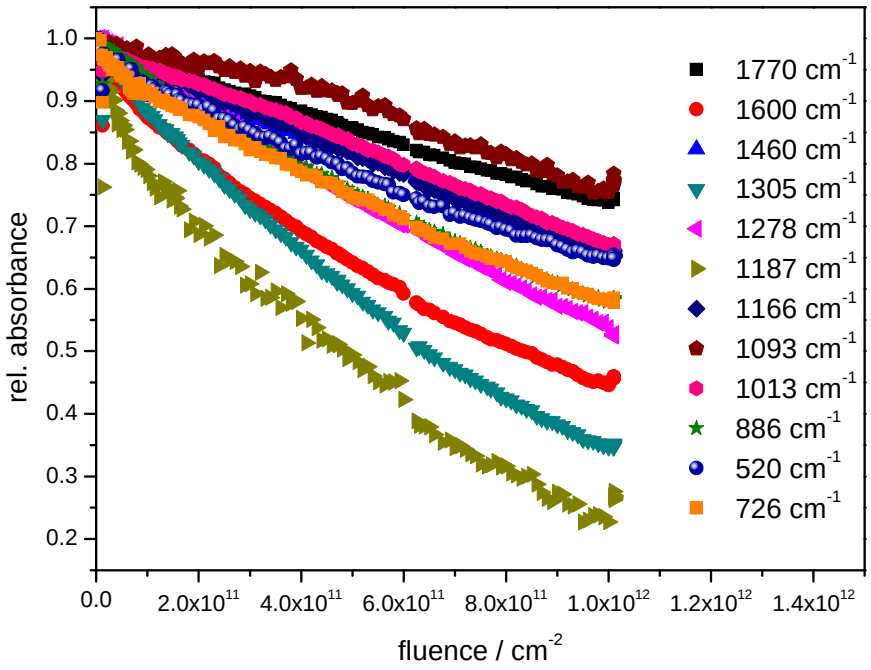

Fig. 5.9 Relative absorbance of several absorption bands of Au-ion irradiated polyimide recorded in-situ during beam breaks.

In-situ residual gas analysis:

Fig. 5.10 shows the residual gas spectra of polyimide measured in combination with in-situ IR spectrometry described above. The diagrams indicate the background spectrum, the sample spectrum during irradiation, and their differential spectrum. Without ion beam exposure, surface contaminations and background gases such as H_2O (m/z=18), CO (m/z=28), and CO_2 (m/z=44), and some signals from fragmented hydrocarbons (m/z=25-27) are detected. They derive from gas leakage and desorption from the surface of the chamber and the sample. With the start of ion irradiation these signals increase and additional signals become visible. The most pronounced difference in peak intensity is found for m/z=28, 2, 26 and 12 in decreasing order. Obviously, a mixture consisting of CO, N_2 C_2H_2, HCN, C and H_2 molecules are the main degradation products which leave the polymer during the irradiation, as described in the literature for ion induced [184], thermally induced [186], and laser induced degradation [187], [188]. Fig. 5.11 shows the ion monitoring traces for carbon (m/z=12), C_2H_2 (m/z=26), and C_2H_4/CO/N_2 (m/z=28). Before the irradiation starts, the partial pressure of all three molecules shows a relatively low value. Starting the irradiation leads to a higher partial pressure for the chosen molecules caused by the

degradation of the sample. At the onset of the irradiation all measured m/z values quickly reach a plateau which represents a stationary state in the emission rate and the pumping efficiency of the turbo molecular pump.

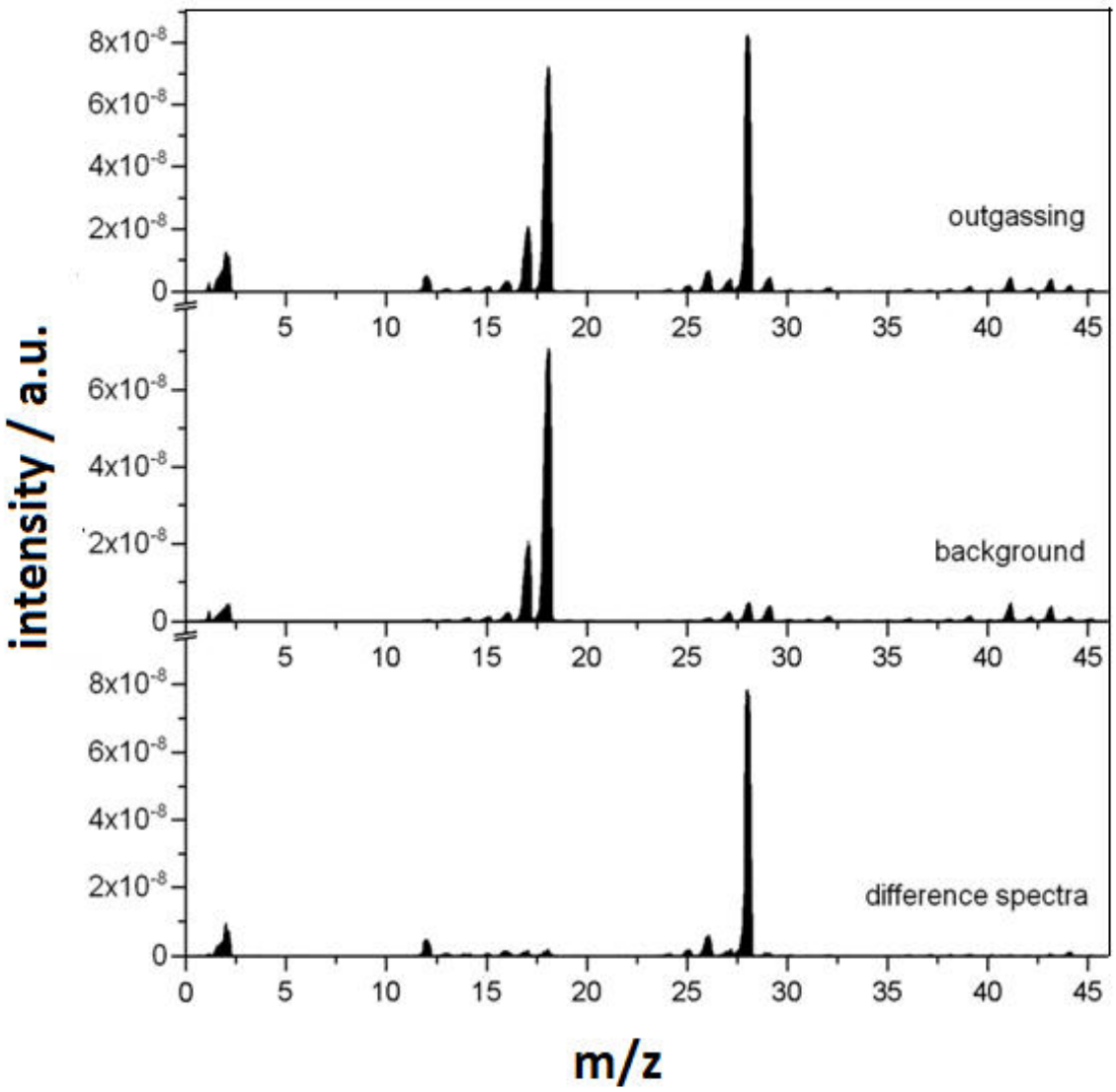

Fig. 5.10 Outgassing products of 12-μm polyimide before and during irradiation as well as the difference of both. The spectra show that the most pronounced peak is found at $m/z = 28$ which is a mixture consisting of C_2H_4, CO, and N_2 molecules.

This behavior is different from other outgassing studies for example using low energy ion irradiation experiments (in the keV range), they show a maximum emission rate after the start of the irradiation, followed by a decrease in emission rate with ongoing fluence [147].

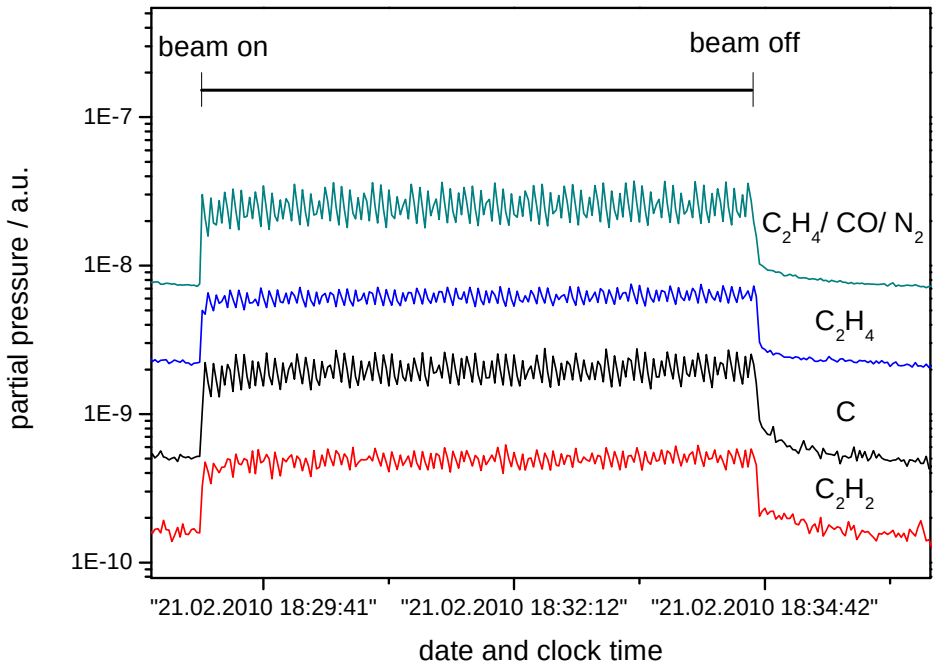

Fig. 5.11 Example of online gas monitoring during irradiation. Before irradiation the partial pressure of all molecules is at a relatively low value. Starting irradiation leads to a rise of partial pressure of the molecules due to the degradation of the sample. After stopping the irradiation the partial pressure returned to the value of the residual gas of the vacuum system.

After the irradiation the partial pressure re-established to the value of the residual gas of the vacuum system [189].

Thermal gravimetric (TG) analysis of ion irradiated polyimide

Fig. 5.12 shows the TG curves and their derivatives of 21 MeV proton irradiated samples in the temperature range up to 800°C. Mishra et al. found for low dose proton irradiations (<100 kGy,) [190], [191] and electron irradiation of polyimide [192] an improvement in thermal stability after irradiation with 60 MeV protons (explained by cross-linking of the material), and a small decrease in thermal stability for 2 MeV electron irradiation of 23 kGy (explained by chain scissions). The great dose 21 MeV proton irradiation used in this study (800 kGy to 82 MGy) shows a reduction of the thermal stability visible in decreased onset temperature of thermal degradation ($T_{d,5\%}$) and the temperature at maximum decomposition rate ($T_{d,max}$, Table 5.2).

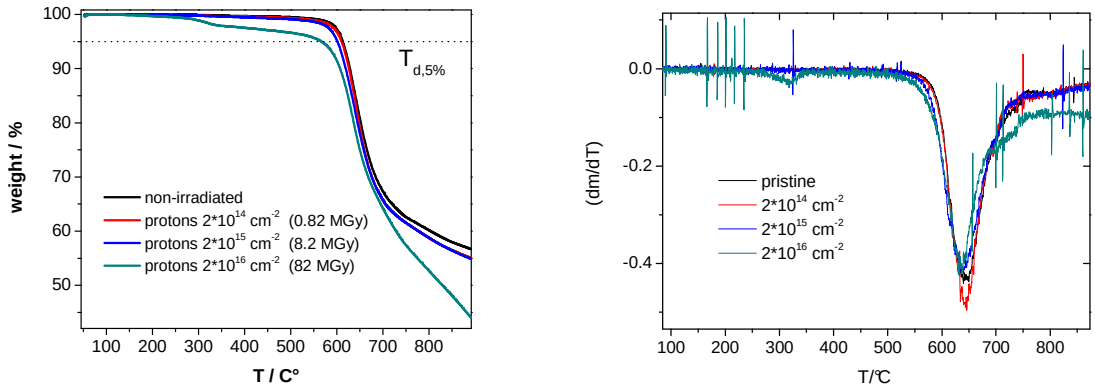

Fig. 5.12 TG analysis of 50 μm polyimide irradiated with 21 MeV-protons (left) and their derivatives (right)

Table 5.2 Results of TGA measurements of 21 MeV proton irradiated polyimide

Fluence /p^+/cm^2	Dose/MGy	$T_{d,(5\%)}$ / °C	$T_{d,max}$ / °C	Char residue / %
Pristine	0	613	645	57
2×10^{14}	0.8	610	642	55
2×10^{15}	8	601	638	54
2×10^{16}	82	566	634	43

The ion irradiation clearly modifies the course of the radiolysis process resulting in reduced degradation temperatures and significant changes of residual weight values due to char residues. Beam-induced effects of heavy ion irradiations are found to be more pronounced as shown in Fig. 5.13. Ta-ion irradiated samples show a strong reduction in thermal stability (Table 5.3) and degrade the material an order of magnitude faster than protons (Fig. 5.14).
It should be noted that the temperature of maximum rate of decomposition ($T_{d,max}$) is less effected compared to the temperature of initial decomposition ($T_{d,\ 5\%}$). In case of Ta-ions first

a decrease of $T_{d,max}$ is observed which increases again at higher fluence. This trend may due to the increasing char residue forming at higher fluences.

Table 5.3 Results of TGA measurements of 11 MeV/u Ta-ion irradiated polyimide

Fluence /ions/cm^2	Dose/MGy	$T_{d,(5\%)}$ / °C	$T_{d,max}$ / °C	Char residue / %
Pristine	0	613	645	57
1×10^{11}	0.8	553	581	60
1×10^{12}	8	399	575	57
5×10^{12}	40	430	614	71

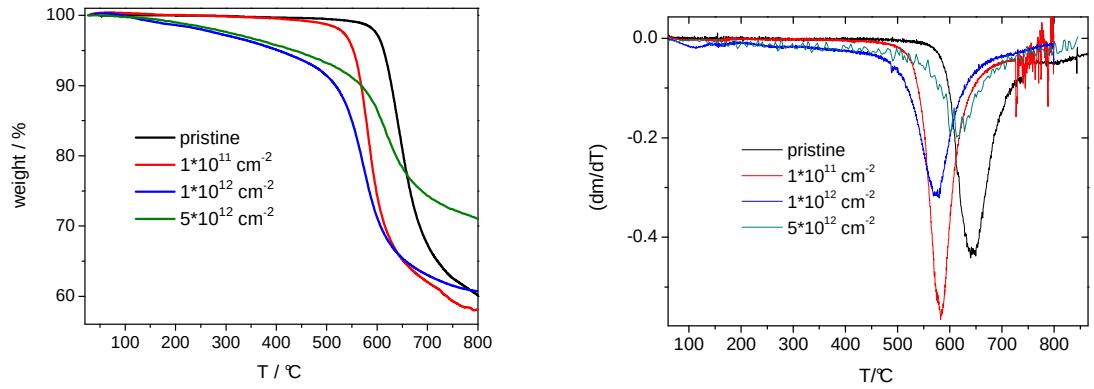

Fig. 5.13 TG analysis of polyimide samples irradiated with 11 MeV/u Ta-ions (left) and their derivatives (right)

The change in char residue follows a different trend for proton and heavy ion irradiated samples. Char residue at 800°C of proton irradiated samples decreases from 57 to 43 % while for Ta-ions the residual weight increases from 57 to ~70 % (at the maximum fluence). The tendency to form a char residue is strongly determined by the chemical structure of a given polymer [193]. A char easily forms in case of dehydrogenated, substituted, or condensed aromatic rings, while a negative char-forming tendency is observed for aliphatic groups connected to aromatic groups. Under proton or low-fluence Ta-ion irradiation, the pristine structure of Kapton is obviously changed in a way that char does not form easily, probably by scission of aromatic rings leading to aliphatic structures. Especially in the case of proton irradiation, which took place in air, a formed char might vanish due to its radiation induced reaction with O_2 leading to CO_2 outgassing from the material during the irradiation experiment (it should be noted that carbon materials are easily degraded thermally in oxygen atmosphere at already moderate temperatures [194]).

High-fluence ion irradiation in vacuum is known to create carbon clusters which do not degrade thermally within the temperature regime tested in inert gas atmosphere. Therefore

samples irradiated with heavy ions at high fluences already contain an ion induced char residue prior to the TG analysis. This would explain the increased char residue found for the heavy ion irradiation. Moreover, carbon particles suspended in polymers are known to catalyse thermal degradation and support the char-forming process [195].

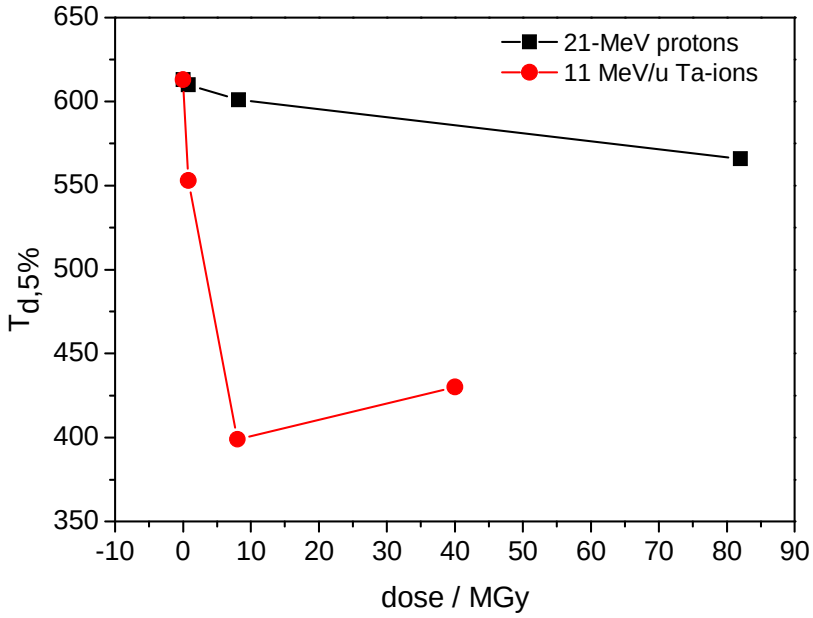

Fig. 5.14 Temperature of initial decomposition values plotted against the dose. The lines are guides to the eye only.

However, it is not possible to distinguish the influence of char formation and beam-induced structural changes on both the char formation and its influence on the onset of thermal degradation.

Residual gas analysis of thermally degraded irradiated polyimide samples

The analysis of the gas evolution during thermal degradation of irradiated polyimide samples was studied by means of TG-MS. For proton irradiated foils despite a small increase in H_2O evolving at temperatures below 200°C no significant change in gas evolution appears. Presumably, this is because of the low energy loss of protons which does not lead to major changes of the chemical structure. The absence of increased gas emission supports the assumption that the decreased char residue found after thermal degradation is not induced by changes in the molecular structure, but is due to the irradiation environment (air). The increased absorption of water of irradiated polyimide has been described for gamma and neutron irradiated samples.

Samples irradiated with different fluences of Ta ions reveal that at 400°C mainly the formation of H_2O (m/z= 17,18), CO (m/z=28) and CO_2 (m/z=44) is increased (Fig. 5.15) while at 550°C the typically observed CO formation decreases relatively to the other outgassing species and totally vanishes at the highest fluence of 5×10^{12} Ta-ions/cm^2 (Fig. 5.16).

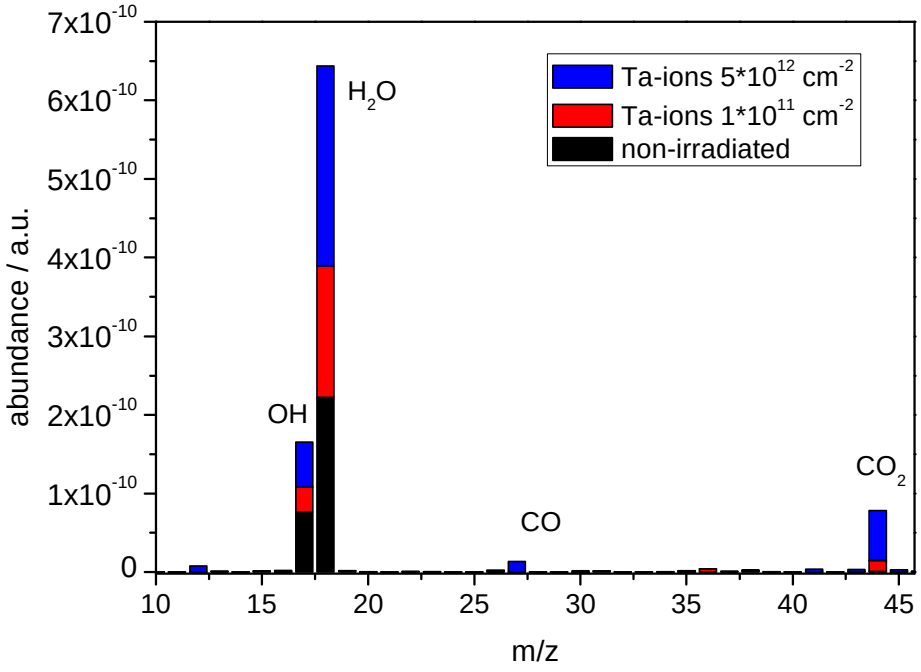

Fig. 5.15 Mass spectra of 11 MeV/u Ta-ion irradiated polyimide at 400°C

This observation is explained by the proposed heavy-ion induced production of carboxylic acids [196], [197] or the rearrangement of an imide into an isoimide [198]. CO, which is found to be the main outgassing product during ion irradiation (in-situ MS analysis), stayed constant until the final fluence of 1×10^{12} Au-ions/cm^2. This means that the decreased amount of CO found at $T_{d,max}$ (already at low fluences) cannot be explained with less outgassing and resulting absence of CO, but in a reduced temperature at which CO starts outgassing. However, at lower temperatures only the CO_2 formation is increased significantly. A possible explanation of this behaviour is the thermal degradation route which via CO formation leads to carboxylic acids [186] and isomerisation from imides to isoimides. Assuming that degradation induced by heavy ion irradiation favours this degradation path explains the increased formation of CO_2 at lower temperatures as well as the relatively low CO production at higher temperatures. The total absence of CO at $T_{d,max}$ for samples irradiated with the highest fluence could be attributed to the fact that nearly all carbonyls are

already degraded. Unfortunately this could not be cross checked with in-situ RGA due to the limited beamtime. One would expect a decreasing CO signal at high fluences where overlapping of damaged regions becomes significant.

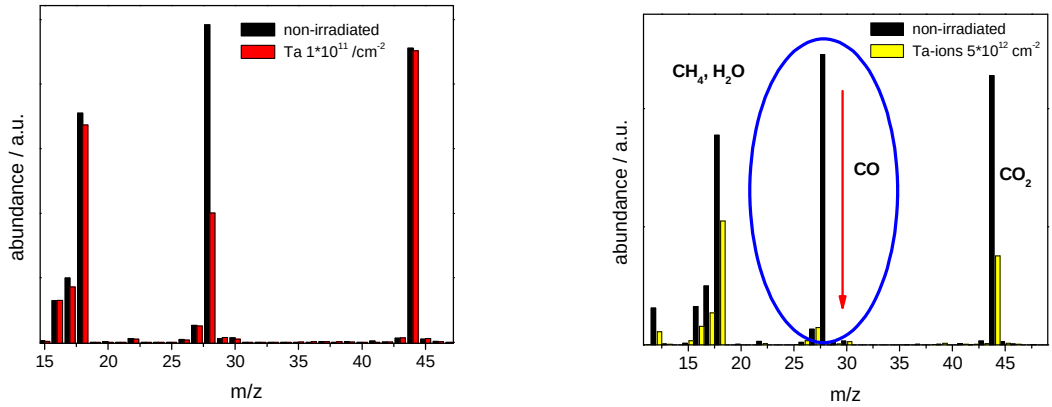

Fig. 5.16 Mass spectra at the temperature of highest decomposition for 11 MeV/u Ta-ion irradiated polyimide foils

Concerning the absolute amount of evolving gases, without a true calibration, it can be anticipated that with increasing fluence, a smaller amount of gas is evolved (as indicated by the decrease in total ion-count in Fig. 5.17) in agreement with the higher char residue found. However, this conclusion is semi-quantitative because of the strong influence of the measurement conditions on the results of the analysis. True quantifications of TG-MS data can only be performed using internal standards (not possible with our samples) or careful control of the gas flow through the TG-MS [199].

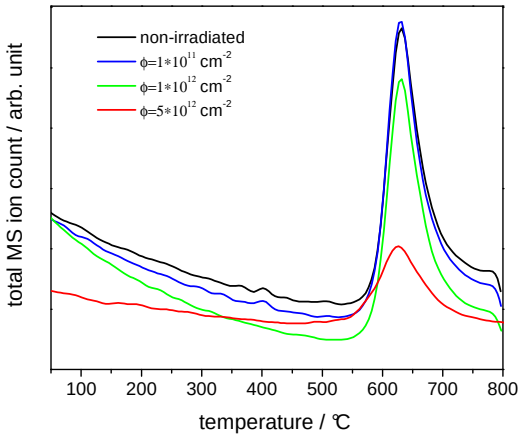

Fig. 5.17 Total MS ion count versus temperature for 11 MeV/u Ta-ion irradiated polyimide

The degradation mechanism of polyimide induced by energetic ion beams

Numerous groups investigated the interaction between energetic heavy ions and polyimide type polymers. Despite the overall degradation of the polymer [120] as well as ion induced carbonization [59] the synthesis of degradation products such as cyanates and alkynes is found. Fig. 5.18 a shows a plausible degradation mechanisms as described in refs. [184][185]. A sufficient explanation how the ion beam triggers the synthesis of -NCO and carbon-carbon triple bonds is found in the cleavage of the imide group which leads to the formation of CO, phenyl isocyanate, ethyne and a biradical at the phenyl residue (1 in Fig. 5.18 a). This radical furthermore reacts in different pathways forming CO, isomeric isocyanates as well as carbon clusters (reaction scheme b in Fig. 5.18).

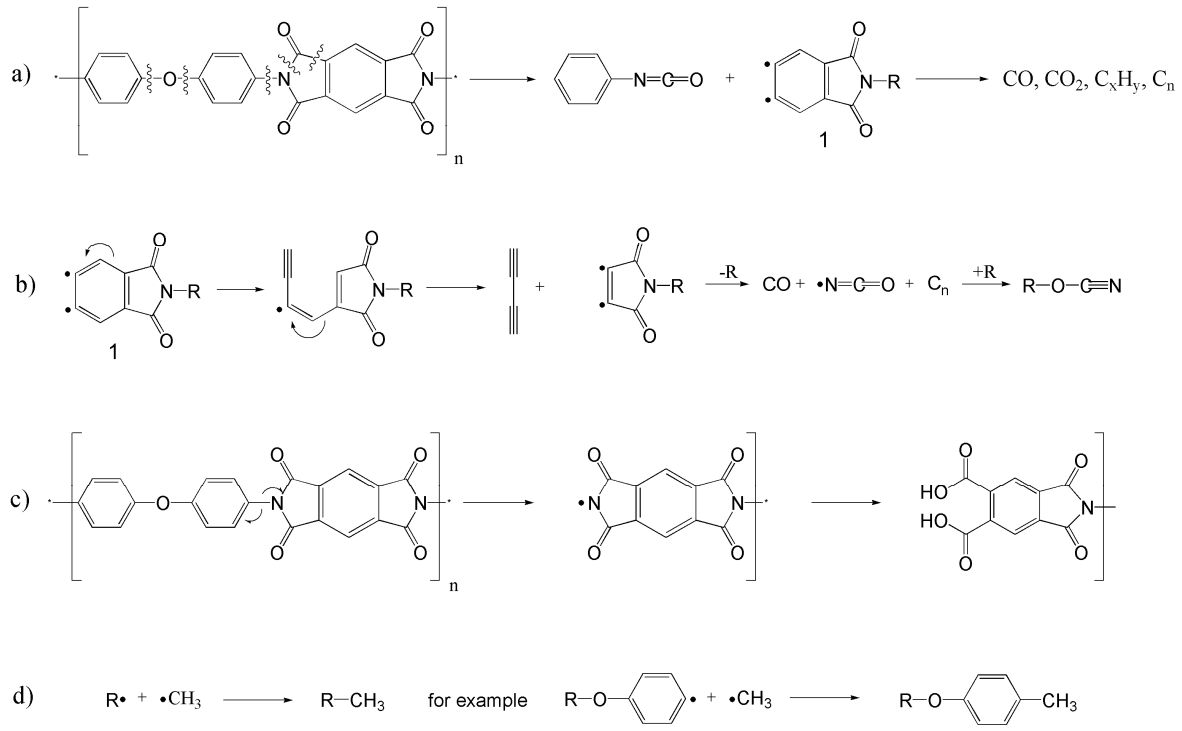

Fig. 5.18 a) and b) show summary of proposed degradation mechanisms from refs. [184], [185]. c) and d) show reasonable reaction pathways which lead to carboxylic functional groups and branching with aliphatic compounds

In the literature, no mechanism describes the production of a non-volatile carboxylic acid as discovered in this study. In Fig. 5.18c a possible synthesis path of a carboxylic acid not degassing from the bulk polymer is proposed. Breaking of the C-N bond produces an imide radical. Hydrolysis of this radical possibly produces a carboxylic acid. A similar reaction was proposed for the degradation mechanism of polyimide during pyrolysis [186]. Secondly, the ring opening of polyimide leading back to polyamic acid (repolymerization) would produce a

carboxylic group. In case of thermal degradation, the emission of CO_2 is ascribed to isoimide moieties initially present in the polymer and a steady state of CO_2 emission suggests the isomerisation of polyimide to an isoimide [127]. Isoimides are a common side-product during the second step of imide synthesis, e.g. the ring closure of the amic acid (Fig. 5.19) [51]. However, the IR spectra of neither non-irradiated nor irradiated sample show the typical IR bands of isoimides (1820 cm^{-1}-1795 cm^{-1}). Therefore the suggestion of ion induced formation of carboxylic acids explains both IR and MS results.

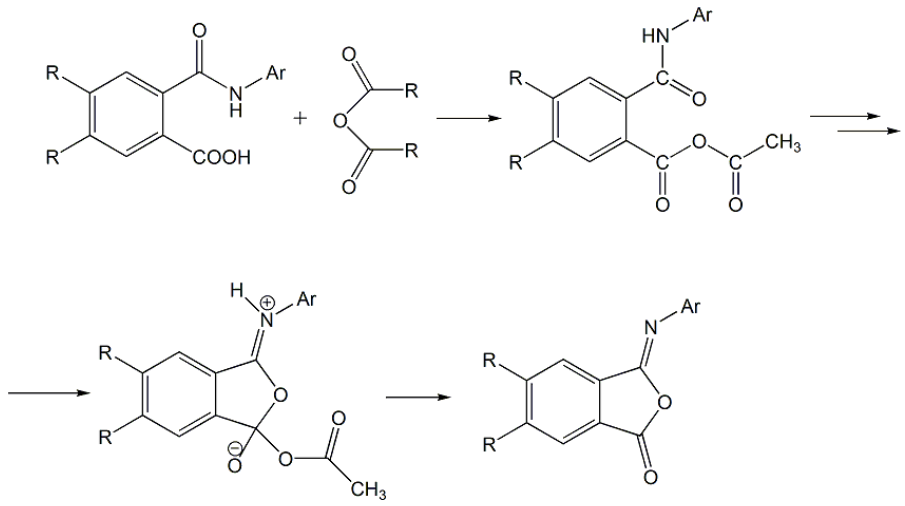

Fig. 5.19 Proposed mechanism of isoimide formation during the second step of polyimide synthesis

An explanation for the formation of saturated hydrocarbons is found in analogy to the radiolysis of polytetrafluoroethylene (PTFE). In Reference [200] it is demonstrated that in the electron beam induced radiolysis of PTFE a -CF_3 radical is formed which recombines with the backbone to a -CF_3 side group. In this way it is possible to branch PTFE with -CF_3 side groups. In polyimide a similar synthesis of -CH_3 side groups coming from the recombination of a -CH_3 radical with the polymer backbone seems reasonable. This mechanism is supported by the detected CH_4 (m/z=16) as a minor outgassing product, but still needs verification by other methods for example nuclear magnetic resonance spectroscopy.

Changes in FAIR-Relevant Material Properties of Irradiated Polyimide

Dielectric strength

Optical and microscopic observations

After breakdown tests, as described in chapter 3.7, the damaged surfaces of pristine and irradiated 50-μm thick polyimide samples were inspected by scanning electron microscopy (Fig. 5.20). The breakdown holes of non-irradiated, gamma, proton and carbon ions irradiated samples are round holes, whereas polyimide samples irradiated with heavier ions are found as more irregular-shaped holes or even double holes. The material at the rim shows a porous morphology with large, up to μm-sized cavities and cracks indicating the increased brittleness of the irradiated material. The eroded area and the size of the breakdown holes become larger with increasing ion fluence in agreement with earlier observations of neutron-irradiated glass-fiber-composite polyimide laminate [201].

Dielectric strength of polyimide irradiated under normal beam incidence

The dielectric strength of all irradiated polyimide samples was found to be directly related to radiation induced degradation which depends on dose, energy, and type of irradiation. Fig. 5.21 and Fig. 5.22 comprise the breakdown results for samples from different irradiations by plotting the dielectric strength as a function of accumulated dose. Each data point represents the mean value from measurements of 3-8 individual samples, error bars correspond to the mean standard deviation. Due to the limited number of samples, the results for gamma-irradiated foils are based on a single measurement.

For irradiations with gammas or protons of doses up to 10-20 MGy, the dielectric strength scatters around the standard value of non-irradiated material. Above this dose, the insulating property decays but remains within 90 % of the value of pristine foils at the highest tested dose of 82 MGy (21-MeV protons, 2×10^{16} cm^{-2}). For samples irradiated with heavy ions, the dielectric strength significantly degrades with increasing dose. The process is more pronounced for ions species of higher mass and energy loss. It is very important to note that heavy ion beams alter the electric strength already at an extremely low dose of 100 Gy. In the dose range 1-10 MGy, the breakdown voltage is only slightly higher than for a 50-μm thick layer of air (breakdown voltage ~700 V). The low dose effect of heavy ions is more obvious when plotting the same data as a function of fluence.

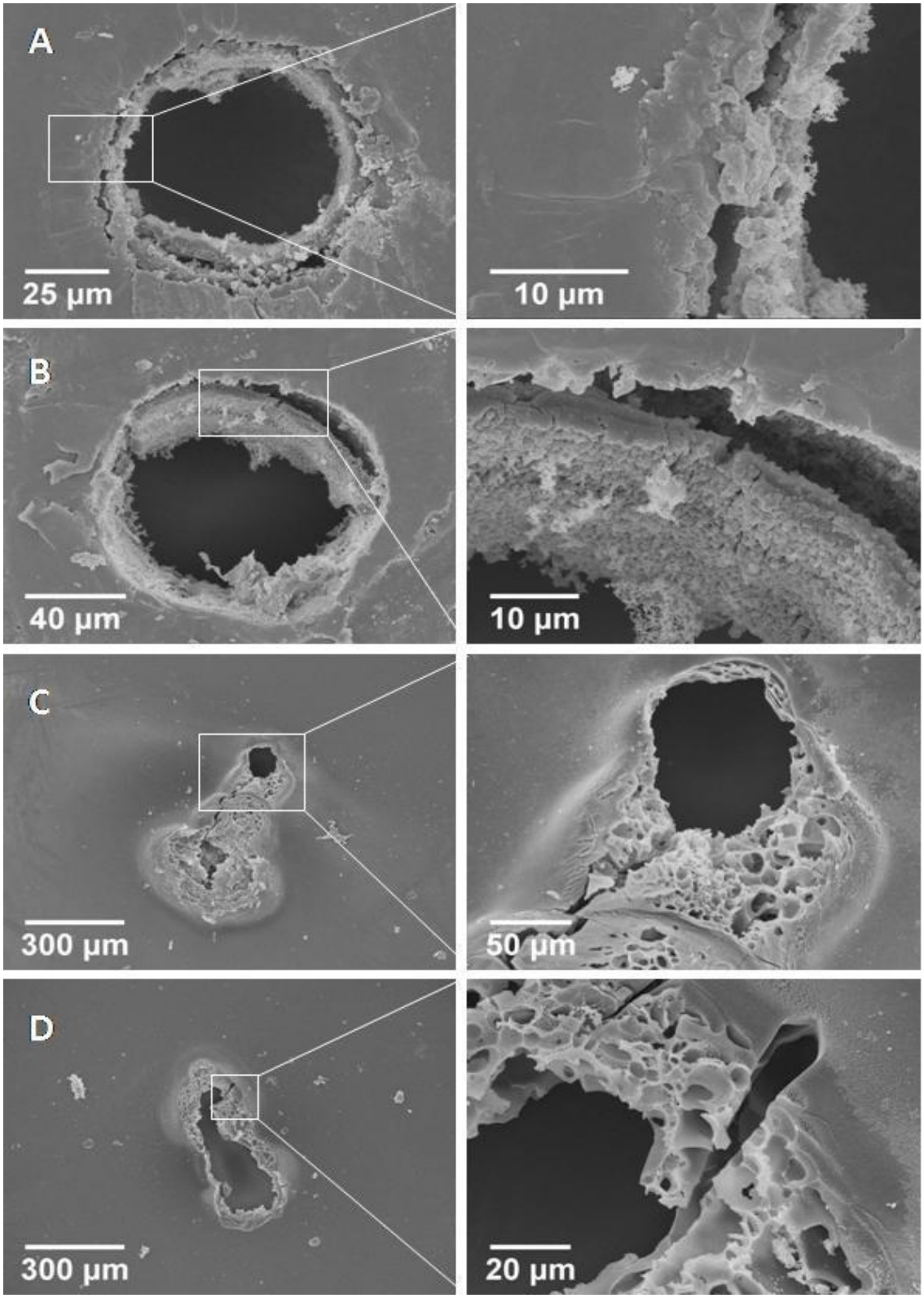

Fig. 5.20 Scanning electron micrographs of sample surfaces after breakdown tests showing typical breakdown holes in low (left) and high (right) magnification in 50-μm thick non-irradiated polyimide (A), and in foils irradiated with 640-MeV Ni-ions of fluence 1×10^{10} cm^{-2} (B), 1×10^{12} cm^{-2} (C), and 5×10^{12} cm^{-2} (D). Reprinted with permission of [202].

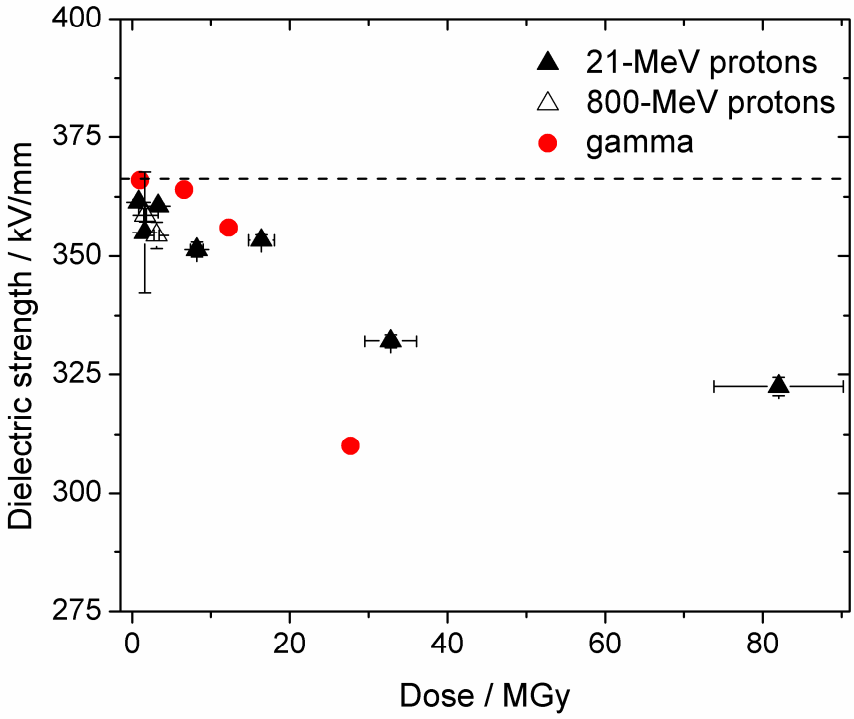

Fig. 5.21 Dielectric strength of polyimide irradiated with gammas (Co^{60} source) and protons as a function of dose. The dashed line corresponds to the pristine value. The maximum dose corresponds to a fluence of 5×10^{15} cm^{-2} (800-MeV protons) and 2×10^{16} cm^{-2} (21-MeV protons). Reprinted with permission of [202].

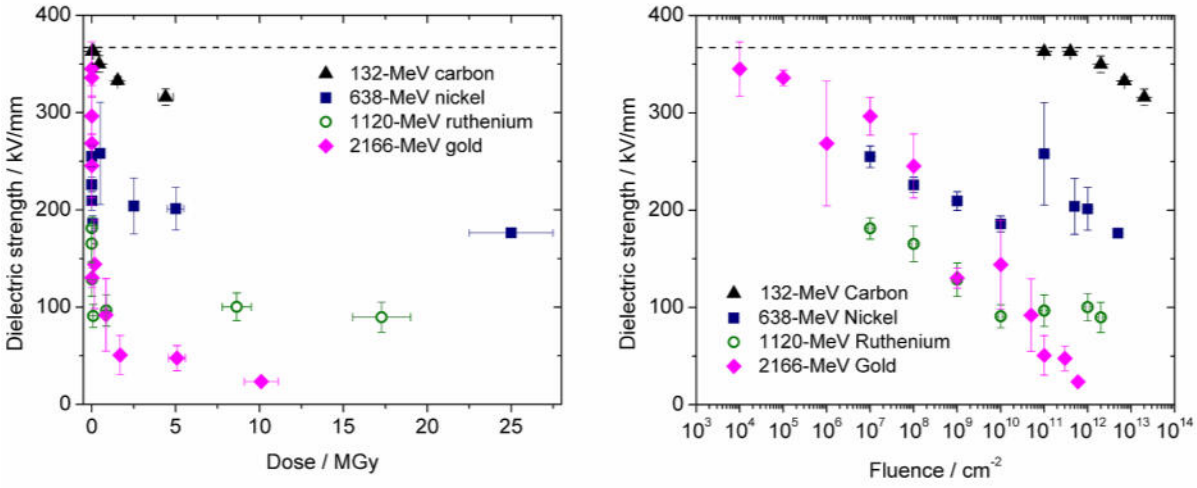

Fig. 5.22 Dielectric strength of polyimide irradiated with various heavy ions as a function of dose (left) and in a semi logarithmic plot as a function of fluence (right). The dashed line corresponds to the pristine value. Reprinted with permission of [202].

Angular dependence of heavy ion induced changes in the dielectric strength of polyimide

In addition to the samples irradiated under normal beam incidence the breakdown voltage of 50-μm thick polyimide foils exposed under 45° (Fig. 5.23) was measured. Under this geometry, the length of the ion tracks is larger by a factor of $\sqrt{2}$ than the thickness of the foil and thus as the track length produced under normal incidence.

The measured breakdown voltage of samples exposed to the tilted ion beam was found to be larger than a factor of $\sim \sqrt{2}$ compared to normal beam incidence. This is an indication that the breakdown process does not simply depend on the foil thickness but scales with the length of the ion tracks.

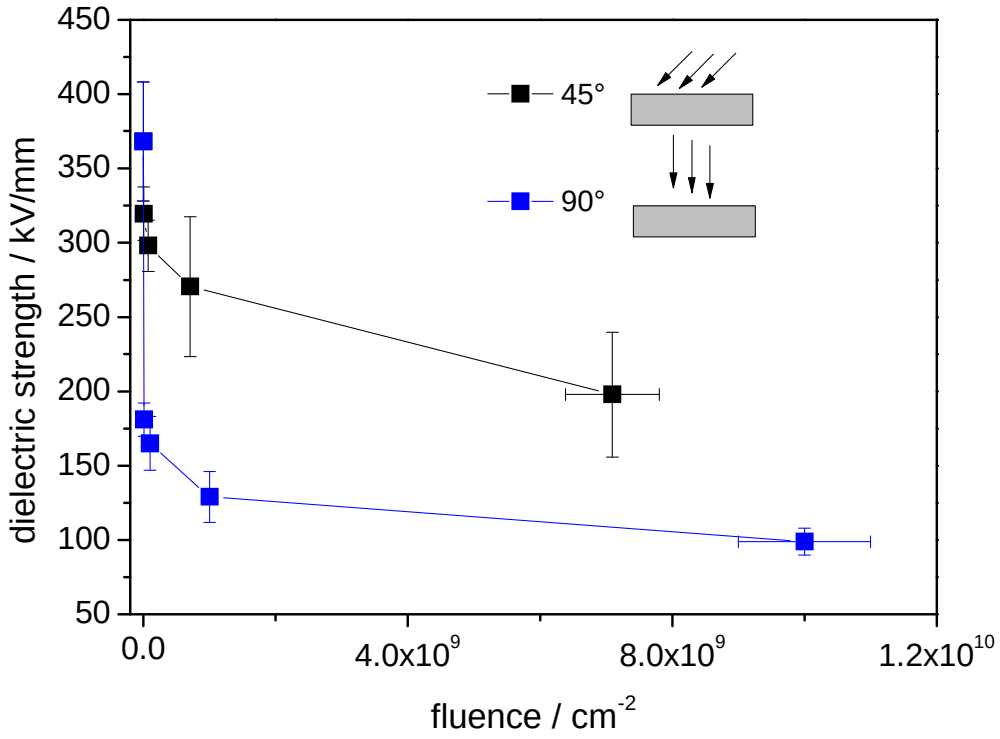

Fig. 5.23 Breakdown voltages for 50-μm thick polyimide foils (Apical AV) irradiated with 1120-MeV Ruthenium ions under normal and 45° beam incidence. Lines are guides to the eye only.

With increasing fluence, the average distance between neighboring ion tracks decreases. If the distance becomes sufficiently small the breakdown proceeds by bridging neighboring tracks. Under this condition, the breakdown voltage of samples with tilted tracks should become equal to values for foils exposed under normal incidence. Within the fluence regime used in this part of the study no significant overlapping of the tracks is expected.

Weibull analysis

To predict failure probabilities of polyimide for the later application as insulator in magnets the breakdown voltage data of 25-μm thick polyimide foils irradiated with Ru ions under normal incidence were evaluated by means of Weibull statistics. This approach is widely used in reliability engineering and failure analysis. Fig. 5.24 shows the Weibull plots for breakdown measurements of non-irradiated and irradiated foils. The experimental results are in good agreement with the Weibull fits (solid lines), although data do not exactly follow Eq. 7 (page 29).

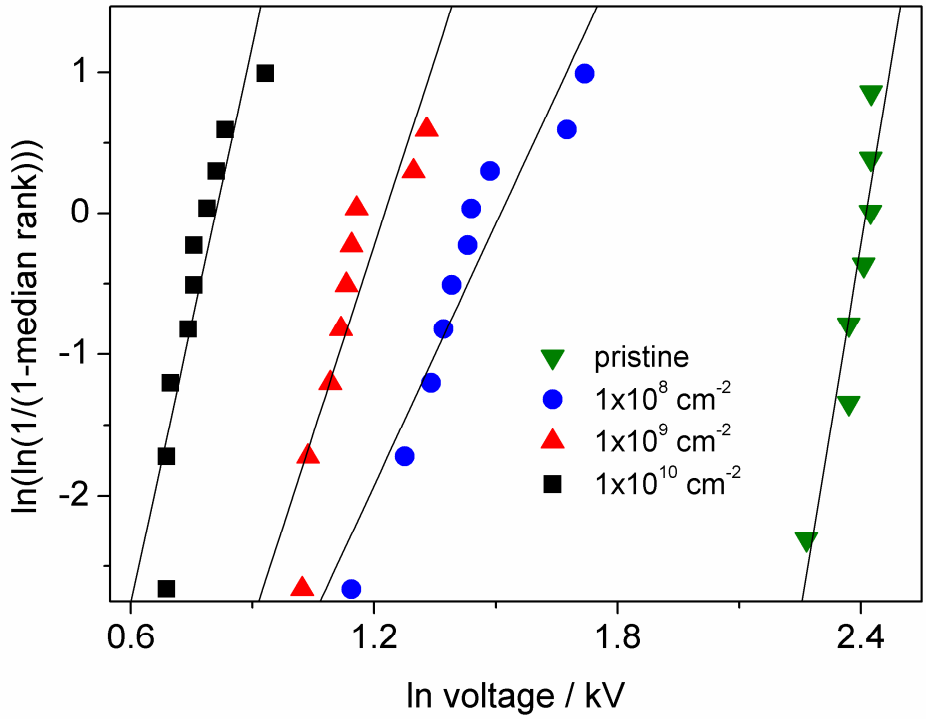

Fig. 5.24 Weibull plots using the linearized form and associated fits for sets of pristine and irradiated polyimide samples. Reprinted with permission of [202].

Table 5.4 shows failure probabilities calculated from the Weibull distribution at 1.67 kV, the designed voltage limit required for the FAIR magnets. Between the non-irradiated foils and the highest tested fluence (1×10^{10} Ru-ions/cm^2), the failure probability increases from close to zero to about 6.7 %.

Table 5.4 Fit parameter of Weibull analysis: β is the shape parameter and α denotes the Weibull characteristic lifetime. The 25-μm thick polyimide foils were irradiated with 1112-MeV Ru-ions. The failure probability was determined at 1.67 kV

Fluence (cm^{-2})	(β)	(α) (kV)	Failure probability (%)
0	27.1	11.1	0
1×10^{8}	5.4	4.5	0.5
1×10^{9}	4.0	3.6	4.6
1×10^{10}	11.0	2.2	6.7

Regarding the shape parameter, no systematic change is found with irradiation fluence. This means that the change in the spread of the distribution follows no clear trend and remains at values $\beta>2$. For these values the shape of the distribution is similar to a normal distribution. This indicates that in all measured sample sets there is an increasing failure rate with increasing voltage, and not a so-called early life failure ($\beta<1$) or constant failure rate ($\beta=1$). This just mirrors the ageing of the material during the measurement due to the electrical field.

Discussion of dielectric strength of ion-irradiated polyimide

Dielectric breakdown in polymers has been studied for decades. Many theories have been proposed in an attempt to explain observed phenomena. However, many problems still remain unsolved. To summarize the main theories, the electrical breakdown is characterized by the electrical, mechanical and thermal properties of the investigated material, as well as its chemical structure and manufacturing quality. In general, the dielectric breakdown is accompanied by the destruction of the molecular structure and formation of a conductive material ("treeing") [90]–[92]. It can be divided into the "tree inception" and "tree propagation" [93], [95]. In polymeric high voltage insulations the tree inception time mainly depends on the conductor, whereas the tree propagation time depends on the insulating properties [96]. Depending on the type of material and the number of pre-existing defects, the formation of a conductive path may be slow, but once a percolation path exists the breakdown suddenly appears in an abrupt and damaging way. Quick charge movement initiates electrical heating (Joule heating), leading to electrical and thermal damage, destroying the insulator along the formed path.

Ion irradiation is known to degrade mechanical and thermal properties of polymers due to bond scission, and induce electrical conductivity because of creation and percolation of carbon clusters [58], [192]. Changes induced by light ions which have a low stopping power are smaller, different or even non-existing due to certain energy thresholds for given material changes [50][203]. Our results follow this trend. Gammas and protons induce only minor changes. At higher stopping powers, degradation starts to increase at low irradiation fluences. The decrease in dielectric strength for heavy ions (≥ Ni) follows a half logarithmic law with increasing fluence, quite similar to the one observed for insulating matrices containing increasing amounts of conducting particles such as carbon black, carbon nanotubes or metal powders [204]–[206]. This indicates that in the case of heavy ions percolation of carbon clusters or induced electrical conductivity starts to occur within single tracks. Similar to this suggestion, ion induced conductive tracks have been found in amorphous diamond-like carbon films [207]. It should be pointed out that for heavy ions already low fluences create a serious risk for having electrical breakdown. However, as mentioned earlier, not only electrical conductivity but also thermal and mechanical properties change during irradiation. From our measurements it is impossible to deduce which effect is dominating and it is very likely that they are additive.

Furthermore, the results show that the breakdown voltage of polyimide samples irradiated under 45° is a factor of 1.5-1.7 larger compared to the samples irradiated under normal incidence. We therefore consider that the breakdown tree follows the ion track, or that the jumping of the tree between non-irradiated and irradiated regions of the material delays the tree percolation. If we consider equivalent breakdown strengths of each track, a factor of 1.4 is expected due to the increased track length. The slightly higher values might be explained by the mixture of both processes measured. Increasing the track length increases the volume of material which has to be degraded as well as increases the delay of the breakdown due to the tree propagation time. Since the ramping speed of the voltage is kept constant during all measurements, this increase in tree propagation time will increase the measured breakdown voltage additional to the higher energy required to form the breakdown hole.

Conclusions of dielectric strength data on ion irradiated polyimide

Overall, the dielectric strength of polyimide is decreased due to ionizing radiation in the observed regime. Gamma and ion beam irradiations, which have a low energy loss (protons and carbon ions), cause less damage compared to heavy ion irradiation (≥Ni). Breakdown

voltage of samples irradiated with Ru ions under 45° of incident angle show higher values due to the increase in track length. The technical specification of the FAIR superconducting magnets` insulation is defined to be ~5 kV for 3 layers of 25 μm thick polyimide films. For a single 25 μm foil this corresponds to an electrical field of 1.67 kV. It can be stated that the polyimide samples irradiated with gammas and protons are still within the specification after a dose of about 28 MGy and 80 MGy respectively, whereas the heavy ion irradiations follow a different trend. Degradation starts orders of dose magnitudes earlier and their insulating properties are at the limit of the specification at a dose of about 1 MGy. Weibull analysis of a selected dataset clearly demonstrates that at the specified maximum electrical field, the failure probability of the insulation is dramatically increased in the case of heavy ions. During FAIR-operation, the angle of lost beam is expected to be in the order of 1-2° gracing incidence. The secondary fragments produced have an angular distribution with a preferred forward direction. Therefore secondary particles will penetrate the magnet coil under grazing incidence. For samples irradiated under an incident angle of 45° the measured breakdown voltage follows the penetration length of the ion induced track. Ion radiation with grazing incidence should produce even less damage to the bulk insulating properties. Each part of the magnet coil will be exposed to a different secondary spectrum depending on the incident angle of the lost beam as well as the different location of each component. The magnets will see thermal cycles as well as pulsed mechanical forces. Not only polyimide but also glass fiber reinforced plastics, polyvinyl formal (FormvarTM) and polyvinyl alcohols (PVA) are used for insulation purposes.

The results provide a first indication that individual tracks induced by heavy fragments completely passing through the polyimide insulation represent failure paths facilitating dielectric breakdown processes. As a recommendation the magnet coil should be shielded against heavy fragments in areas where calculations show its necessity.

Low temperature thermal properties of ion irradiated polyimide

Low temperature thermal conductivity

The reproducibility of the thermal conductivity measurement set up (as described in) was tested for 3 individually prepared polyimide samples and within 10% (Fig. 5.25).

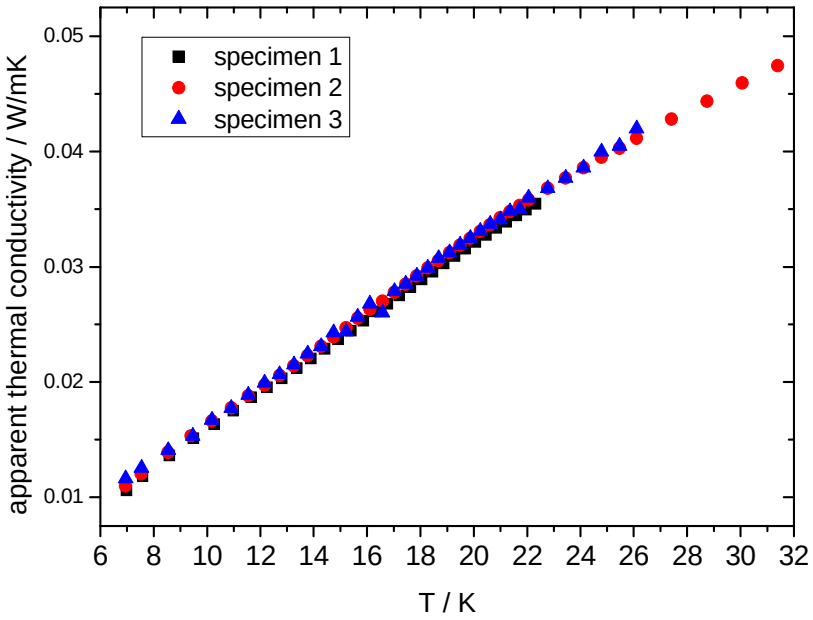

Fig. 5.25 Thermal conductivity of three non-irradiated 125 μm thick polyimide foils. Error of temperature measurements using silicon diodes is less than 4%.

Several groups reported thermal conductivity data of Kapton-type polyimide over a wide temperature range [208]–[213]. In all of these works the thermal conductivity is found to be proportional to T in the investigated temperature range. Best fits were found using the allometric function. In Fig. 5.26, a fit of our data (blue line) is compared to fit functions of values given in literature (red lines). The deviations are ascribed to the different measurement techniques as well as to differences in film thickness and manufacturer of the PI films. A direct comparison of the reported values is thus difficult. However, it can be seen that the obtained values scatter by a factor of approximately 5 and our measurements on a single 125 μm foil show reasonable values.

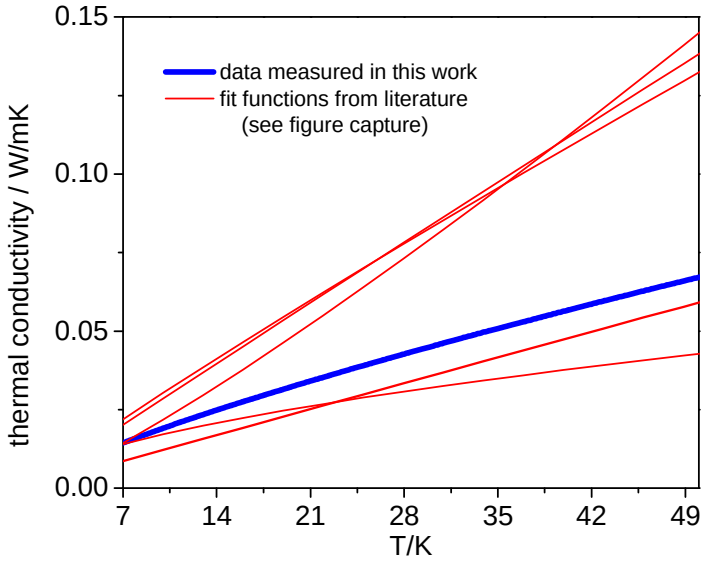

Fig. 5.26 Thermal conductivity of 125 μm thick polyimide measured in this work (blue line) and fit curves from data in Refs. [208]–[213] (red lines).

For heavy ion irradiation, the thermal conductivity of polyimide decreases with increasing irradiation dose (Fig. 5.27). At the maximum dose of 25 MGy for Ni-ion irradiation, the thermal conductivity has decreased by 50 %. A possible explanation for this behavior is the formation of defects and amorphization. This results in an increased phonon scattering, hindering thermal transport, which is similar to the results reported by Briskman, who found a decrease of the thermal conductivity of polyethylene terephtalate (PET) irradiated with high energy protons [214], [215] and results on neutron irradiated graphite [216]. Since it is known that ion irradiated polymers become carbonized, accompanied with electrical conductivity, it can be stated that the increased phonon scattering has a stronger influence than the heat carried by the electrons, which additionally contribute to the heat transfer. In similarity some sorts of graphite (especially polycrystalline nuclear grade type graphite, such as AGOT [217] or pitch bonded graphite [218]) were found to have the lowest thermal conductivity at low temperature measured so far [118].

Additionally to the decrease of thermal conductivity after ion bombardment, it can be stated that the plateau regime found for amorphous materials (explained in chapter 2.3) cannot be registered in ion irradiated polyimide within the observed fluence regime. An appearance of the plateau would have indicated total amorphization of the polymer and was expected due to the known ion induced amorphization in various crystalline materials. This behavior is interpreted by the lack of a totally amorphous material after ion irradiation. For example,

Calcagno et al. found small graphite crystals in carbon derived from keV-MeV ion irradiated polymer samples [219] explaining the observed trend.

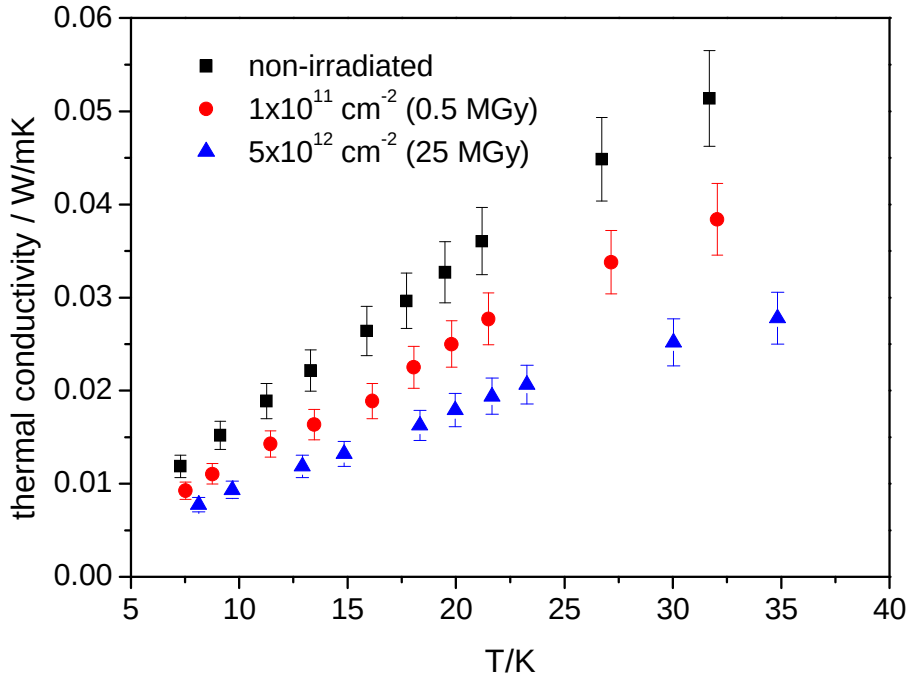

Fig. 5.27 Thermal conductivity of non-irradiated polyimide (black squares) and samples irradiated with 11 MeV/u Ni-ions. The red point and blue point curve correspond to irradiation doses of about 0.5 and 25 MGy respectively. Error bars show 10% error estimated by the reproducibility measurements.

Heat capacity of ion irradiated polyimide

Complimentary to the low temperature thermal conductivity of ion irradiated polyimide heat capacity measurements were carried out with non-irradiated polyimide and a sample irradiated with 5×10^{12} Ni-ions/cm^2 (~25 MGy) in the temperature range from 2-300 K.

Fig. 5.28 shows the obtained volumetric specific heat measured in comparison with the standard value of the National Institute for Standards (NIST) and with data found in the literature and unpublished results derived through private communications [220],[221],[222].

The measured value of non-irradiated polyimide is very similar to those derived by V. Zubko [221] and the NIST standard value [220].

For ion irradiated polyimide an increased specific heat is found at very low temperatures (<4 K) and a decrease at higher temperatures; the latter being consistent with the lower thermal conductivity found as previously shown. Table 5.5 lists the changes and the relative

changes at 5 selected temperatures. After the transition from higher to lower specific heat at low temperatures the maximum difference starts to be quite constant having a value of -13 %.

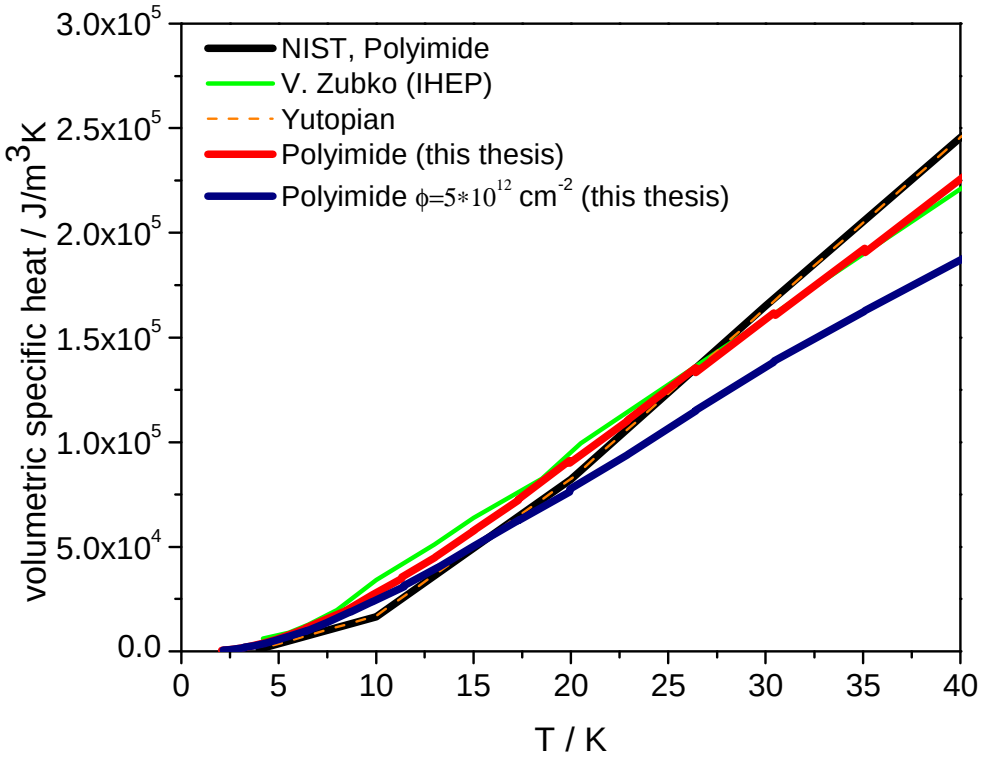

Fig. 5.28 Volumetric specific heat versus temperature data of polyimide measured by different groups and volumetric specific heat of 125-μm polyimide irradiated with 11 MeV/u Ni-ions

Table 5.5 Difference in volumetric specific heat of ion irradiated polyimide calculated exemplary for 5 temperatures in the low temperature regime.

Temperature / K	C_V non-irradiated / J/m^3K *	C_V irradiated / J/m^3K *
2	521	591
4	3922	3792
8	19701	18875
16	65135	56125
35	191566	166200

*: estimated error is in the order of 10%

Conclusion on low temperature properties of ion irradiated polyimide

In conclusion, the results clearly demonstrate that the thermal conductivity and volumetric heat capacity of polyimide insulations will decrease with extending operation time of the FAIR magnets. That means that depending on the expected radiation dose of the

superconducting magnets, possibly higher heat power values have to be considered when quench heaters are designed. In addition, the quench behavior of the magnet is changing and could lead to earlier quenches because of the reduction in heat dissipated through the insulation material.

The true effect of this has to be simulated and calculated to really show how these effects will combine. Performance of these simulations was not the scope of this thesis, but will be carried out by the magnetic design department.

It should be noted that the used Ni-beam has to be considered as a worst case scenario keeping in mind beam fragmentation calculations in chapter 1.6 showing that the heavy ion contribution to the secondary radiation in the later application has the highest portion in a small volume at the surface of the material (directly next to the beamtube), not at the whole superconducting coil and its supporting structure.

5.2 Polyepoxy/G11-Type Glass-Fiber Reinforced Plastic:

Beam Induced Structural Changes in Polyepoxy and G11

This chapter deals with heavy ion induced changes of cured polyepoxy and G11-type GFRP. IR spectroscopy (in-situ and ex-situ ATR) and RGA (in-situ), as described in Chapter 3, were used to analyze the degradation mechanisms on a molecular level.

G11 composites as used for FAIR magnets contain both a polyepoxy matrix and multiple layers of woven glass-fiber bundles. For spectroscopic analytical methods, such as IR-spectroscopy, samples are either too thick (order of mm) or the glass fibers show strong absorption bands hiding the degradation of the polymer matrix. Because of this, thin (~8-15 μm) amine cured polyepoxy foils were synthesized (as described in chapter 3.1), irradiated (chapter 4.4), analyzed and wherever applicable compared with data obtained from the G11 composite assuring the similarity of the used polymer system compared to the composite.

In-situ IR-spectroscopy of cured polyepoxy:

Results are displayed in Fig. 5.29 showing the IR spectra of non-irradiated polyepoxy foil and after irradiation with 1×10^{12} cm^{-2} of 4.5 MeV/u ^{197}Au ions. Next to new developing peaks it can be noted that nearly all IR bands (assigned in chapter 3.3) present in the non-irradiated sample decrease due to the molecular destruction induced by the ion beam.

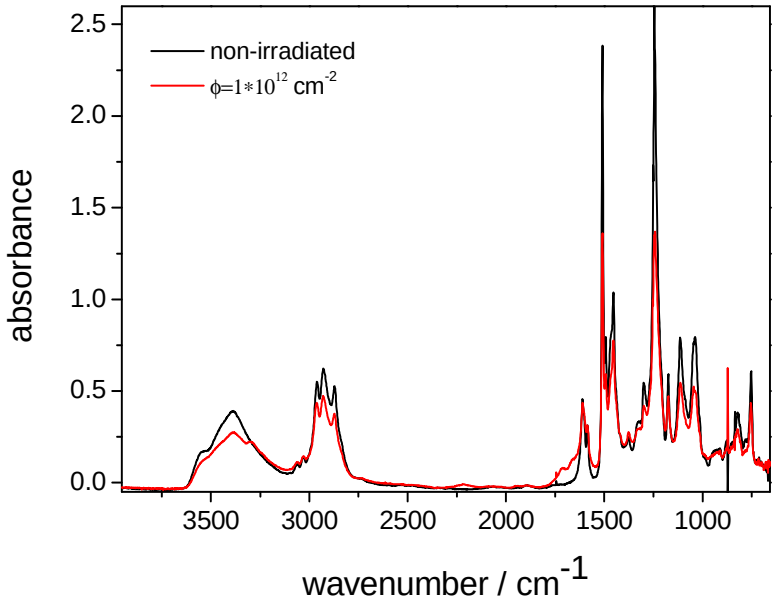

Fig. 5.29 FT-IR spectra of non-irradiated and 4.5 MeV/u Au-ion irradiated cured polyepoxy foil (~10 μm thick). For a better visibility only the spectra of non-irradiated polyepoxy and the highest fluence are presented.

Next to the decrease in band intensities, a shoulder appearing at 3300 cm^{-1} can be identified (Fig. 5.30). This band is interpreted to derive from the C-H vibration of radiolytically produced terminal alkynes. The formation of terminal alkynes is a known phenomenon taking place within different polymers irradiated with swift heavy ions and seems to be independent of the molecular structure of the polymer. For example Balanzat et al. found the identified terminal alkynes in polyethylene (PE) and polyvinylidene fluoride (PVDF) [223], Steckenreiter et al. observed similar absorption bands in polyimide (PI), polycarbonate (PC), and polyethylene therephtalate (PET) [168], [184], [196]. Terminal alkynes are known to show three vibrational bands: one strong absorption due to symmetric stretching of C-H in the regime near 3300 cm^{-1}, a weak absorption at about 2200 cm^{-1} deriving from the vibration of the carbon-carbon triple bond, and a strong but wide absorption at around 632 cm^{-1} due to a deformation vibration of the C-H bond (in the appendix 5 exemplary IR spectra of different molecules bearing terminal alkynes are presented).

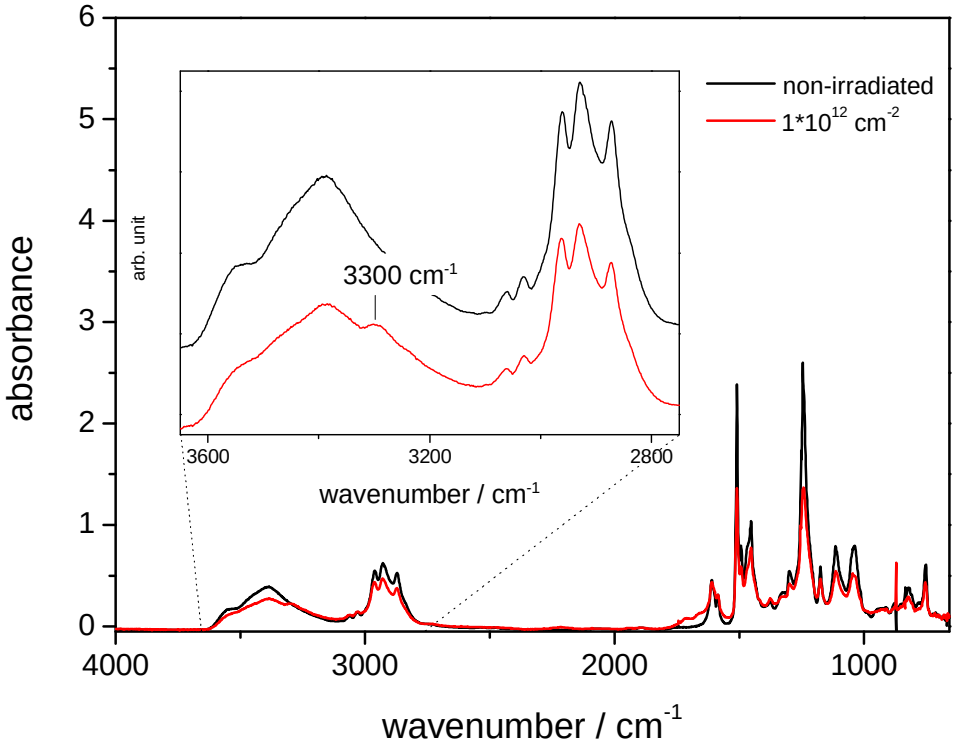

Fig. 5.30 FT-IR spectra as shown in Fig. 5.29 with a higher magnification to the wavenumber regime from 3650-2750 cm^{-1}.

Even though the formation of alkynes seems logical (explaining for example the increase in the absorption band at 2216 cm^{-1}, Fig. 5.31), it should be noted that the latter described

deformation band has only been identified in case of PE and PVDF. The absence of the alkyne deformation band in other polymers may be explained by the initial broadness of the polymeric absorption band, which broadens even more due to the mixture of alkyne-containing degradation products. Additionally, the molecular weight distribution is known to further widen by the ion beam degradation. All this could be responsible for the absence of the deformation band, but should be verified for final proof by means of solid state nuclear magnetic resonance in further studies.

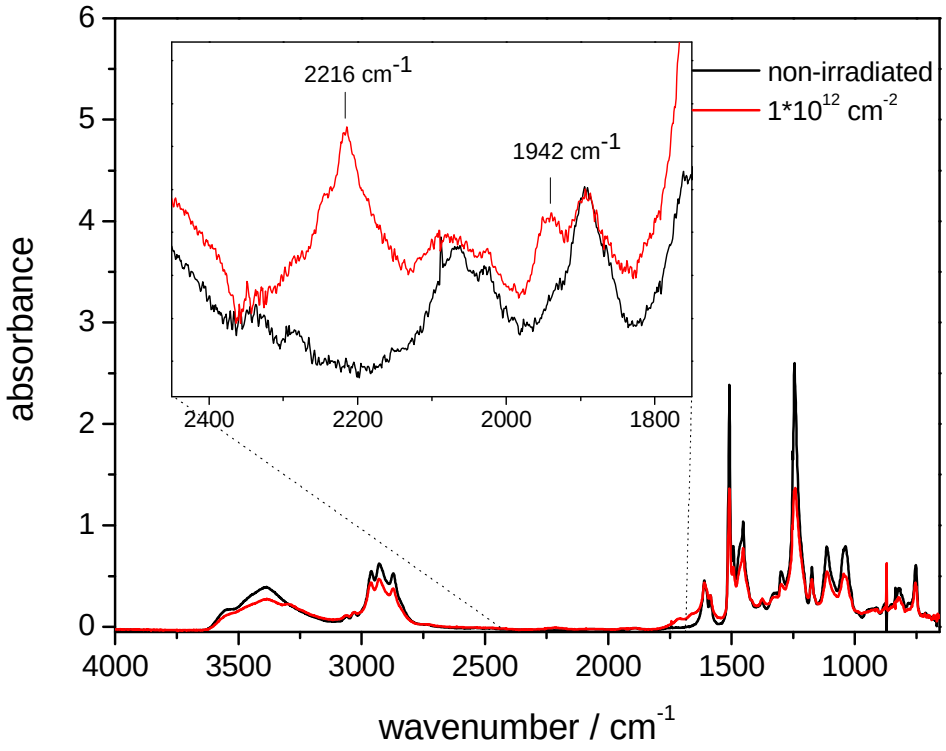

Fig. 5.31 FT-IR spectra as shown in Fig. 5.29 with a higher magnification to the wavenumber regime from 2460-1750 cm^{-1}.

In Fig. 5.31 the wavenumber regime between 2400-1800 cm^{-1} is shown. Next to the absorption at 2216 cm^{-1}, identified as vibration of the carbon-carbon and carbon-nitrogen triple bonds and/or ketenals or isocyanides cumulated double bonds, a peak at 1942 cm^{-1} can be seen. This peak, in principle being in the regime of carbonylic double bonds, is shifted to very high wavenumbers (standard carbonyl absorptions are strong absorptions found between 1800-1600 cm^{-1}), indicating an allene type of structure.

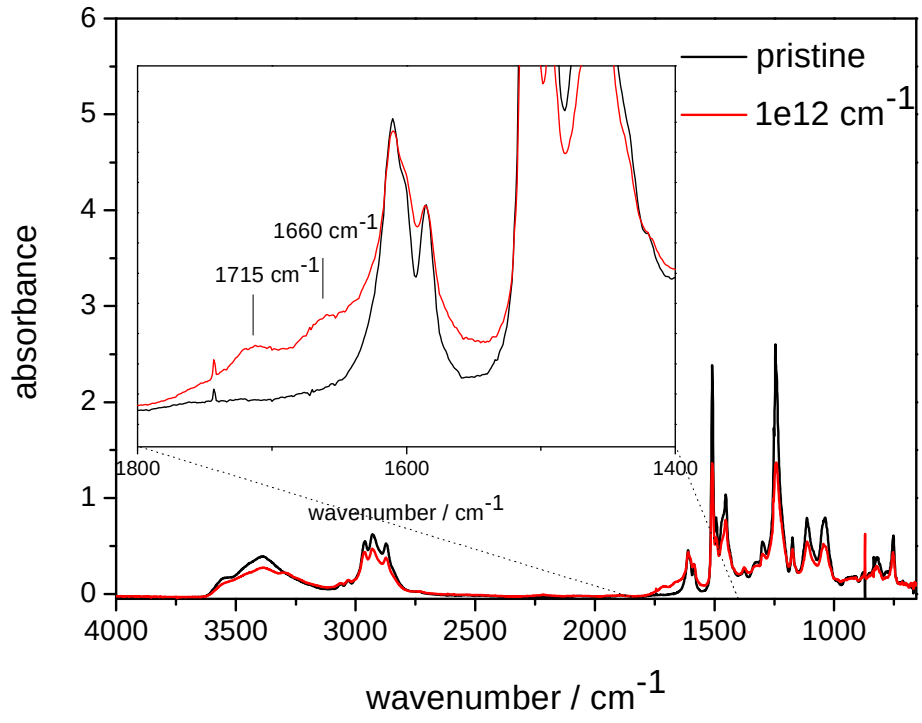

Fig. 5.32 FT-IR spectra as shown in Fig. 5.29 with a higher magnification to the wavenumber regime from 2460-1750 cm^{-1}.

In the last wavenumber regime (Fig. 5.32), broad peaks between 1800-1650 cm^{-1} are found. In this regime typical double bond formation takes place. In case of carbonyls derived by oxidation and in case of carbon-carbon double bonds arising via the elimination of hydrogen. The latter is found in all ion degradation studies of hydrocarbons and is typically one of the main outgassing products.

ATR-IR of irradiated G11-type GFRP

Fig. 5.33 shows the ATR-IR spectra derived from the surface of G11-type GFRP irradiated with 1×10^{12} Au-ions/cm^2. Despite the known decrease in band intensities of non-irradiated present bands, mainly two changes can be seen. (i) The increase of hydroxyl vibrational band and (ii) a strong absorption band at 1710 cm^{-1}. This band is identified as carbonyl absorption deriving from carbonyl double bonds. No evidence of alkyne-formation or radiolytic production of carbon-carbon double bonds can be found. The latter case might be masked due to existing absorption band at 1610 cm^{-1} deriving from phenyl vibrations. It seems that use of a coupling agent as well as the glass fibers change the degradation products slightly, compared to the in-situ IR investigations on cured polyepoxy film.

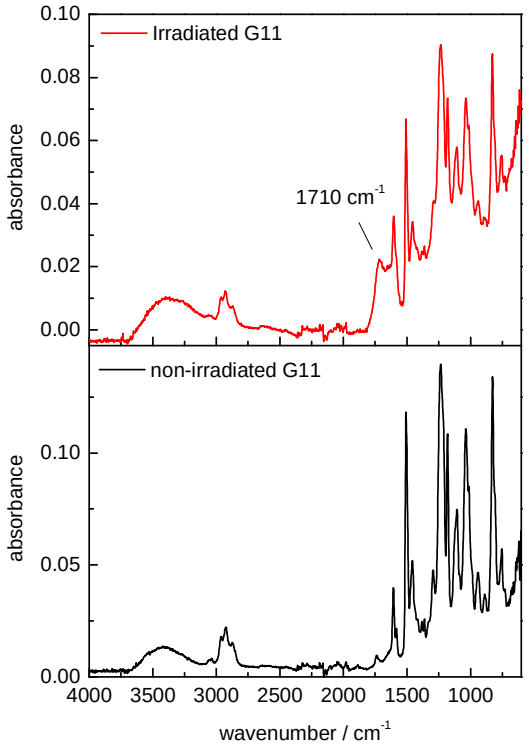

Fig. 5.33 ATR-IR spectra of non-irradiated and 11 MeV/u Au-ion irradiated ($\phi = 1 \times 10^{12}$ cm^{-2}) G11

Additionally, the ex-situ measurements could have lost information due to the formation of instable degradation products which disappear after the irradiation. It should be noted that the samples for ex-situ measurements typically have to cool down from the ion induced radioactivity for weeks up to months depending on the used energy and irradiation time.

The results will be discussed further together with the results of the residual gas analysis in more detail.

Residual gas analysis:

Polyepoxy:

The RGA spectra before and during ion irradiation of amine cured epoxy resin are shown in Fig. 5.34. Before the start of irradiation the spectrum is dominated by H_2O but also contains small amounts of CO and hydrocarbons. These hydrocarbons are not present in the empty chamber (without any sample) and originate from the outgassing of the target holder and the sample.

Irradiation of the sample leads to a significant increase of the intensity of many m/z values. Next to hydrogen, which is the dominating outgassing species, mainly hydrocarbons such as

CH_x (m/z=12-16), C_2H_x (m/z=24-30), C_3H_x (m/z=36-44) and C_4H_x (m/z=48-58), H_2O (m/z=16-18), CO (m/z=28), and N_2 (m/z= 14,28) are recorded. As background we recorded the irradiation of the sample holder without sample, therefore degassing from irradiated surfaces of sample holder and chamber wall are included (and substracted). In the case of sample irradiation the energy of the beam and its range in the sample holder is changed by 10%, i.e. the surface of the target holder is irradiated slightly different in comparison to the background spectrum without sample. Due to this and the unknown pumping speed of the system for different gases obtained values can be interpreted only in a qualitative way.

The intensity of the outgassing hydrocarbons C_xH_y decreases with higher carbon content and starts to be non-detectable above C_5H_x. This is a typical observation for mass spectra of aliphatic hydrocarbons. In comparison to thermal combustion processes of epoxy polymers only small amounts of CO_2 are produced.

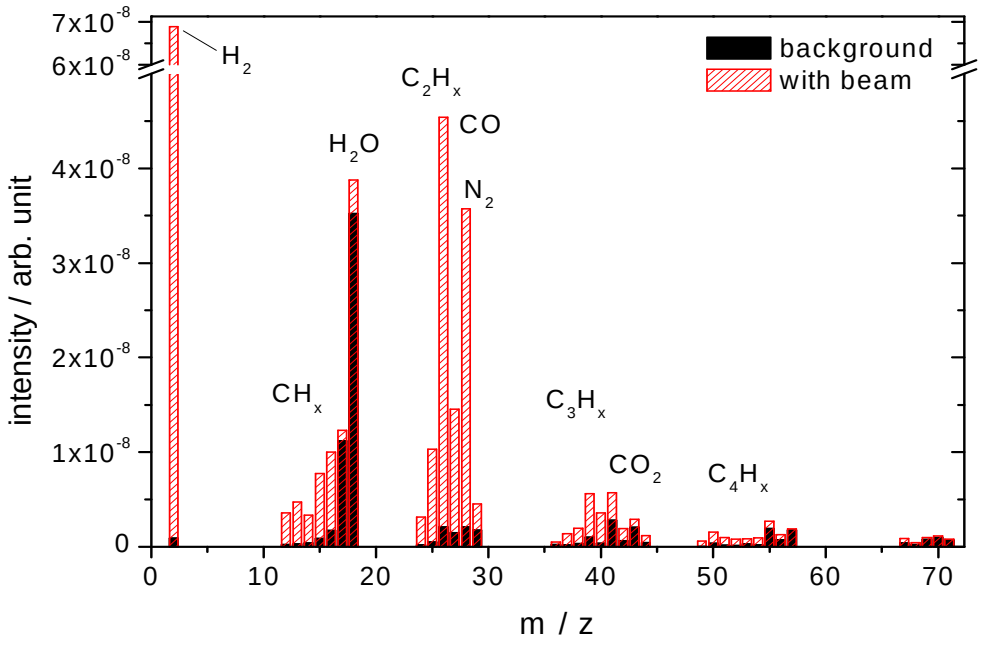

Fig. 5.34 Mass spectra of 10 μm thick amine cured polyepoxy irradiated with 4.5 MeV/u Au-ions

G11-type GFRP:

Samples of G11-type polyepoxy were irradiated with a Ca beam and an energy of 5 MeV/u at the GANIL in France as described in [58]. Compared to the RGA spectra of the amine cured polyepoxy matrix during Au irradiation, the G11 composite irradiated with Ca ions shows significant differences (Fig. 5.35). Despite hydrogen (H_2, m/z=2) still being the dominating outgassing degradation product, mainly water and carbon monoxide become noticeable in greater amounts relative to other outgassing species. Hydrocarbon fragments are not detectable significantly. An explanation of this can be found both in the lower energy loss of the used Ca-beam, and in the smaller volume of outgassing polymers material due to the composites mixture of 60 % glass fibers. It is difficult to draw conclusions and/or a true comparison to the Au irradiation of the amine cured polymer because of the different ion-beam as well as the different experimental chambers (chamber vacuum, pumps, ect.). Experiments with both types of material would have been necessary. Due to limited beam time it was not possible to conduct this type of experiment.

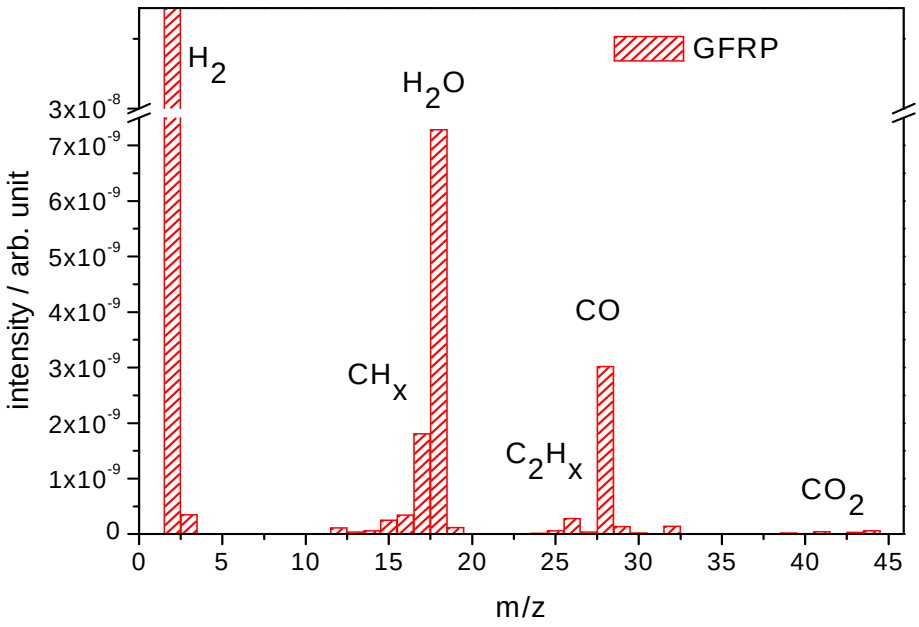

Fig. 5.35 Obtained mass spectrum of 5 MeV/u Ca-ion irradiated G11 after subtraction of the background (beam on holder without sample). The range of 5 MeV/u Ca ions in G11 is about 50 μm and therefore stopped in the 1 mm thick sample.

Degradation mechanism of polyepoxy and G11-type GFRP:

In summary, the ion induced changes of the chemical structure of G11-type polyepoxy is governed by the decomposition as indicated by outgassing of volatile combustion gases (mass loss) as well as decrease of band intensities of functional groups as detected by FT-IR. In the case of G11-type composite, only ex-situ measurements are available for the IR because of its thickness of about 1 mm. Besides the decrease of IR bands degradation products such as alkynes, carbon-carbon double bonds, and heterocummulenes (allenes) become visible in the in situ FT-IR measurements. The structure of amine cured polyepoxy is shown in Fig. 5.36, where the arrows indicate the 3D crosslinking of the material; i.e. continuous repetition of diglycidylether of bisphenol F and amine curing agent units. Possible degradation routes are presented in Fig. 5.37.

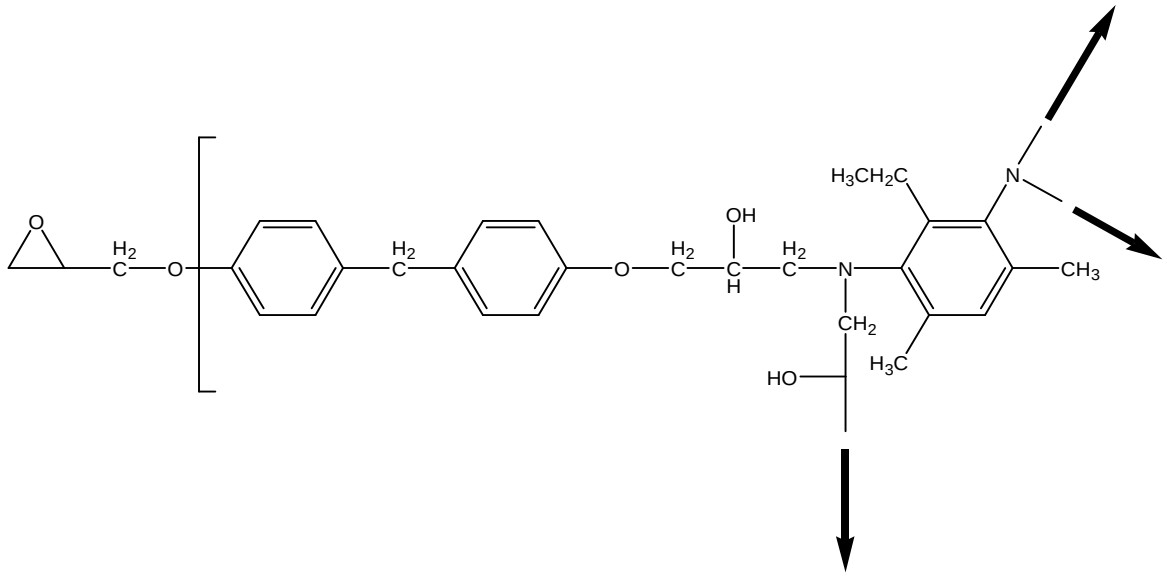

Fig. 5.36 Part of the repeating unit of amine cured polyepoxy used in this study. Arrows indicate the continuing of the structure which is cross-linked in great amount due to the amine curing.

Ion induced synthesis of alkyne formation

In literature the explanation of ion induced production of terminal alkynes is adopted from high temperature processes observed in the thermal degradation of aromatic molecules such as benzene, phenol, ect. [224]. Also, in PE, PVDF and PP alkyne-bands are identified too, but so far an explanation of their synthesis is missing [223]. In the latter reference the broadness of the alkyne bands of aromatic polymers is discussed. The FT-IR measurements of ion induced polyepoxy show the same tendency of forming rather broad alkyne-absorption band.

Despite the fact that polymers naturally show broad absorption bands, an adittional explanation for the broad alkine bands could be the existence of additionally –OH groups, because the CH-stretching of terminal alkynes in molecules additionally bearing –OH are found to be broad (see appendix). Fig. 5.37 A) shows the proposed ion induced production of butadiine and a ketenale from ion irradiated polyimide as described in Ref. [224]. The intermediate step of observed degradation products (in case of in-situ FT-IR gas analysis) already shows a subunit containing a terminal alkyne. It would therefore be a reasonable degradation path for amine cured polyepoxy as they bear similar structural units.
Another possible formation pathway can be drawn from the industrial synthesis of acetylenes which is performed using CH_4 pyrolysis at 1500°C with short contact times. An ion induced thermal spike would produce similar conditions: high temperatures and short contact times. For hydrocarbons which have a greater carbon content than CH_4, alkynes, or better polyynes, are the typical intermediate products for carbon char or soot synthesis [225]–[227]. Since carbon cluster synthesis is commonly observed in ion induced polymer degradation (as discussed in chapter 5.1 for polyimide degradation), an adoption of this mechanism would explain both carbon cluster production as well as alkyne production. In principle, the energies introduced into the material are high enough to break all bonds within a track. Therefore exotic degradation products as in case of high temperature synthesis are expected. However, the exact mechanism of the nature of alkyne formation is considered to be a mixture of the mentioned different degradation processes. Again it should be pointed out that ion induced polymer degradation follows thermal degradation pathways rather than photochemical processes.

Ion induced synthesis of allenes

Heterocummulenes and allenes are sensitive molecules usually synthesized at high temperatures, for example from malonic esters and their derivatives [228], or acetic anhydride [229]. At ambient conditions they tend to form ring structures or to polymerize. Therefore, the observation of this degradation path becomes only visible in the used in-situ IR spectroscopy set-up. Earlier investigations using ex-situ IR spectroscopy on cured polyepoxy samples did not reveal the band at 1942 cm^{-1} [230]. The band at 1942 cm^{-1} is most likely an allene not having a ketenal- or isocyanide-type structure, because cumulated double bonds which include oxygen or nitrogen atoms are found at higher wavenumbers (as the band found at 2200 cm^{-1}). One idea of a degradation pathway which ends in an allene is

proposed in Fig. 5.37 C). The proposed formation includes water and hydrogen abstraction, both identified outgassing degradation products in the experiments.

Ion induced synthesis of carbonyls and carbon-carbon double bonds

The degradation pathways which end up in carbon-carbon double bonds are dehydrogenations and discussed widely discussed in literature [78], [231], [232]. In the same manner carbonyls are found in polymers containing oxygen such as PC, PVAc and others [196], [224], [233]. Both structural groups, being identified in the IR spectra, are therefore expected degradation products and not discussed further. It can be stated that cured polyepoxy polymers show similar degradation tendencies to form carbon-carbon and carbon-oxygen double bonds like other polymers.

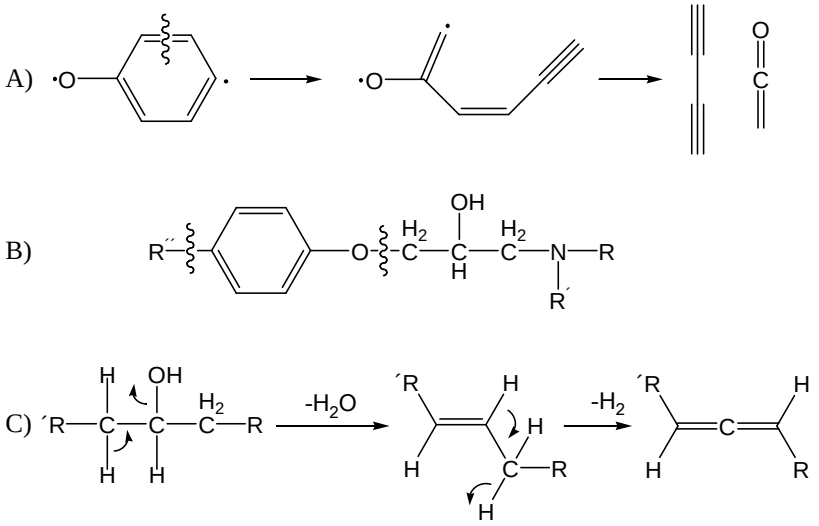

Fig. 5.37 Discussed degradation pathways A) synthesis of terminal alkynes as described in [184], [185] B) possible bonds which after degradation create the phenol radical of A) C) mechanistic degradation pathway which forms allenes

Changes in FAIR-relevant material properties of irradiated glass-fiber reinforced plastics

Dielectric strength of glass-fiber reinforced plastics (GFRPs)

Microscopic observations

In all cases, the ion irradiation induced coloration of GFRP as well as cyanatester/S-glass composites. The color of the polymer matrix, initially green in the case of G11, becomes dark brown. Additional features become visible under the light microscope. Cracks and delaminated areas show up within the irradiated zone (Fig. 5.38). Delamination of the fibers with the matrix interface was reported to appear in the case of gamma irradiated glass-fiber/composites and is a strong indicator for loss of material performance [234]. These eroded areas were found for all samples of the amine cured polyepoxy system and the cyanatester epoxy mix (not presented).

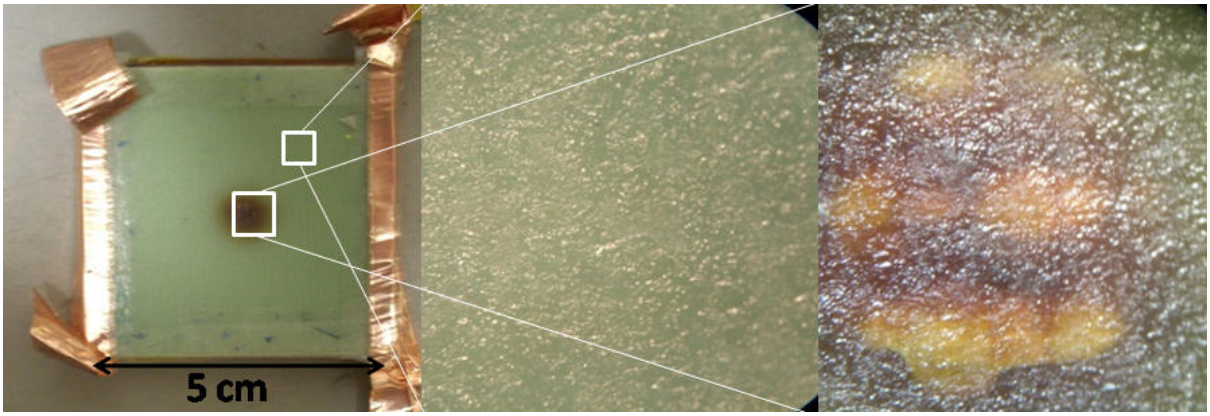

Fig. 5.38 left: G11-type GFRP sample stack irradiated with a total fluence of 1e12 cm^{-2} xenon ions of 200 MeV/u. center & right) Magnified areas of non-irradiated and irradiated samples showing cracks and delamination

Breakdown voltage measurements of G11-type polyepoxy/glass-fiber composite (DC)

The data of breakdown voltage measurements using a DC voltage ramping are presented in Fig. 5.39 and represent average values and standard deviation of three measurements. In the low fluence regime (up to 1×10^{11} cm^{-2}) no significant change of dielectric strength is found. A small increase might be anticipated. But, considering the low statistics in the case of irradiated samples, the overall effects are within the calculated standard deviations. At higher

fluences the dielectric strength dramatically decreases due to degradation of the material. At the highest fluence of 1.2×10^{12} cm^{-2} (corresponding to 2.3 MGy) the material has lost more than half of its dielectric strength.

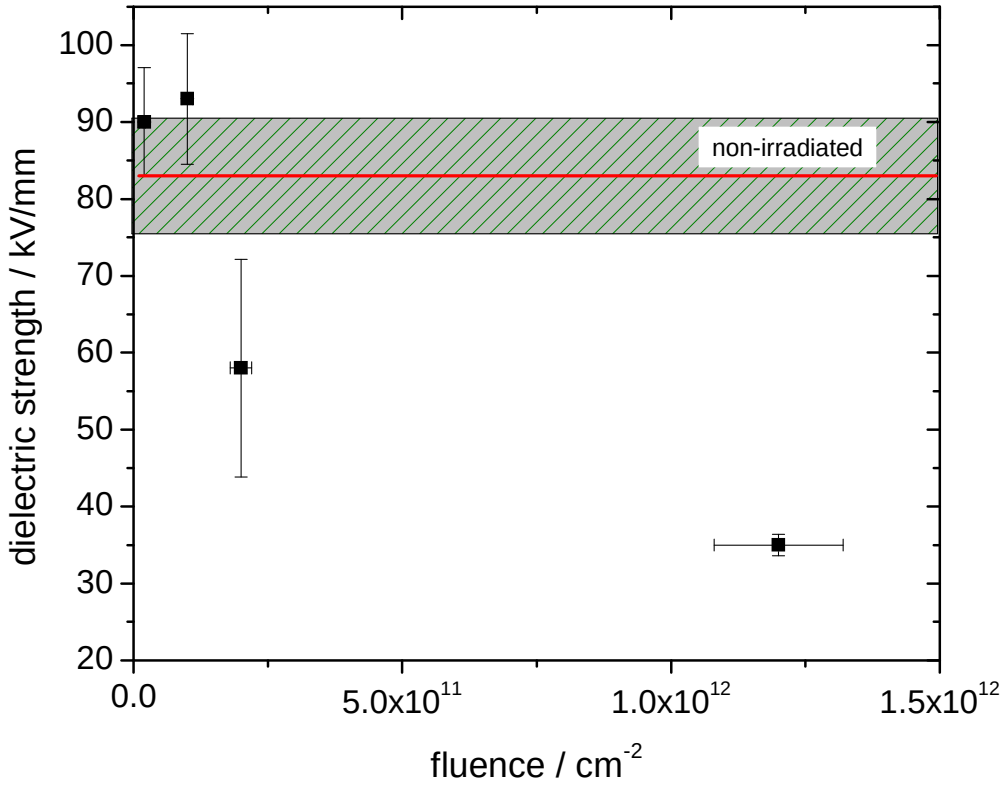

Fig. 5.39 DC-dielectric strength of G11-type GFRP versus fluence of 200 MeV/u Xe-ions. Error bars are by means of standard deviation of three measurements.

Breakdown voltage measurements of G11-type polyepoxy and cyanatester-epoxy glass-fiber composite (AC)

The (AC)-dielectric strength of non-irradiated and irradiated glass-fiber reinforced plastics is plotted as a function of irradiation fluence in Fig. 5.40. For the non-irradiated materials it can be stated that (i) the material shows a lower dielectric strength compared to DC measurements (as discussed in the introduction) and (ii) that the initial dielectric strength of the cyanatester-epoxy blend/S-glass system is lower than in the case of the commercial epoxy system. The latter finding might be explained by the pilot-plant production process of the cyanatester system, which was apparently not optimized, and sample pieces showed imperfections at the surface already in the non-irradiated state.

For irradiated samples, two different degradation behaviors are observed. In the case of classical G11-type composite the dielectric strength decreases in a kind of exponential decay evolving to a limiting value of about 32 kV/mm (Fig. 5.40).

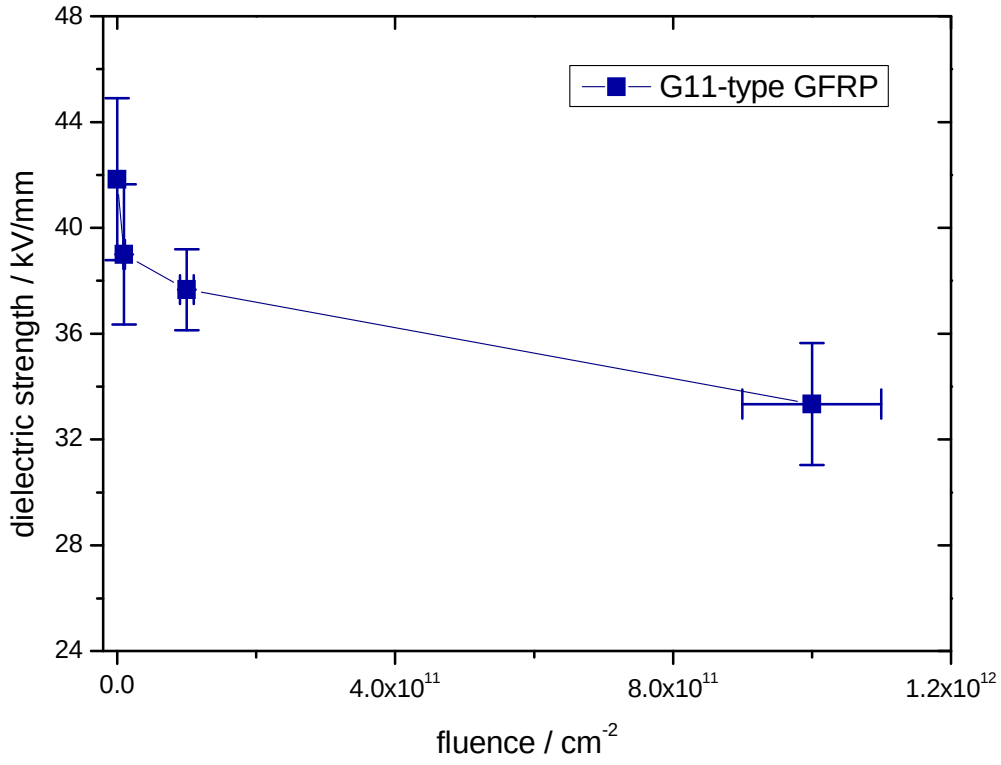

Fig. 5.40 AC-dielectric strength of G11 type GFRP versus fluence of 400 MeV/u Au-ions. Lines are guides to the eye only.

In contrast to this, the cyanatester-epoxy/S-glass composite does not show any degradation in dielectric strength (Fig. 5.41). Within the experimental error the dielectric strength value scatters around 20-30 kV/mm. The reason for this behavior is to be found in the higher radiation resistance of cyanatester (as observed in gamma and neutron irradiation studies) as well as the higher strength of the S-glass fibers.

The classical and commercially available system, even so degraded, shows a higher dielectric strength after irradiation. The question remains open-ended as to whether the radiation resistance would still be higher in the case of an optimized synthesis procedure of cyanatester-epoxy/S-glass composites.

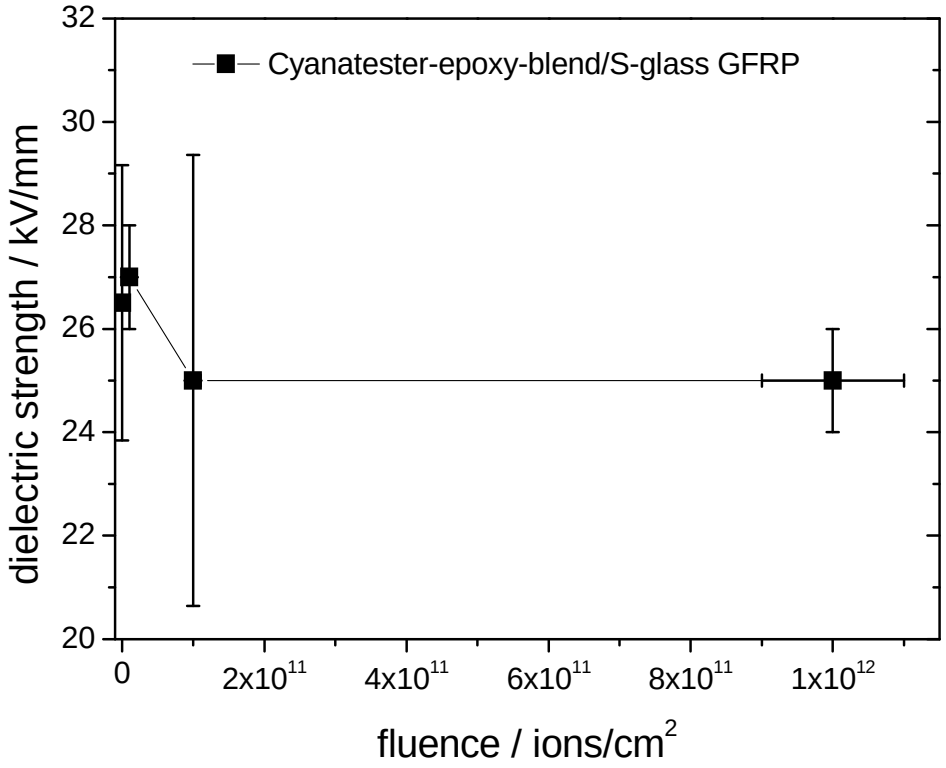

Fig. 5.41 AC-dielectric strength of cyanatester-epoxy/fiber composite versus fluence of 400 MeV/u Au-ions. Lines are guides to the eye only.

SEM

After dielectric strength measurement breakdown holes within the ion beam eroded area become visible. These areas were analyzed by means of scanning electron microscopy as presented in Fig. 5.42, exemplary on the G11 sample tested under DC conditions irradiated with 1.2×10^{12} cm^{-2} of xenon-ions (2.3 MGy). The breakdown causes the creation of a large hole, where the epoxy matrix is completely pulled out, surrounded by a less damaged zone. Higher magnification of the damaged zone reveals that the matrix partly is not bonded to the fiber anymore, which indicates an degraded fiber-matrix interface.

In disagreement with [36], we did not observe any changes of the breakdown holes with increasing irradiation dose. Different samples show no clear trend in growing damage zone or form of breakdown holes and are therefore not presented.

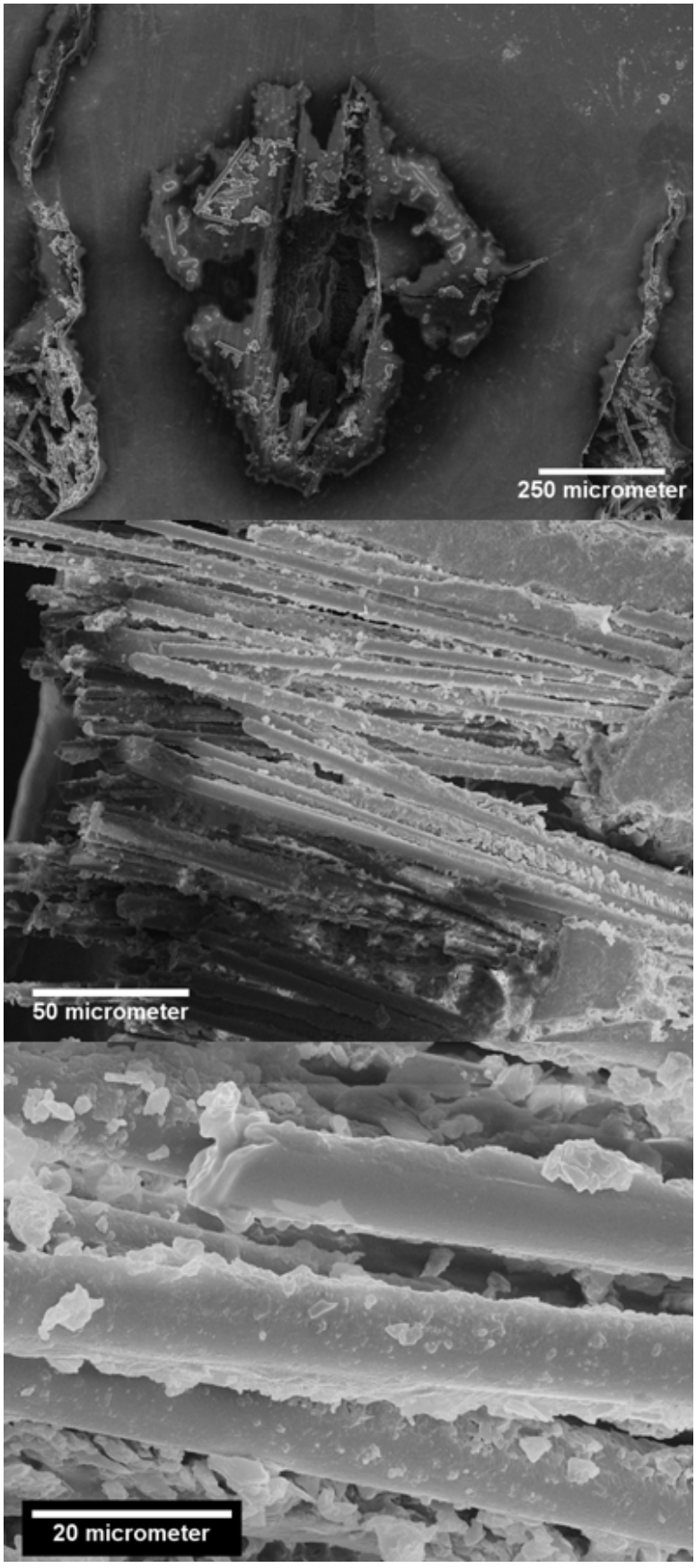

Fig. 5.42 Top view (SEM images) of breakdown voltage hole of irradiated epoxy/fiber composite with a special focus on the fiber-matrix interface.

Low temperature thermal conductivity and specific heat of G11

Thermal conductivity

Fig. 5.43 shows the low temperature thermal conductivity of G11-type glass-fiber reinforced polyepoxy. Since the material consists of two dimensional woven glass fabrics embedded in a polyepoxy matrix, it is anisotropic in nature. Therefore the thermal transport was measured in fiber- and "through thickness"- (warp-) direction.

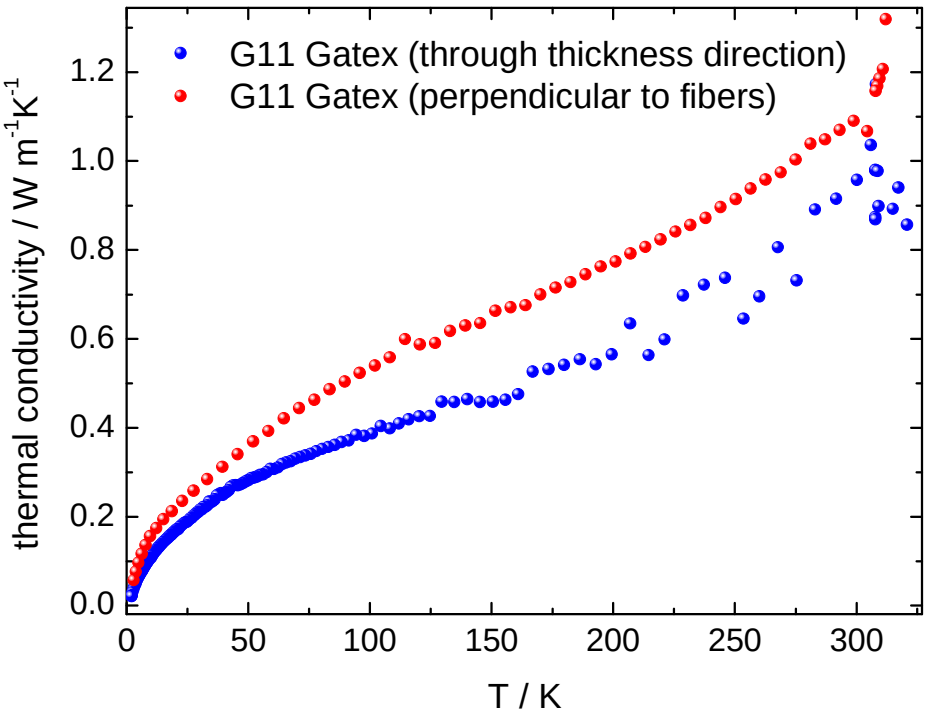

Fig. 5.43 Thermal conductivity versus temperature of G11-type GFRP for different directions of the composite

In the fiber direction the thermal conductivity is 30 % higher within the analyzed temperature regime. Glass-fibers such as the E-glass used in this composite is known to have a higher thermal conductivity compared to polymers such as cured polyepoxy. The results are therefore within the expectations that in warp direction a higher thermal conductivity is found [235]. Unfortunately, no appropriate irradiated samples were available to check the difference of irradiated and non-irradiated composites. However, the non-irradiated data is useful for the superconducting magnet design to simulate the quench behavior of the superconducting coil which is dependent on the heat capacity and the thermal conductivities of the used materials. Although much literature on low temperature thermal conductivity of

G11-type composites is available [118], [99], [236], [237]; the thermal conductivity of this specific type of material has been measured for the first time.

Specific heat

The low temperature volumetric specific heat of non-irradiated G11-type composite is presented in Fig. 5.44 in comparison with data of other glass-fiber reinforced plastics, taken from literature [235], [238], [239], [240], [241], [242].

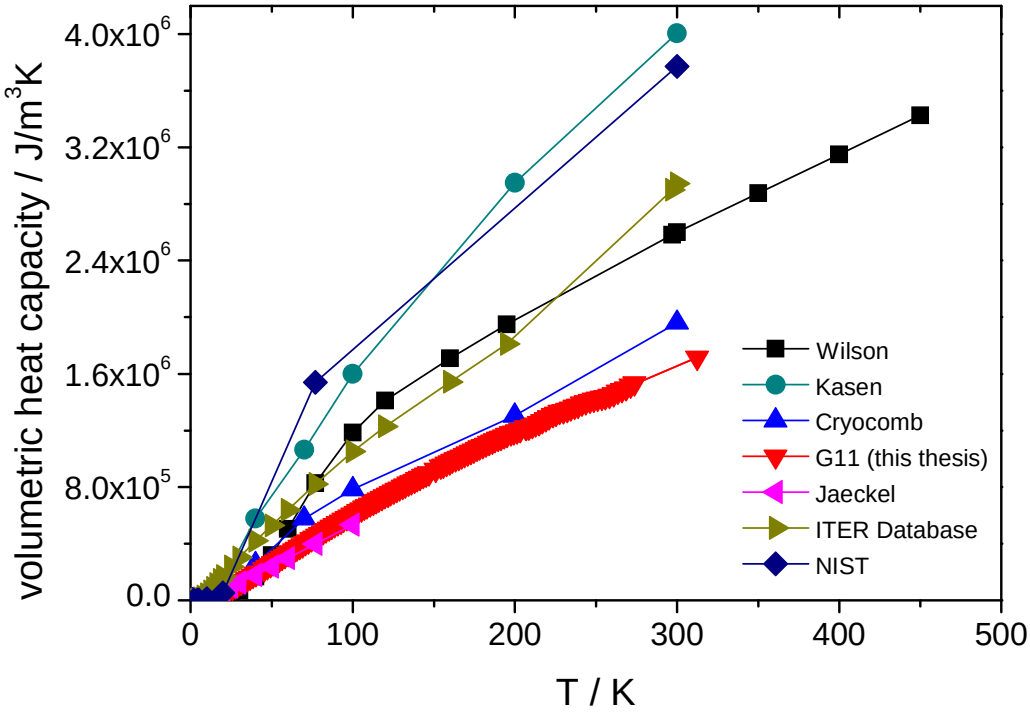

Fig. 5.44 Volumetric specific heat of various G11-type GFRP´s versus temperature

In comparison to the found volumetric specific heat of other G11-type composites, the Gatex material used in this study has a low volumetric specific heat. In Fig. 5.45 the specific heat capacity (per mass) is presented for non-irradiated material. Within the expected instrumental error of about 5 % no significant change in C_P is found. The reason for this is the low energy loss of the used particle beam as well as the high glass fiber content (50-60 %) of the material. If we expect the polyepoxy matrix to behave like polyimide and consider the glass fiber unchanged in the observed dose regime, then this behavior is very well explained.

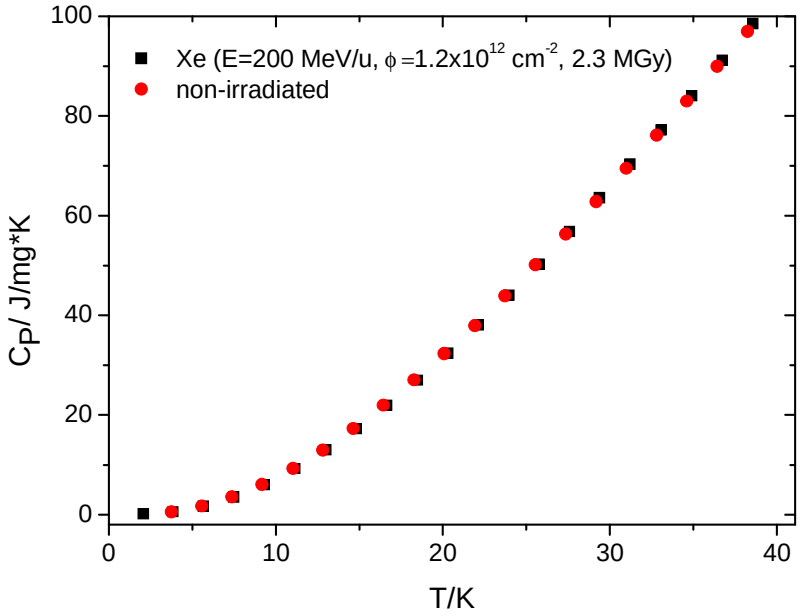

Fig. 5.45 Comparison between the heat capacity of non-irradiated and 200 MeV/u Xe-ion irradiated G11-type GFRP

Conclusion about ion induced material property changes of glass fiber reinforced plastics

In comparison to the ion induced degradation of thin polymer insulators, the effects on material properties of high energy heavy ion irradiated G11-type glass-fiber reinforced plastics are less dramatic. The reason for this is ascribed to (i) the lower energy loss of high energy particles, which is 2.5 keV/nm for 200 MeV/u xenon ions compared to 10.5 keV/nm for 11 MeV/u xenon ions and (ii) from the inorganic part of the composite (i.e. glass-fibers) which also reinforce the composite against radiation because of the higher radiation resistance. The relative change in dielectric strength of irradiated cyanatester/S-glass composites is found to be less sensitive compared to classical G11 epoxy/E-glass systems. However, the classical system initially has a higher dielectric strength. The turns of the superconducting coil of the SIS 100 FAIR magnets will be insulated with about 75 μm of polyimide reinforced with G11 (about 0.2 mm between each turn) and have to survive a security limit of 5 kV. From our tests it can be concluded that without further degradation by electrical and thermal cycling, and/or pulsed mechanical forces, the used insulation fulfill the specifications of the FAIR magnet design. However, the mentioned factors cannot be neglected, and have to be tested to give a true lifetime estimation. Also, more statistics could

deliver useful information about true failure probabilities. Due to the limited beamtime available, high doses as well as a great number of samples are typically not available.

Changes of thermal properties at low temperature of the G11 were tested and the volumetric heat capacity of irradiated G11 samples was found to be unchanged after an irradiation dose of 2.3 MGy of 200 MeV/u xenon ions. This means that the quench performance of the superconducting coil will not change due to a change in volumetric heat capacity at the analyzed dose.

5.3 Functional Tests on Irradiated Accelerator Components

Leak Test on Irradiated Voltage Breaker

The voltage breaker decouples magnets from each other from an electrical point of view, but its main function is the transport of liquid helium (as described in the introduction) in a circuit of many magnets. Considering the high mobility of helium atoms in the gaseous or liquid state, it is imperative that the voltage breaker guarantees leak tightness. Remembering the accident at CERN in 2010, the safety of the cryogenic system is of major concern.

The specification of the FAIR magnet design gives a leakage rate of $<10^{-7}$ Pa/l*s as tolerable (inner pressure 2.5×10^{6} Pa, room temperature). Prior to the irradiation, the non-irradiated voltage breaker was submitted to inner helium pressure of 30 bars and 5 times cycled (thermally) from 300 K to 77 K by liquid nitrogen. After this procedure the leakage rate was determined with a vacuum tester and found to be 10^{-9} Pa/l*s, two orders of magnitude better than specified. After irradiation (as described in 4.4), the voltage breakers insulation, impregnated G11, suffered from strong coloration due to the ion irradiation (Fig. 5.46). It was submitted to 2.5×10^{6} Pa of inner helium pressure and 1 time cycled to 77 K. After this (moderate) procedure the leakage rate increased to 5×10^{-3} Pa/l*s.

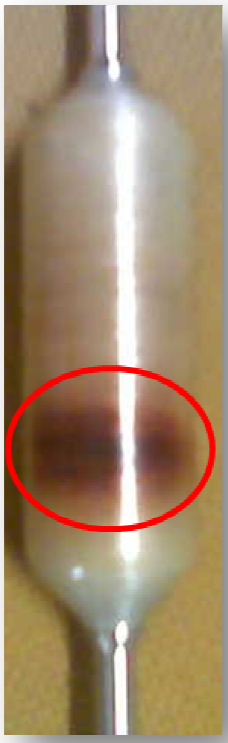

Fig. 5.46 Photograph of irradiated voltage breaker showing ion induced coloration

Table 5.6 Helium leakage rate of non-irradiated and irradiated voltage breaker

Fluence / cm^{-2}	Leakage rate / (Pa/l*s)
Pristine	1×10^{-9}
3×10^{13} Ar-ions (400 MeV/u, 0.630 MGy)	5×10^{-3}

The conclusion of this experiment is that ~1 MGy of Ar-beam is not tolerable for the application. As a consequence of this result, the magnet design plans to shield the voltage breaker from irradiation via a stainless steel shield, or replace it with ceramic voltage breakers. The latter voltage breakers are successfully used in the LHC of the CERN, leak tight without a polymeric impregnation, and expected to be more radiation resistant.

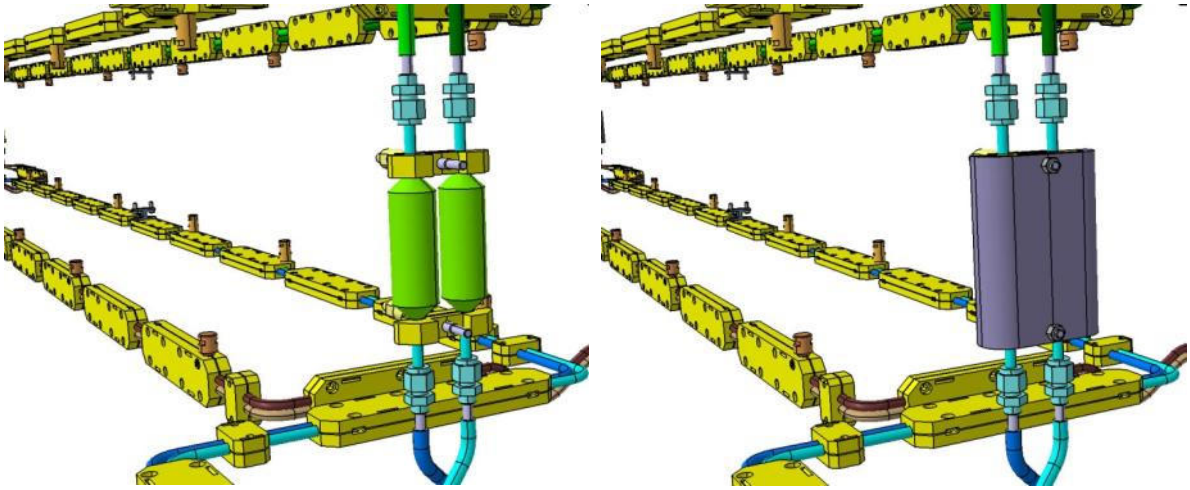

Fig. 5.47 Technical drawing of the liquid helium transport tubes (left) and with the proposed steel shielding of the G11-type voltage breaker (right)

Temperature Sensors

In order to investigate the radiation hardness of Cernox™-Temperature Sensors (described in chapter 1.3), 5 sensors were irradiated with an secondary beam produced by stopping 1 GeV/u uranium beam in a stainless steel target, as described in chapter 4.3. Sensors were calibrated with a reference sensor before irradiation and cooled down after the irradiation together with the reference. The results of the temperature measurements and the relative error in percentage of each sensor versus the temperature are shown in Fig. 5.49. The beam induced error in temperature is always smaller than 2.5 %. This means in absolute temperature that the error is more pronounced in the high temperature regime above 100 K, where the sensors also initially have a higher uncertainty. The reason for this is due to the high resistivity of Cernox™-Sensors at low temperatures (which assures exact temperature measurements). Therefore low temperature measurements are more precise.

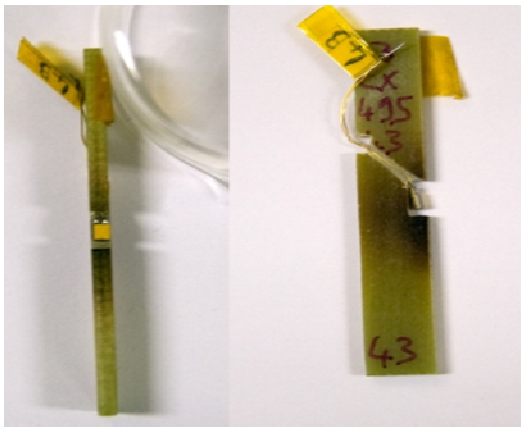

Fig. 5.48 Photographs of the irradiated sensor and its target holder made out of G11. Note the ion induced black coloration at the height of the beam spot.

Table 5.7 Dose of irradiated Cernox^{TM}-sensors

Sensor	Dose / MGy
reference	0
S1	2.7
S2	5.2
S3	6.1
S4	3.2
S5	0.1

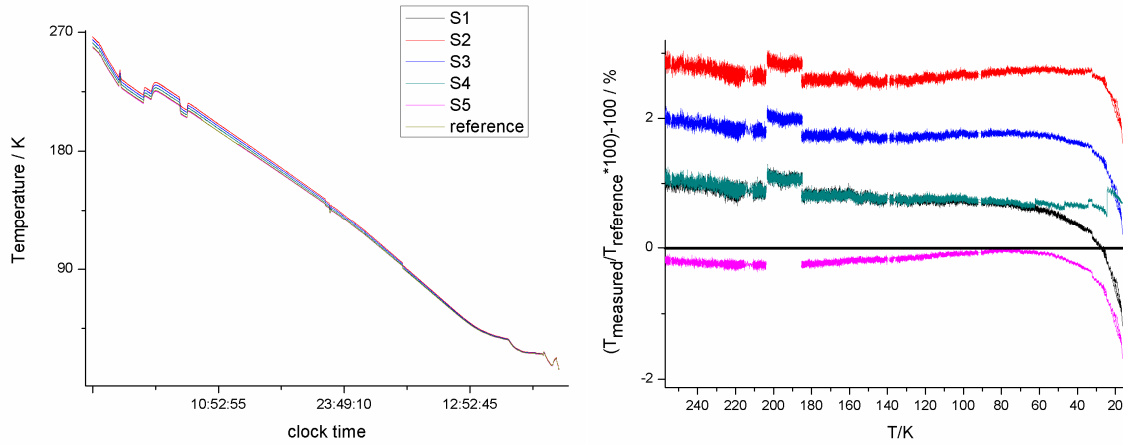

Fig. 5.49 Temperature versus cooling time of the 5 irradiated sensors and the non-irradiated reference sensor (left) and the calculated difference of the irradiated sensors against the reference sensor in %

Cernox^{TM}-Sensors are thin film metal oxide sensors which are based on electrical resistivity measurements. It is known that the resistivity of materials can be increased or decreased by irradiation and that metal oxides are quite radiation hard materials. So far, testing of radiation hardness of temperature sensors was exclusively done using gamma and neutron radiation for Cernox^{TM}, PtRh and carbon based sensors [243]–[247]. In our measurements these tests were expanded to a fragmented secondary beam consisting of gamma rays, neutrons and light and heavy particles as described in chapter 4.3.

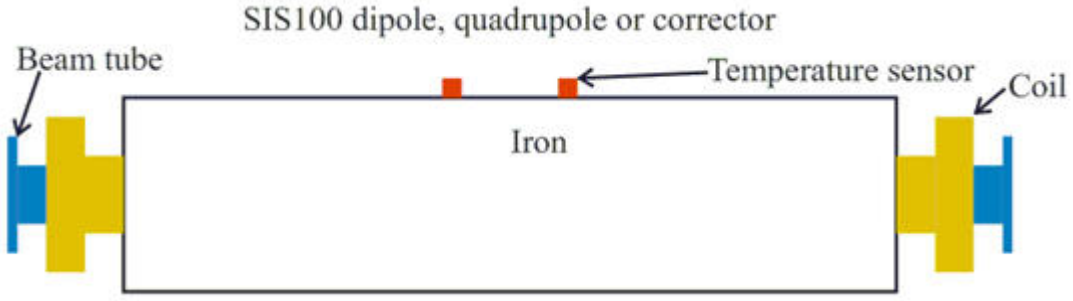

Fig. 5.50 Schematics of the beamtube and the vacuum chamber made out of stainless steel with position of the temperature sensors

Due to the planned position of the sensors on the outside of the later magnet (Fig. 5.50), they will be exposed mainly to neutrons, and our test conditions can be seen as a worst case scenario. It is expected that during 20 years of operation these sensors will see less than 10 MGy of neutron irradiation. Comparing the results for neutron and gamma irradiation with our results leads to the conclusion, that at low temperatures (such as 4.2 K) the expected error due to radiation will be less than 0.5 K. This means no problems are expected within the estimated operation time of 20 years.

Pixeo Peel Test Samples

The results of Pixeo glued polyimide strips irradiated with 11 MeV/u carbon ions and fragmented beam (as described in chapter 4.3) are presented in Fig. 5.51. In the case of carbon ions, the peel strength increases with irradiation dose while the elongation to break decreases. This result is an indication for an increase in brittleness and hardness of the material which is in agreement with mechanical studies of other irradiated polymers [248], [249].

The results of the fragmented beam irradiated samples show a strong decrease in both peel strength and elongation to break. In Fig. 5.52 the test specimen of the highest dose of the fragmented beam irradiation is presented to show the strong coloration induced by the fragmented beam. The results of this special sample (irradiated with a dose of about 5 MGy) were not measurable because the sample fell apart while being clamped into the measuring device.

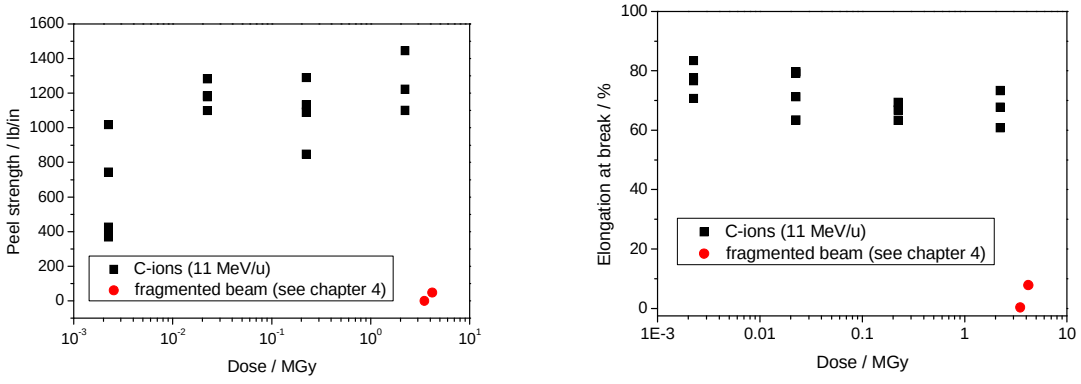

Fig. 5.51 Peel strength (left) and elongation at break (right) versus irradiation dose of Pixeo glued polyimide strips. Light ion irradiation (black squares) shows less effects compared with secondary radiation containing also heavy ions (red circles)

Even with the low statistic, heavier ions as present in the mixture of the fragmented beam experiment cause more damage compared to light ion irradiation within the analyzed fluence and energy regime. Furthermore, at 5 MGy induced by the secondaries of the fragmented

beam, the glued polyimide connection has lost its mechanical properties. Whether the radiation resistance of this glued connection fulfills the specification of the FAIR magnets should be carefully reconsidered. The part of the superconducting coil next to the beamtube will be exposed to a fragmented beam from one side which will result in a coil having intact and broken glued connections. This may not only affect the electrical insulation of the superconducting coil but also its quench behavior due to inhomogeneously altered materials, which may additionally contribute to friction induced heating during ramping of the magnet.

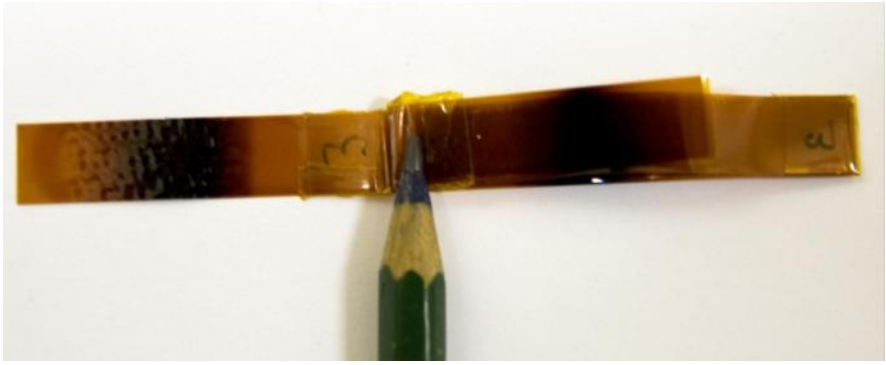

Fig. 5.52 Pixeo peel test specimen irradiated with about 5 MGy of secondary radiation as described in chapter 4. Note the radiation induced black coloration and the sample fell apart while being clamped into the measuring device.

For a reliable lifetime estimation additional tests are necessary. In the case of light ion irradiation the material is within the specification up to a dose of about 25 MGy.

6 Summary and Conclusions

This thesis deals with the characterization of radiation induced effects in polymers, polymer fiber composites and magnet components. A special focus lies in energetic heavy ion beam induced changes in the chemical structure and material properties of polymeric materials used in the future accelerator at the Facility for Antiproton and Ion Research (FAIR). For this reason, various irradiation experiments were conducted at the GSI Helmholtz Center for Heavy Ion Research, LMU Munich and the Institute for Theoretical and Experimental Physics (ITEP) and analyzed by means of various in-situ and ex-situ analytical methods, dielectric strength measurements, low temperature measurements of thermal properties, as well as technical tests of low-temperature sensors, voltage breakers and a special glued polyimide tape.

First in-situ experiments were performed at the new M3-Beamline of GSI. Polyimide as well as polyepoxy samples were irradiated with 4.5 MeV/u Au ions up to a fluence of 1×10^{12} cm^{-2} (~10 MGy) and their degradation was followed by means of in-situ FT-IR and on-line RGA. On the basis of these in-situ measurements, which revealed high sensitivity towards small changes in polymer structure, several degradation products could be identified. In polyimide four IR absorption bands in the regime of aliphatic $-CH_3$ and carboxylic -OH suggest that the heavy ions induce the formation of carboxylic acids and aliphatic branches such as methyl groups. For amine-cured polyepoxy samples alkynes, allenes and double bond formation are found as degradation products. Complimentary, ex-situ UV/Vis spectroscopy and TG-MS measurements demonstrated a great influence of the used type of radiation on the degradation mechanism. While particle beams lead to a carbonization of the material, gamma irradiation does not form any carboneous structures (within the observed dose regime). The applied high energy neutron irradiation does not show significant changes in polymer structure up to a neutron fluence of 2×10^{16} n/cm^2. An even higher neutron flux, necessary to create considerable modification, was not applied because of the high radioactivity such an experiment would create and the limited beamtime available.

In all cases, the measured induced changes are dependent on the energy loss of the used particle beams and therefore are sensitive towards their energy and atomic mass. In this context the dose is not anymore a suitable value to compare the degree of changes of different ion beams. A weighted unit (like an effective dose as used in biophysics) should be created or the fluence in combination with the dE/dx_{el} should be considered.

All material properties such as dielectric strength, thermal conductivity and volumetric specific heat at low temperatures suffer from ion induced degradation. The degree of changes

depends not only on the used particle beam but also on the measured material and the type of material property.

The dielectric strength of polyimide is found to be affected at rather low fluences (starting at 6×10^{6} cm^{-2}, for 11 MeV/u Au ions) where track percolation is not expected. At 1 MGy the insulating properties are at the limit of the specification. 21 MeV Proton irradiated polyimide samples still fulfill the electrical specification of the magnet at 82 MGy.

In measurements of samples irradiated under 45° of incident beam (11 MeV/u, Ru ions), the dielectric strength is dependent on the used angle of irradiation which indicates that the dielectric breakdown follows the ion tracks. Therefore single tracks already act as starting defects for breakdown events. It can be stated that heavy ions contributing to the secondary radiation in the later application are a serious security risk for the magnet insulation. Wherever possible an appropriate shielding should be foreseen or the insulation should be made of a different insulation system (such as MgO or mica-wrapped composites).

Glass-fiber reinforced plastics show less sensitivity against ion irradiation. The glass-fibers seem to protect the composite from continuous damaged zones showing only minor degradation in dielectric strength. Of the two different composites tested cyanatester-epoxy blend/S-glass-fiber composite has increased radiation hardness compared to classical G11-type composite. This result is in agreement with results of tests performed for ITER.

Thermal property measurements at low temperatures reveal that the thermal conductivity of polyimide decreases with increasing fluence of ion irradiation. However, the decrease is not of big technical concern. It is recommended that foreseen quench heaters should be designed more powerful to compensate this effect.

The tested impregnated voltage breaker suffers from tremendous degradation at already low dose. Leakage rates after irradiation are crucial and the usage is not recommended without appropriate shielding. Commercially available ceramic voltage breakers used at the LHC at CERN should have a higher radiation resistance and should be tested. Cernox™ temperature sensors showed a good performance. No strong radiation effects on the low temperature thermometry are expected. The polyimide strips glued with Pixeo™ are found to be sensitive against particle beams of high energy loss (similar to the dielectric strength or structural changes).

Because of the different degradation tendencies found for different material classes and properties it is recommended, from a technical point of view, to conduct more studies to analyze radiation induced changes of material properties, rather than following structural changes.

7 Outlook

Future investigations will focus on (i) measurements of test specimens irradiated to higher dose which were too radioactive to be measured so far (ii) static and dynamic mechanical tests of irradiated glass fiber reinforced plastics and (iii) testing of polymers such as Formvar™ and PVA used as insulators of accelerator components.

As mentioned in the introduction, all materials used in pulsed sc magnets will be exposed to dynamical mechanical forces at low temperature, due to Lorentzian forces and the pulsed operation of the magnet. Within the experiment described in chapter 4, various samples were irradiated for tensile, shear and compression tests. Due to the high induced radioactivity of this test specimen (mainly because of their higher mass and volume compared to the already tested materials), they could not be measured within the period of this thesis.

In Fig. 7.1 irradiated compression test samples of G11 are presented which show inhomogeneous damage induced by the ion beam, which are foreseen for dynamic compression tests at low temperature.

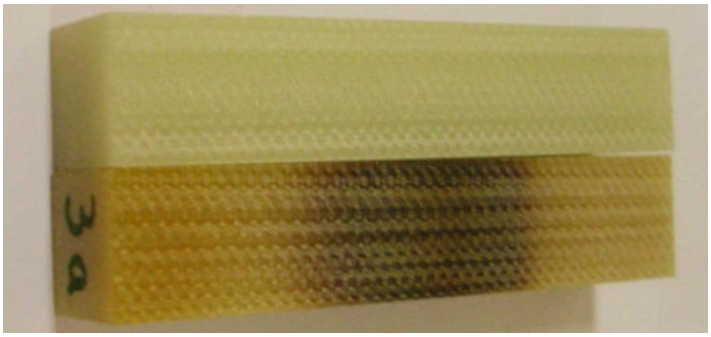

Fig. 7.1 Non-irradiated (top) and irradiated (fragmented beam, 6MGy) G11-type GFRP samples for compression tests (size: 1x1x5 cm).

Because of the inhomogeneous degradation there is the risk, that the degraded volume will act as weak link.

In Fig. 7.2, the residual radioactivity of this sample is shown as a function of time. Since no "hot cells" are available at GSI activated samples have to cool down to an appropriate level, commonly about 0.5 μSv/h. From the graph in Fig. 7.2 it can be anticipated that a tolerable residual radioactivity will be reached approximately by the end of 2014.

Besides polyimide also different types of vinyl-polymers such as polyvinyl alcohol (PVA), polyvinyl acetate (PVAc) and a mixture out of PVA/PVAc/polyvinyl acetal (Formvar™) are foreseen as wire enamels at various positions of the superconducting accelerator structure of FAIR. Such aliphatic polymers are known to show a lower radiation resistance compared

with aromatic polymers. Testing of these materials therefore has a high priority. The M-branch facility is used to investigate structural changes induced in such polymers and measurements on this field are ongoing [233].

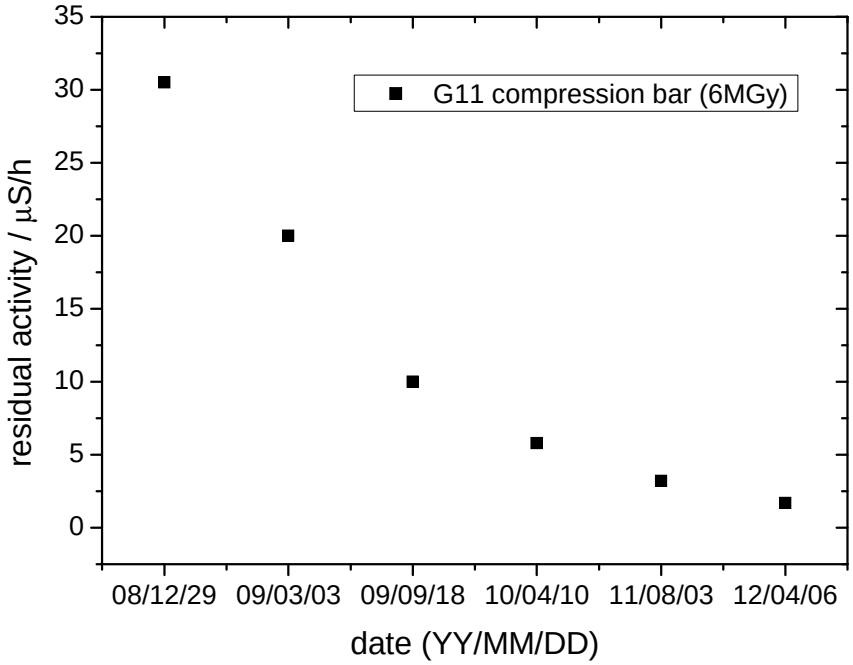

Fig. 7.2 Radioactivity of G11-type GFRP compression test specimen irradiated with 6 MGy of secondary radiation

Additionally, in 2009 a complete irradiation experiment was performed at the ITEP in Moscow. G11-type composites and pre-irradiated polyimide samples were irradiated with ~80 MGy of 21 MeV protons. At present, this samples are still too radioactive to be transported to Germany. Measurements of these samples will deliver interesting information such as dielectric strength comparisons of classical G11 and cyanatester/S-glass fiber composites. In addition they will expand the dose data of proton irradiated polyimides up to 160 MGy.

Appendix

IR spectra: Examples of Terminal Alkynes

All spectra are adopted from the spectral database of organic compounds (SDBS)
http://riodb01.ibase.aist.go.jp/sdbs/cgi-bin/direct_frame_top.cgi

1-Octyne

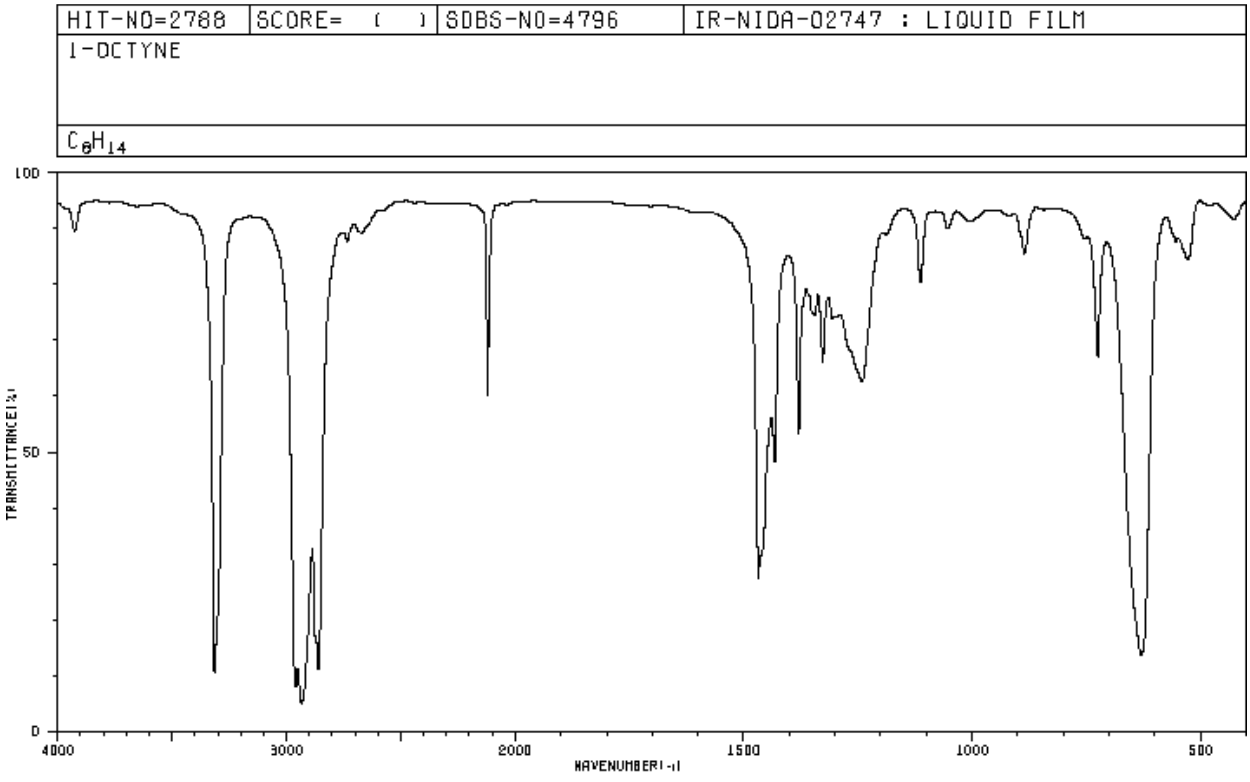

3926	86	2673	86	1327	64
3315	10	2120	58	1242	60
2959	7	1468	26	1113	77
2933	4	1461	30	886	81
2874	15	1432	46	725	64
2861	10	1380	52	630	13
2734	84	1346	72	628	81

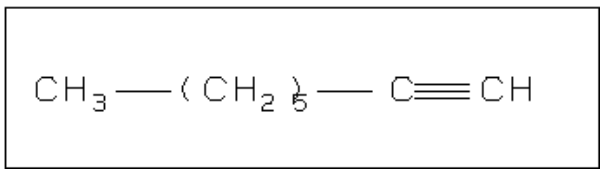

1-Tetradecyne

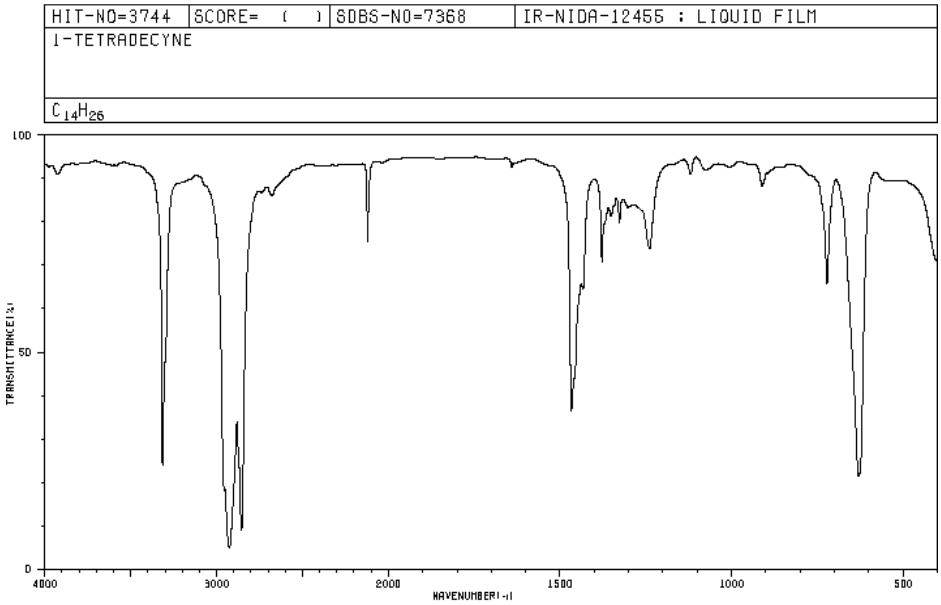

3315	23	1378	68	722	64
2926	4	1370	77	630	20
2855	8	1352	78		
2679	84	1327	77		
2121	72	1240	70		
1467	35	911	84		
1433	62	904	88		

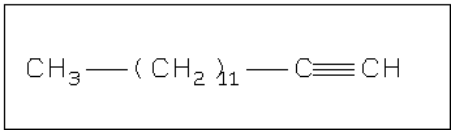

1-Dodecyne

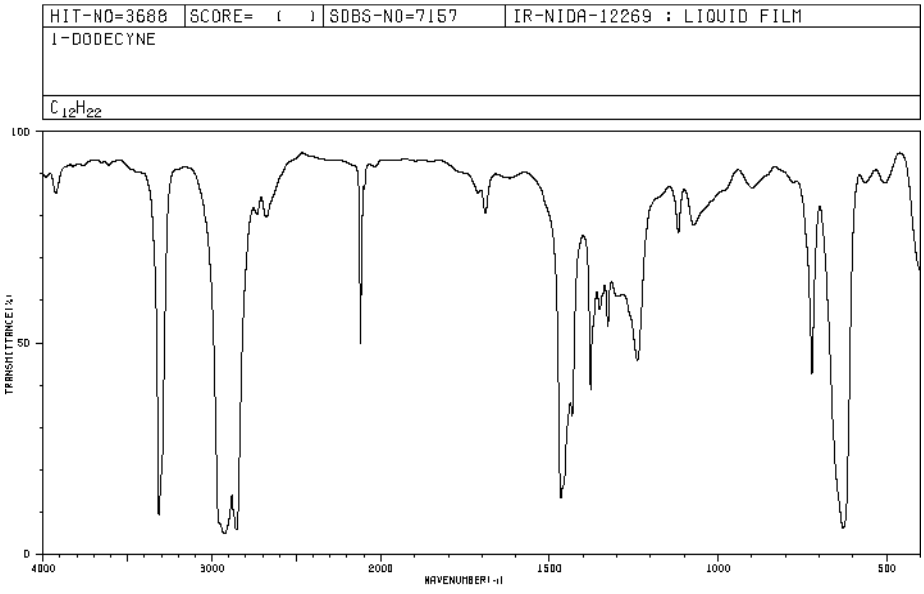

3926	81	2097	84	1327	62	664	84
3314	8	1703	84	1240	44	506	84
2927	4	1690	77	1117	72		
2857	6	1467	12	1072	74		
2734	77	1433	31	900	84		
2677	77	1378	37	722	41		
2121	47	1361	66	630	6		

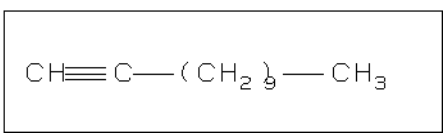

3-Butyn-1-OL

HIT-NO=829	SCORE= ( )	SDBS-NO=56	IR-NIDA-58849 : LIQUID FILM
3-BUTYN-1-OL			
C_4H_6O			

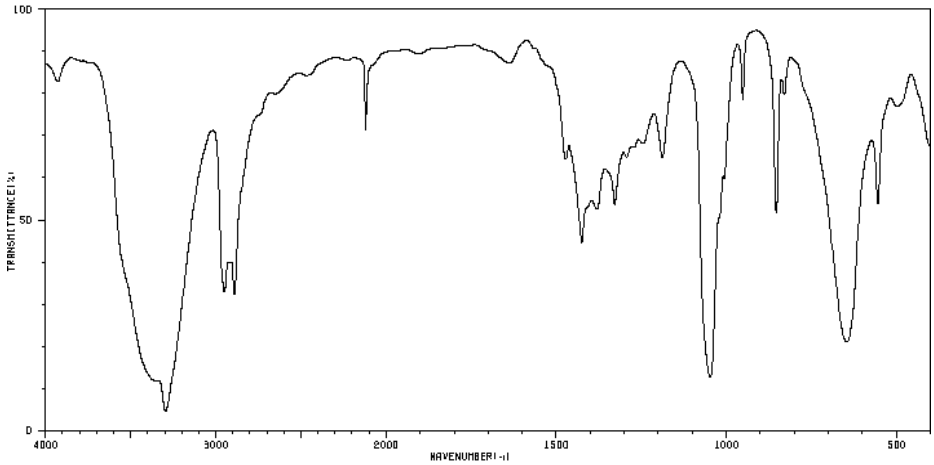

3929	79	1639	84	1047	12	494	74
3296	4	1472	82	952	77		
2950	32	1428	45	855	50		
2920	38	1381	60	830	77		
2890	32	1329	52	647	20		
2120	70	1293	62	555	52		
1645	84	1188	62	499	74		

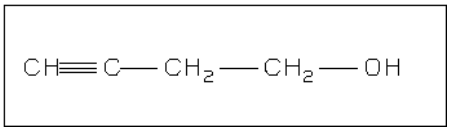

3.3-Dimethyl-1-Butyne

HIT-NO=6387	SCORE= ( )	SDBS-NO=22638	IR-NIDA-30148 : LIQUID FILM
3,3-DIMETHYL-1-BUTYNE			
C_6H_{10}			

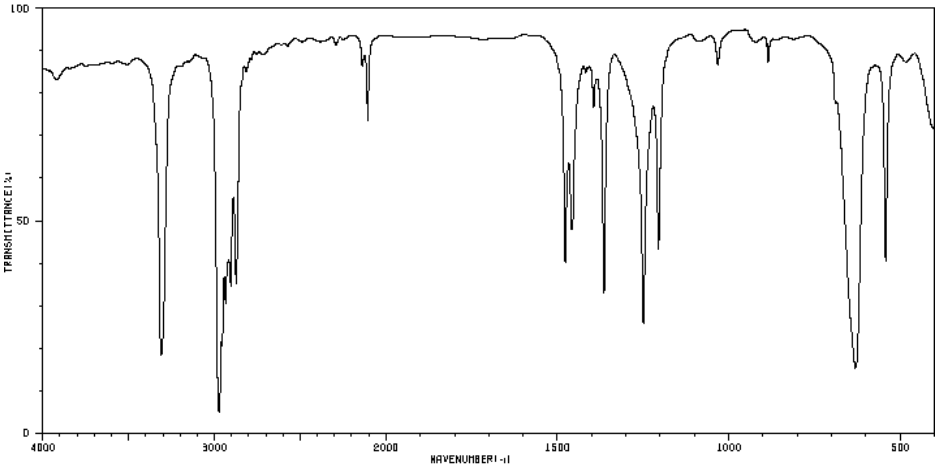

3920	79	2811	81	1364	32	483	84
3311	18	2138	84	1249	25		
2973	4	2108	70	1206	42		
2954	20	1477	38	1033	84		
2934	29	1457	46	885	84		
2904	33	1418	61	831	14		
2873	34	1396	74	643	39		

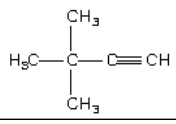

1-Phenyl-2Propyn-1-OL

HIT-NO=849	SCORE= ( )	SDBS-NO=87	IR-NIDA-10289 : LIQUID FILM

1-PHENYL-2-PROPYN-1-OL

C_9H_8O

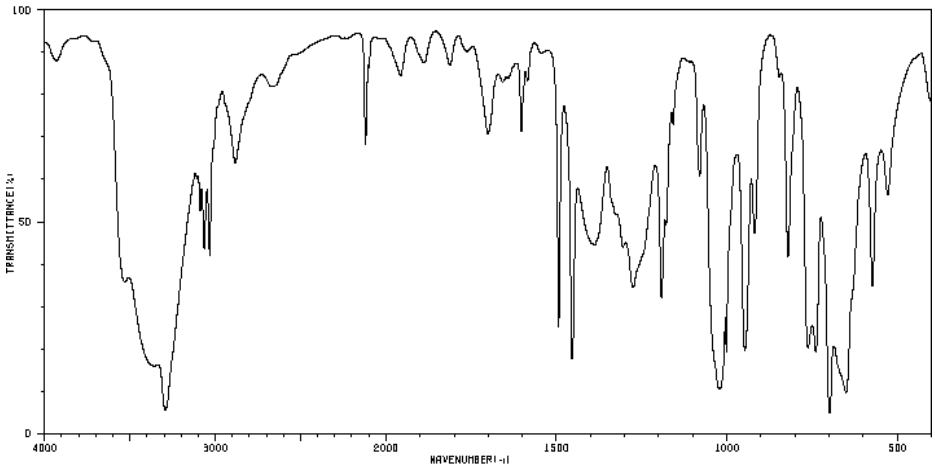

3292	5	2118	66	1494	24	1168	70	763	19
3088	50	1957	81	1455	17	1080	58	751	24
3065	42	1701	68	1388	43	1021	10	739	16
3039	41	1658	78	1305	42	1002	18	699	4
2883	62	1651	81	1276	33	947	18	651	9
2864	79	1603	68	1192	31	919	46	574	34
2864	79	1586	79	1179	47	821	41	528	53

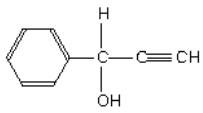

Phenylacetylene

HIT-NO=1445	SCORE= ( )	SDBS-NO=1444	IR-NIDA-63379 : LIQUID FILM

PHENYLACETYLENE

C_8H_6

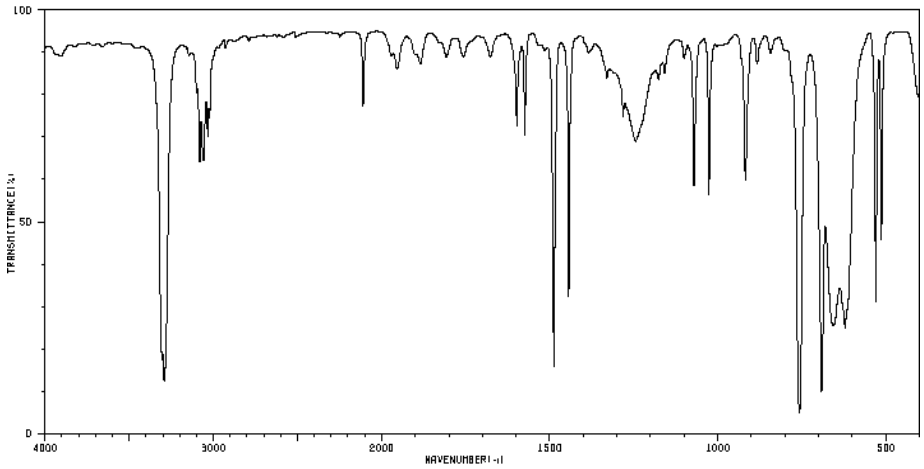

3906	86	2110	74	1674	68	1176	81	843	86
3306	16	1954	84	1488	15	1159	81	757	4
3291	12	1900	86	1444	31	1100	84	692	9
3081	62	1886	84	1386	86	1071	67	656	24
3058	62	1808	86	1331	81	1026	53	621	23
3034	68	1757	86	1282	72	918	57	530	30
3022	72	1598	70	1245	66	883	84	514	43

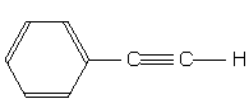

References

[1] I. Augustin, “Status of the FAIR project,” *Nuclear Instruments and Methods in Physics Research Section B: Beam Interactions with Materials and Atoms*, vol. 261, no. 1–2, pp. 1014–1017, Aug. 2007.

[2] P. Spiller and G. Franchetti, “The FAIR accelerator project at GSI,” *Nuclear Instruments and Methods in Physics Research Section A: Accelerators, Spectrometers, Detectors and Associated Equipment*, vol. 561, no. 2, pp. 305–309, Jun. 2006.

[3] W. F. Henning et al., “GSI Proposal,” *An International Accelerator Facility for Beams of Ions and Antiprotons*. [Online]. Available: http://www.gsi.de/GSI-Future/cdr/. [Accessed: 03-Aug-2011].

[4] “FAIR.” [Online]. Available: http://www.gsi.de/portrait/fair.html. [Accessed: 03-Aug-2011].

[5] W. F. Henning et al., “An International Accelerator Facility for Beams of Ions and Antyprotons-Conceptional Design Report.” [Online]. Available: http://www.gsi.de/GSI-Future/cdr/. [Accessed: 23-Aug-2011].

[6] L. Latycheva, N. Sobolevsky, G. Moritz, E. Mustafin, and G. Walter, “Radiation Damage to the Elements of the Nuclotron-Type Dipole of SIS100,” *Proceedings of the 9th European Particle Accelerator Conference*, 2004.

[7] E. Fischer, P. Shcherbakov, and R. Kurnyshov, “Finite element calculations on detailed 3D models for the superferric main magnets of the FAIR SIS100 synchrotron,” *Cryogenics*, vol. 47, no. 11–12, pp. 583–594, November.

[8] A. Kovalenko, N. Agapov, A. Alfeev, A. Bychkov, A. Gromov, A. Khodzhibagiyan, G. Kuztetsov, A. Shabunov, A. Starikov, E. Fischer, G. Moritz, and P. Spiller, “Full Size Prototype Magnets For Heavy Ion Superconducting Synchrotron SIS100 at GSI: Status of Manufactoring and Test at JINR.,” in *Proceedings of EPAC2008*, Genova, Italy, 2008, pp. 2443–2445.

[9] E. Fischer, Mierau, A., Schnizer, P., Schroeder, C., Bleile, A., Floch, E., Macavei, J., Stafiniak, A., Walter, F., Sikler, G., and Gaertner, W., “Fast Ramped Superferric Prototype Magnets of the FAIR Project — First Test Results and Design Update,” in *Proceedings of PAC09*, Vancouver, BC, Canada, 2009, vol. MO6PFP065, pp. 1–3.

[10] E. Fischer, A. Mierau, P. Schnizer, A. Bleile, W. Gartner, O. Guymenuk, H. Khodzhibagiyan, C. Schroeder, G. Sikler, and A. Stafiniak, “Thermodynamic Properties of Fast Ramped Superconducting Accelerator Magnets For the Fair Project,” *AIP Conf. Proc.*, vol. 1218, no. 1, pp. 989–996, Apr. 2010.

[11] M. Anerella et al., “The RHIC Magnet System for NIM,” BNL, Note (AM-MD-311), 15 2001.

[12] P. Komarek, “Materials for superconducting magnets,” *Journal of Nuclear Materials*, vol. 155–157, Part 1, no. 0, pp. 207–217, Jul. 1988.

[13] R. Denz, “Electronic Systems for the Protection of Superconducting Elements in the LHC,” *IEEE Transactions on Applied Superconductivity*, vol. 16, no. 2, pp. 1725–1728, Jun. 2006.

[14] K. Bauer, S. Fink, G. Friesinger, A. Ulbricht, and F. Wächner, “The electrical insulation system of a forced flow cooled superconducting (sc) magnet,” *Cryogenics*, vol. 38, no. 11, pp. 1123–1134, Nov. 1998.

[15] K. P. Jungst and H. Kronhardt, “Influence of discharge voltage on electrical arcing in magnet systems with short-circuits,” *IEEE Transactions on Magnetics*, vol. 28, no. 1, pp. 263–266, Jan. 1992.

[16] A. Ibarra and E. R. Hodgson, “The ITER project: the role of insulators,” *Nuclear Instruments and Methods in Physics Research Section B: Beam Interactions with Materials and Atoms*, vol. 218, no. 0, pp. 29–35, Jun. 2004.

[17] P.-H. Rebut, “ITER: the first experimental fusion reactor,” *Fusion Engineering and Design*, vol. 30, no. 1–2, pp. 85–118, May 1995.

[18] A. Newirkowez, “Untersuchungen zu durch Schwerionen-Bestrahlung induzierten Materialveränderungen in supraleitenden NbTi-Drähten,” PhD thesis,Technische Universität Darmstadt, Darmstadt, 2008.

[19] A. K. Bledzki, A. Kessler, G. Wacker, and H. Frenzel, “Einfluß der Faserbehandlung auf das Feuchteverhalten von glasfaserverstärkten Epoxidharzen,” *Angew. Makromol. Chem.*, vol. 260, no. 1, pp. 83–90, Nov. 1998.

[20] U. Riedel, “Konstruktionswerkstoffe aus nachwachsenden Rohstoffen,” Braunschweig, 2003.

[21] R&G Faserverbundwerkstoffe GmbH, “Glassfibers: Manufactore and Properties,” Waldenbuch, Manufactorer Datasheet.

[22] “Die Glasfaser.” [Online]. Available: http://www.pohris-fiber.de/html/body_die_glasfaser.html. [Accessed: 26-Sep-2011].

[23] G. Baschek and G. Hartwig, “Parameters influencing the thermal expansion of polymers and fibre composites,” *Cryogenics*, vol. 38, no. 1, pp. 99–103, Jan. 1998.

[24] S. Kanagaraj and S. Pattanayak, “Measurement of the thermal expansion of metal and FRPs,” *Cryogenics*, vol. 43, no. 7, pp. 399–424, Jul. 2003.

[25] O. Horn, “Kunststoff-Handbuch. Band 11. Polyacetale, Epoxidharze, fluorhaltige Polymerisate, Silicone usw. Herstellung, Eigenschaften, Verarbeitung und Anwendung. Herausgeg. von R. Vieweg, M. Reiher und H. Scheurlen. Carl Hanser Verlag, München 1971. 1. Aufl., XXII, 616 S., 362 Abb., 176 Tab., geb. DM 220.—,” *Angewandte Chemie*, vol. 84, no. 20, pp. 1000–1000, Oct. 1972.

[26] D. J. O’Brien and S. R. White, “Cure kinetics, gelation, and glass transition of a bisphenol F epoxide,” *Polymer Engineering & Science*, vol. 43, no. 4, pp. 863–874, Apr. 2003.

[27] H. Liu, A. Uhlherr, R. J. Varley, and M. K. Bannister, “Influence of substituents on the kinetics of epoxy/aromatic diamine resin systems,” *J. Polym. Sci. A Polym. Chem.*, vol. 42, no. 13, pp. 3143–3156, Jul. 2004.

[28] M. F. Grenier-Loustalot and C. Lartigau, “Molten state reactivity of difunctional cyanates: Thermal and spectroscopic studies by liquid and solid CP-MAS 13C-NMR,” *Journal of Polymer Science Part A: Polymer Chemistry*, vol. 35, no. 7, pp. 1245–1254, May 1997.

[29] W. A. Su and C. Chuang, “Effects of chemical structure changes on curing reactions and thermal properties of cyanate ester-cured rigid-rod epoxy resins,” *Journal of Applied Polymer Science*, vol. 85, no. 11, pp. 2419–2422, Sep. 2002.

[30] P. E. Fabian, J. A. Rice, N. A. Munshi, K. Humer, and H. W. Weber, “Novel radiation-resistant insulation systems for fusion magnets,” *Fusion Engineering and Design*, vol. 61–62, no. 0, pp. 795–799, Nov. 2002.

[31] S. W. Feucht, P. E. Fabian, and N. A. Munshi, “Development of novel radiation-resistant insulation systems for fusion magnets,” *IEEE Transactions on Applied Superconductivity*, vol. 13, no. 2, pp. 1516– 1519, Jun. 2003.

[32] K. Humer, K. Bittner-Rohrhofer, H. Fillunger, R. K. Maix, R. Prokopec, and H. W. Weber, “Innovative insulation systems for superconducting fusion magnets,” *Superconductor Science and Technology*, vol. 19, pp. S96–S101, Mar. 2006.

[33] M. W. Hooker, S. A. Arzberger, S. D. Grandlienard, M. W. Stewart, N. A. Munshi, G. M. Voss, R. D. Benson, and M. S. Madhukar, "Industrialization of Radiation-Resistant Cyanate Ester Magnet Insulation," *IEEE Transactions on Applied Superconductivity*, vol. 19, no. 3, pp. 2367–2370, Jun. 2009.
[34] M. Grenier-Loustalot, C. Lartigau, F. Metras, and P. Grenier, "Mechanism of thermal polymerization of cyanate ester systems: Chromatographic and spectroscopic studies," *Journal of Polymer Science Part A: Polymer Chemistry*, vol. 34, no. 14, pp. 2955–2966, Oct. 1996.
[35] J. B. Schutz, P. E. Fabian, C. S. Hazelton, T. S. Bauer-McDaniel, and R. P. Reed, "Effects of cryogenic irradiation on electrical strength of candidate ITER insulation materials," *Cryogenics*, vol. 35, no. 11, pp. 759–762, Nov. 1995.
[36] K. Humer, H. W. Weber, R. Hastik, H. Hauser, and H. Gerstenberg, "Dielectric strength, swelling and weight loss of the ITER Toroidal Field Model Coil insulation after low temperature reactor irradiation," *Cryogenics*, vol. 40, no. 4–5, pp. 295–301, April.
[37] J. B. Schutz, "Properties of composite materials for cryogenic applications," *Cryogenics*, vol. 38, no. 1, pp. 3–12, Jan. 1998.
[38] R. R. Coltman Jr. and C. E. Klabunde, "The strength of G-10CR and G-11CR epoxies after irradiation at 5 K by gamma rays," *Journal of Nuclear Materials*, vol. 113, no. 2–3, pp. 268–272, Jan. 1983.
[39] D. Evans and R. P. Reed, "Factors influencing the rate of gas evolution from epoxide resins during irradiation," *Advances in Cryogenic Engineering*, vol. 72 A, pp. 29–35, Jul. 1995.
[40] H. Bansemir and O. Haider, "Fibre composite structures for space applications: recent and future developments," *Cryogenics*, vol. 38, no. 1, pp. 51–59, Jan. 1998.
[41] S. Egusa, M. A. Kirk, R. C. Birtcher, and M. Hagiwara, "Neutron and gamma-ray irradiation effects in composite organic insulators," *Journal of Nuclear Materials*, vol. 133–134, no. 0, pp. 795–799, Aug. 1985.
[42] S. Egusa, M. A. Kirk, and R. C. Birtcher, "Neutron irradiation effects on the mechanical properties of organic composite materials," *Journal of Nuclear Materials*, vol. 126, no. 2, pp. 152–159, Oct. 1984.
[43] C. E. Klabunde and R. R. Coltman Jr., "Debonding of epoxy from glass in irradiated laminates," *Journal of Nuclear Materials*, vol. 117, no. 0, pp. 345–350, Jul. 1983.
[44] K. Humer, H. W. Weber, and E. K. Tschegg, "Radiation effects on insulators for superconducting fusion magnets," *Cryogenics*, vol. 35, no. 12, pp. 871–882, Dec. 1995.
[45] S. Egusa, M. A. Kirk, and R. C. Birtcher, "Effects of neutron irradiation on polymer matrix composites at 5 K and at room temperature: II. Degradation of mechanical properties," *Journal of Nuclear Materials*, vol. 148, no. 1, pp. 53–60, Mar. 1987.
[46] M. Mélot, Y. Ngono-Ravache, and E. Balanzat, "Role of the irradiation temperature on the modifications of swift-heavy-ion irradiated polyethylene," *Nuclear Instruments and Methods in Physics Research Section B: Beam Interactions with Materials and Atoms*, vol. 209, pp. 205–211, Aug. 2003.
[47] S. Egusa, K. Ishigure, and Y. Tabata, "Fast Neutron Irradiation Effects on Polymers. 1. Degradation of Poly(methyl methacrylate)," *Macromolecules*, vol. 12, no. 5, pp. 939–944, Oct. 2011.
[48] M. Krämer and M. Scholz, "Treatment planning for heavy-ion radiotherapy: calculation and optimization of biologically effective dose," *Physics in Medicine and Biology*, vol. 45, pp. 3319–3330, Nov. 2000.
[49] A. Meftah, F. Brisard, J. M. Costantini, M. Hage-Ali, J. P. Stoquert, F. Studer, and M. Toulemonde, "Swift heavy ions in magnetic insulators: A damage-cross-section velocity effect," *Phys. Rev. B*, vol. 48, no. 2, p. 920, Jul. 1993.
[50] J.-M. Costantini, J.-P. Salvetat, F. Couvreur, and S. Bouffard, "Carbonization of polyimide by swift heavy ion irradiations: Effects of stopping power and velocity," *Nuclear Instruments and Methods in Physics Research Section B: Beam Interactions with Materials and Atoms*, vol. 234, no. 4, pp. 458–466, Jul. 2005.
[51] M. K. Ghosh and K. L. Mittal, *Polyimides: Fundamentals and Applications*. New York: Marcel Dekker, Inc., 1996.
[52] C. E. Sroog, "Polyimides," *Journal of Polymer Science: Macromolecular Reviews*, vol. 11, no. 1, pp. 161–208, Jan. 1976.
[53] G. F. Hurley and R. R. Coltman Jr., "Organic materials for fusion reactor applications," *Journal of Nuclear Materials*, vol. 123, no. 1–3, pp. 1327–1337, May 1984.
[54] R. R. Coltman Jr. and C. E. Klabunde, "Mechanical strength of low-temperature-irradiated polyimides: A five-to-tenfold improvement in dose-resistance over epoxies," *Journal of Nuclear Materials*, vol. 103, no. 0, pp. 717–721, 1981.
[55] S. Takamura and T. Kato, "Effect of low temperature irradiation on insulators and other materials for superconducting magnets," *Journal of Nuclear Materials*, vol. 103, no. 0, pp. 729–733, 1981.
[56] R. H. Kernohan, C. J. Long, and R. R. Coltman Jr., "Cryogenic radiation effects on electric insulators," *Journal of Nuclear Materials*, vol. 85–86, Part 1, no. 0, pp. 379–383, Dec. 1979.
[57] D. J. T. Hill and J. L. Hopewell, "Effects of 3 MeV proton irradiation on the mechanical properties of polyimide films," *Radiation Physics and Chemistry*, vol. 48, no. 5, pp. 533–537, Nov. 1996.
[58] D. Severin, "Study of the degradation process of polyimide induced by high energetic ion irradiation," PhD thesis, Philipps University of Marburg, 2008.
[59] J.-P. Salvetat, J.-M. Costantini, F. Brisard, and L. Zuppiroli, "Onset and growth of conduction in polyimide Kapton induced by swift heavy-ion irradiation," *Phys. Rev. B*, vol. 55, no. 10, p. 6238, Mar. 1997.
[60] H. Schönbacher and M. Tevlet, "Report: Compilation of radiation hardness test data," CERN 89-10, 1989.
[61] Kar and R. G. Sharma, "Cryogenic Temperature Sensors," *Science*, vol. 57, no. 3, pp. 195–208, 2007.
[62] P. R. Swinehart, S. S. Courts, and D. S. Holmes, "Metal oxy-nitride resistance films and methods of making the same," U.S. Patent 536728522-Nov-1994.
[63] P. R. Swinehart, "Film resistors having trimmable electrodes," U.S. Patent 536308408-Nov-1994.
[64] S. S. Courts and P. R. Swinehart, "Review of Cernox™ (Zirconium Oxy-Nitride) Thin-Film Resistance Temperature Sensors," *AIP Conference Proceedings*, vol. 684, no. 1, pp. 393–398, Sep. 2003.
[65] Y. P. Filippov, V. M. Miklayev, and A. K. Sukhanova, "Irradiation of cryogenic temperature sensors by gamma dose of 1 MGy.," *Review of Scientific Instruments*, vol. 78, no. 4, p. 043502, 2007.
[66] H. W. Bonin, V. T. Bui, H. Pak, E. Poirier, and H. Harris, "Radiation effects on aluminum-epoxy adhesive joints," *Journal of Applied Polymer Science*, vol. 67, no. 1, pp. 37–47, 1998.
[67] L. Beskrovnaia, B. Florko, M. Paraipan, N. Sobolevsky, and G. Timoshenko, "Verification of Monte Carlo transport codes FLUKA, GEANT4 and SHIELD for radiation protection purposes at relativistic heavy ion accelerators," *Nuclear Instruments*

and Methods in Physics Research Section B: Beam Interactions with Materials and Atoms, vol. 266, no. 18, pp. 4058–4060, Sep. 2008.
[68] L. Latycheva and E. Mustafin, "Use of the Shield Code for Monte-Carlo simulation of the energy deposition and the fragmentation spectra in the elements of the SIS100 dipole magnet irradiated by 1GeV/u Uranium ions," GSI, Darmstadt, GSI-Acc-Note GSI-Acc-Note-2004-01-001, Jan. 2004.
[69] F. Bloch, "Zur Bremsung rasch bewegter Teilchen beim Durchgang durch Materie," *Annalen der Physik*, vol. 408, no. 3, pp. 285–320, Jan. 1933.
[70] H. Bethe, "Zur Theorie des Durchgangs schneller Korpuskularstrahlen durch Materie," *Annalen der Physik*, vol. 397, no. 3, pp. 325–400, Jan. 1930.
[71] J. F. Ziegler, M. D. Ziegler, and J. P. Biersack, "SRIM - The stopping and range of ions in matter (2010)," *Nuclear Instruments and Methods in Physics Research Section B: Beam Interactions with Materials and Atoms*, vol. 268, no. 11–12, pp. 1818–1823, Jun. 2010.
[72] R. Spohr and K. Bethge, *Ion Tracks and Microtechnology: Principles and Applications*, 1. ed. Wiesbaden: Vieweg, 1990.
[73] G. Schiwietz, E. Luderer, G. Xiao, and P. L. Grande, "Energy dissipation of fast heavy ions in matter," *Nuclear Instruments and Methods in Physics Research Section B: Beam Interactions with Materials and Atoms*, vol. 175–177, pp. 1–11, Apr. 2001.
[74] P. Sigmund, "Ion Beam Science: Solved and Unsolved Problems," *Mat. Fys. Med.*, vol. 52, no. 2, pp. 557–594, 2006.
[75] J. Schou, "Transport theory for kinetic emission of secondary electrons from solids," *Phys. Rev. B*, vol. 22, no. 5, p. 2141, 1980.
[76] R. Katz, F. A. Cucinotta, and C. X. Zhang, "The calculation of radial dose from heavy ions: predictions of biological action cross sections," *Nuclear Instruments and Methods in Physics Research Section B: Beam Interactions with Materials and Atoms*, vol. 107, no. 1–4, pp. 287–291, Feb. 1996.
[77] L. T. Chadderton, S. A. Cruz, and D. W. Fink, "Theory for latent particle tracks in polymers," *Nuclear Tracks and Radiation Measurements*, vol. 22, no. 1–4, pp. 29–38, 1993.
[78] E. H. Lee, "Ion-beam modification of polymeric materials - fundamental principles and applications," *Nuclear Instruments and Methods in Physics Research Section B: Beam Interactions with Materials and Atoms*, vol. 151, no. 1–4, pp. 29–41, May 1999.
[79] R. L. Fleischer, P. B. Price, and R. M. Walker, "Ion Explosion Spike Mechanism for Formation of Charged-Particle Tracks in Solids," *Journal of Applied Physics*, vol. 36, no. 11, pp. 3645–3652, Nov. 1965.
[80] S. Klaumünzer, M. Hou, and G. Schumacher, "Coulomb Explosions in a Metallic Glass Due to the Passage of Fast Heavy Ions?," *Phys. Rev. Lett.*, vol. 57, no. 7, p. 850, 1986.
[81] R. L. Fleischer, P. B. Price, and R. M. Walker, *Nuclear Tracks in Solids. Principles & Applications*. University of California Press, 1975.
[82] M. Toulemonde, W. Assmann, C. Dufour, F. Studer, and C. Trautmann, "Experimental Phenomena and Thermal Spike Model Description of Ion Tracks in Amorphisable Inorganic Insulators," in *Ion Beam Science: Solved and Unsolved Problems*, Copenhagen: , 2006.
[83] G. Szenes, "Thermal spike model of amorphous track formation in insulators irradiated by swift heavy ions," *Nuclear Instruments and Methods in Physics Research Section B: Beam Interactions with Materials and Atoms*, vol. 116, no. 1–4, pp. 141–144, Aug. 1996.
[84] G. Szenes, "Comparison of two thermal spike models for ion-solid interaction," *Nuclear Instruments and Methods in Physics Research Section B: Beam Interactions with Materials and Atoms*, vol. 269, no. 2, pp. 174–179, Jan. 2011.
[85] Y. Sun, Z. Zhu, Z. Wang, J. Liu, Y. Jin, M. Hou, Y. Wang, and J. Duan, "The damage process induced by swift heavy ion in polycarbonate," *Nuclear Instruments and Methods in Physics Research Section B: Beam Interactions with Materials and Atoms*, vol. 212, pp. 211–215, Dec. 2003.
[86] Y. Sun, C. Zhang, Z. Zhu, Z. Wang, Y. Jin, J. Liu, and Y. Wang, "The thermal-spike model description of the ion-irradiated polyimide," *Nuclear Instruments and Methods in Physics Research Section B: Beam Interactions with Materials and Atoms*, vol. 218, pp. 318–322, Jun. 2004.
[87] G. Szenes, K. Havancsák, V. Skuratov, P. Hanák, L. Zsoldos, and T. Ungár, "Application of the thermal spike model to latent tracks induced in polymers," *Nuclear Instruments and Methods in Physics Research Section B: Beam Interactions with Materials and Atoms*, vol. 166–167, pp. 933–937, May 2000.
[88] J. Gerhold, "Properties of cryogenic insulants," *Cryogenics*, vol. 38, no. 11, pp. 1063–1081, Nov. 1998.
[89] D. Evans, "Turn, layer and ground insulation for superconducting magnets," *Physica C: Superconductivity*, vol. 354, no. 1–4, pp. 136–142, May 2001.
[90] M. Ieda, "Dielectric Breakdown Process of Polymers," *IEEE Transactions on Electrical Insulation*, vol. EI-15, no. 3, pp. 206–224, Jun. 1980.
[91] Weijun Yin and D. Schweickart, "Dielectric breakdown of polymeric insulation films under AC, DC and pulsed voltages," in *IEEE Electrical Insulation Conference, 2009. EIC 2009*, 2009, pp. 292–296.
[92] T. J. Lewis, "The Role of Electrodes in Conduction and Breakdown Phenomena in Solid Dielectrics," *IEEE Transactions on Electrical Insulation*, vol. EI-19, no. 3, pp. 210–216, Jun. 1984.
[93] K. Kimura and Y. Kaneda, "The role of microscopic defects in multistress aging phenomena of micaceous insulation," *Conference Record of the 1994 IEEE International Symposium on Electrical Insulation*, pp. 257–260, 1994.
[94] K. Kimura and Y. Kaneda, "The role of microscopic defects in multistress aging of micaceous insulation," *IEEE Transactions on Dielectrics and Electrical Insulation*, vol. 2, no. 3, pp. 426–432, Jun. 1995.
[95] Y. Shibuya, S. Zoledziowski, and J. H. Calderwood, "Void formation and electrical breakdown in epoxy resin," *IEEE Transactions on Power Apparatus and Systems*, vol. 96, no. 1, pp. 198–207, 1977.
[96] R. Vogelsang, T. Weiers, K. Frohlich, and R. Brutsh, "Electrical breakdown in high-voltage winding insulations of different manufacturing qualities," *IEEE Electrical Insulation Magazine*, vol. 22, no. 3, pp. 5–12, 2006.
[97] V.-D. Nguyen, J.-M. Joung, S.-M. Baek, C.-H. Lee, and S.-H. Kim, "Aging characteristics of cryogenic insulator for development of HTS transformer," *Cryogenics*, vol. 45, no. 1, pp. 57–63, Jan. 2005.
[98] P. Bjellheim and B. Helgee, "Aromatic polyimides: Synthesis, characterization, and evaluation of electric strength," *Journal of Applied Polymer Science*, vol. 48, no. 9, pp. 1587–1596, Jun. 1993.

[99] J. B. Schutz, P. E. Fabian, C. S. Hazelton, T. S. Bauer-McDaniel, and R. P. Reed, “Effects of cryogenic irradiation on electrical strength of candidate ITER insulation materials,” *Cryogenics*, vol. 35, no. 11, pp. 759–762, Nov. 1995.
[100] J. Bobo, M. Perrier, B. Fallou, and J. Galand, “Dielectric strength of polymers at cryogenic temperatures under vacuum,” *Vacuum*, vol. 18, no. 7, pp. 397–401, Jul. 1968.
[101] S. Nishijima and M. Hara, “Mechanical influence on long-term dielectric performance of insulants,” *Cryogenics*, vol. 38, no. 11, pp. 1105–1113, Nov. 1998.
[102] K. Wu, Y. Wang, Y. Cheng, L. A. Dissado, and X. Liu, “Statistical behavior of electrical breakdown in insulating polymers,” *Journal of Applied Physics*, vol. 107, no. 6, pp. 064107–064107–5, Mar. 2010.
[103] S. Okabe, N. Hayakawa, H. Murase, H. Hama, and H. Okubo, “Common insulating properties in insulating materials,” *Dielectrics and Electrical Insulation, IEEE Transactions on*, vol. 13, no. 2, pp. 327 –335, Apr. 2006.
[104] R. B. Abernethy, J. E. Breneman, C. H. Medlin, and G. L. Reinman, *Weibull Analysis Handbook*. California: Pratt & Whitney Aircraft, 1983.
[105] B. Dodson, *The Weibull Analysis Handbook*, Second edition. Milwaukee: American Society of Quality Press, 2006.
[106] K. Eiermann, “Modellmäßige Deutung der Wärmeleitfähigkeit von Hochpolymeren,” *Colloid & Polymer Science*, vol. 198, no. 1, pp. 5–16, 1964.
[107] K. Eiermann, “Bestimmung der Temperaturabhängigkeit des Kristallisationsgrades aus der Wärmeleitfähigkeit,” *Colloid & Polymer Science*, vol. 198, no. 1, pp. 96–98, 1964.
[108] K. Eiermann, “Modellmäßige Deutung der Wärmeleitfähigkeit von Hochpolymeren,” *Colloid & Polymer Science*, vol. 199, no. 2, pp. 125–128, 1964.
[109] K. Eiermann, “Modellmäßige Deutung der Wärmeleitfähigkeit von Hochpolymeren,” *Colloid & Polymer Science*, vol. 201, no. 1, pp. 3–15, 1965.
[110] C. L. Choy and K. Young, “Thermal conductivity of semicrystalline polymers — a model,” *Polymer*, vol. 18, no. 8, pp. 769–776, Aug. 1977.
[111] O. Yano and H. Yamaoka, “Cryogenic properties of polymers,” *Progress in Polymer Science*, vol. 20, no. 4, pp. 585–613, 1995.
[112] M. Barucci, E. Olivieri, E. Pasca, L. Risegari, and G. Ventura, “Thermal conductivity of Torlon between 4.2 and 300 K,” *Cryogenics*, vol. 45, no. 4, pp. 295–299, Apr. 2005.
[113] J. J. Freeman and A. C. Anderson, “Thermal conductivity of amorphous solids,” *Physical review. B, Condensed matter*, vol. 34, no. 8, pp. 5684–5690.
[114] G. J. Morgan and D. Smith, “Thermal conduction in glasses and polymers at low temperatures,” *Journal of Physics C: Solid State Physics*, vol. 7, no. 4, pp. 649–664, Feb. 1974.
[115] L. Risegari, M. Barucci, E. Olivieri, E. Pasca, and G. Ventura, “Very-low-temperature thermal conductivity of polymeric supports for massive cryogenic detectors,” in *Astroparticle, Particle And Space Physics, Detectors And Medical Physics Applications*, Como, 2004, pp. 603–607.
[116] T. Horiuchi and T. Ooi, “Cryogenic properties of composite materials,” *Cryogenics*, vol. 35, no. 11, pp. 677–679, Nov. 1995.
[117] G. Hartwig and S. Knaak, “Fibre-epoxy composites at low temperatures,” *Cryogenics*, vol. 24, no. 11, pp. 639–647, Nov. 1984.
[118] F. Pobell, *Matter and Methods at Low Temperatures*. Springer, 2007.
[119] H. Ishida, S. T. Wellinghoff, E. Baer, and J. L. Koenig, “Spectroscopic Studies of Poly[N,N’-bis(phenoxyphenyl)pyromellitimide]. 1. Structures of the Polyimide and Three Model Compounds,” *Macromolecules*, vol. 13, no. 4, pp. 826–834, Jul. 1980.
[120] D. Severin, W. Ensinger, R. Neumann, C. Trautmann, G. Walter, I. Alig, and S. Dudkin, “Degradation of polyimide under irradiation with swift heavy ions,” *Nuclear Instruments and Methods in Physics Research Section B: Beam Interactions with Materials and Atoms*, vol. 236, no. 1–4, pp. 456–460, Jul. 2005.
[121] G. Compagnini, G. Foti, R. Reitano, and G. Mondio, “Graphitic clusters in hydrogenated amorphous carbon induced by keV-ion irradiation,” *Applied Physics Letters*, vol. 57, no. 24, pp. 2546–2548, Dec. 1990.
[122] S. Shukushima, S. Nishikawa, Y. Matsumoto, and Y. Hibino, “Ion beam modification of aromatic polymers,” *Nuclear Instruments and Methods in Physics Research Section B: Beam Interactions with Materials and Atoms*, vol. 80–81, Part 2, no. 0, pp. 1119–1122, 1993.
[123] D. I. Bower and W. F. Maddams, *The vibrational spectroscopy of polymers*, 1st ed. Cambridge, Great Britain: Cambridge University Press, 1989.
[124] M. Hesse, H. Meier, and B. Zeeh, *Spektroskopische Methoden in der organischen Chemie*, 7., überarbeitete Auflage. Stuttgart: Thieme, 2011.
[125] J. Fahrenfort, “Attenuated total reflection: A new principle for the production of useful infra-red reflection spectra of organic compounds,” *Spectrochimica Acta*, vol. 17, no. 7, pp. 698–709, 1961.
[126] T. Matsuo, “Carbonyl Absorption Bands in the Infrared Spectra of Some Cyclic Imides with a Five-membered Ring,” *Bull. Chem. Sac. Jpn.*, vol. 37, no. 12, pp. 1844–1848, 1964.
[127] R. J. Angelo, R. C. Golike, W. E. Tatum, and J. A. Kreuz, in *Proc. of sec. intern. conf. of polyimides*, Ellenville, NY, 1985, pp. 631–667.
[128] H. Ishida and M. T. Huang, “Infrared spectral assignments for a semicrystalline thermoplastic polyimide,” *Spectrochimica Acta Part A: Molecular and Biomolecular Spectroscopy*, vol. 51, no. 3, pp. 319–331, Mar. 1995.
[129] S. T. Wellinghoff, H. Ishida, J. L. Koenig, and E. Baer, “Spectroscopic Studies of Poly[N,N’-bis(phenoxyphenyl)pyromellitimide]. 2. Structural Changes of Polyimide upon Yielding,” *Macromolecules*, vol. 13, no. 4, pp. 834–839, Jul. 1980.
[130] G. Guerra, S. Choe, D. J. Williams, F. E. Karasz, and W. J. MacKnight, “Fourier transform infrared spectroscopy of some miscible polybenzimidazole/polyimide blends,” *Macromolecules*, vol. 21, no. 1, pp. 231–234, Jan. 1988.
[131] I. Karamancheva, V. Stefov, B. Å optrajanov, G. Danev, E. Spasova, and J. Assa, “FTIR spectroscopy and FTIR microscopy of vacuum-evaporated polyimide thin films,” *Vibrational Spectroscopy*, vol. 19, no. 2, pp. 369–374, Apr. 1999.
[132] E. Spassova, “Vacuum deposited polyimide thin films,” *Vacuum*, vol. 70, no. 4, pp. 551–561, Apr. 2003.
[133] C. A. Pryde, “IR studies of polyimides. I. Effects of chemical and physical changes during cure,” *Journal of Polymer Science Part A: Polymer Chemistry*, vol. 27, no. 2, pp. 711–724, Jan. 1989.

[134] K. Ha and J. L. West, “Studies on the photodegradation of polarized UV-exposed PMDA–ODA polyimide films,” *Journal of Applied Polymer Science*, vol. 86, no. 12, pp. 3072–3077, 2002.
[135] H. B. Henbest and R. a. L. Wilson, “376. Aspects of stereochemistry. Part I. Stereospecificity in formation of epoxides from cyclic allylic alcohols,” *J. Chem. Soc.*, no. 0, pp. 1958–1965, Jan. 1957.
[136] R. N. O’Brien and K. Hartman, “Air infrared spectroscopy study of the epoxy-cellulose interface,” *Journal of Polymer Science Part C: Polymer Symposia*, vol. 34, no. 1, pp. 293–301, 1971.
[137] D. O. Hummel, *Atlas of polymer and plastics analysis. Vol. 2, Parts a/I and a/II*. Munich/Vienna/Weinheim/Basel: Carl Hanser Verlag, 1984.
[138] G. C. Stevens, “Cure kinetics of a low epoxide/hydroxyl group-ratio bisphenol a epoxy resin–anhydride system by infrared absorption spectroscopy,” *Journal of Applied Polymer Science*, vol. 26, no. 12, pp. 4259–4278, 1981.
[139] S. C. Lin, B. J. Bulkin, and E. M. Pearce, “Epoxy resins. III. Application of fourier transform IR to degradation studies of epoxy systems,” *Journal of Polymer Science: Polymer Chemistry Edition*, vol. 17, no. 10, pp. 3121–3148, 1979.
[140] J. Mijović and S. Andjelić, “Monitoring of reactive processing by remote mid infra-red spectroscopy,” *Polymer*, vol. 37, no. 8, pp. 1295–1303, Apr. 1996.
[141] F. J. Boerio and S. K. Bahl, “Vibrational analysis of aromatic esters,” *Spectrochimica Acta Part A: Molecular Spectroscopy*, vol. 32, no. 5, pp. 987–1006, 1976.
[142] H. Ishida and J. L. Koenig, “An investigation of the coupling agent/matrix interface of fiberglass reinforced plastics by fourier transform infrared spectroscopy,” *Journal of Polymer Science: Polymer Physics Edition*, vol. 17, no. 4, pp. 615–626, 1979.
[143] H. Ishida and J. L. Koenig, “The reinforcement mechanism of fiber-glass reinforced plastics under wet conditions: A review,” *Polymer Engineering & Science*, vol. 18, no. 2, pp. 128–145, 1978.
[144] H. Ishida and J. L. Koenig, “A fourier-transform infrared spectroscopic study of the hydrolytic stability of silane coupling agents on E-glass fibers,” *Journal of Polymer Science: Polymer Physics Edition*, vol. 18, no. 9, pp. 1931–1943, 1980.
[145] A. T. Dibenedetto and P. J. Lex, “Evaluation of surface treatments for glass fibers in composite materials,” *Polymer Engineering & Science*, vol. 29, no. 8, pp. 543–555, 1989.
[146] “Akadémiai Kiadó - Journal of Thermal Analysis and Calorimetry - Zeitschriftenbeitrag.” [Online]. Available: http://www.akademiai.com/content/j06km3u8j431x777/. [Accessed: 14-Nov-2011].
[147] M. B. Lewis and E. H. Lee, “Residual gas and ion-beam analysis of ion-irradiated polymers,” *Nuclear Instruments and Methods in Physics Research Section B: Beam Interactions with Materials and Atoms*, vol. 61, no. 4, pp. 457–465, Oct. 1991.
[148] A. Idesaki, N. Koizumi, M. Sugimoto, N. Morishita, T. Ohshima, K. Okuno, U. (Balu) Balachandran, K. Amm, D. Evans, E. Gregory, P. Lee, M. Osofsky, S. Pamidi, C. Park, J. Wu, and M. Sumption, “Gas evolution from insulating materials for sc coil of ITER by gamma ray irradiation at liquid nitrogen temperature,” 2008, vol. 986, pp. 169–173.
[149] Z. Chang and J. A. Laverne, “Dynamic evolution of gases in the γ- and helium-ion radiolyses of solid polymers,” *Journal of Polymer Science Part B: Polymer Physics*, vol. 39, no. 13, pp. 1449–1459, 2001.
[150] H. Lee, “Rapid measurement of thermal conductivity of polymer films,” *Rev. Sci. Instrum.*, vol. 53, no. 6, p. 884, 1982.
[151] R. Bachmann, “Heat Capacity Measurements on Small Samples at Low Temperatures,” *Review of Scientific Instruments*, vol. 43, p. 205, 1972.
[152] J. S. Hwang, K. J. Lin, and C. Tien, “Measurement of heat capacity by fitting the whole temperature response of a heat-pulse calorimeter,” *Review of Scientific Instruments*, vol. 68, p. 94, 1997.
[153] J. C. Lashley, M. F. Hundley, A. Migliori, J. L. Sarrao, P. G. Pagliuso, T. W. Darling, M. Jaime, J. C. Cooley, W. L. Hults, L. Morales, D. J. Thoma, J. L. Smith, J. Boerio-Goates, B. F. Woodfield, G. R. Stewart, R. A. Fisher, and N. E. Phillips, “Critical examination of heat capacity measurements made on a Quantum Design physical property measurement system,” *Cryogenics*, vol. 43, no. 6, pp. 369–378, Jun. 2003.
[154] “Kapton HN Datasheet,” *DuPont*, pp. 1–5, 2011.
[155] A. N. Hammoud, E. D. Baumann, E. Overton, I. T. Myers, J. L. Suthar, W. Khachen, and J. R. Laghari, “High temperature dielectric properties of Apical, Kapton, PEEK, Teflon AF, and Upilex polymers,” in *Conference on Electrical Insulation and Dielectric Phenomena, 1992. Annual Report*, 1992, pp. 549–554.
[156] “Using Excel for Weibull Analysis.” [Online]. Available: http://www.qualitydigest.com/jan99/html/body_weibull.html. [Accessed: 20-Jun-2012].
[157] “Institute for Theoretical and Experimental Physics.” [Online]. Available: http://www.itep.ru/eng/in_eng.shtml. [Accessed: 07-Mar-2011].
[158] “GSI - Linearbeschleuniger.” [Online]. Available: http://www.gsi.de/forschung_beschleuniger/beschleunigeranlage/linearbeschleuniger.htm. [Accessed: 25-Jun-2012].
[159] P. Forck, “Lecture Notes on Beam Instrumentation and Diagnostics,” Darmstadt, Joint Universities Accelerator School, 2011.
[160] D. Severin, C. Trautmann, and R. Neumann, “The M-Branch, a new UNILAC irradiation facility with in-situ analytical techniques for materials research,” *GSI Scientific Report*, p. 362, 2008.
[161] S. Amirthapandian, F. Schuchart, and W. Bolse, “A high resolution scanning electron microscope for in situ investigation of swift heavy ion induced modification of solid surfaces,” *Review of Scientific Instruments*, vol. 81, p. 033702, 2010.
[162] O. Baake, T. Seidl, U. H. Hossain, A. O. Delgado, M. Bender, D. Severin, and W. Ensinger, “An apparatus for in situ spectroscopy of radiation damage of polymers by bombardment with high-energy heavy ions,” *Rev. Sci. Instrum.*, vol. 82, no. 4, p. 045103, 2011.
[163] E. Mustafin, E. Floch, A. B. Plotnikov, E. Schubert, and T. Seidl, “Irradiation of superconducting magnet components for FAIR,” presented at the Heavy Ion Accelerator Technology 2009, Venice, Italy, 2009.
[164] A. B. Plotnikov, E. Floch, E. Mustafin, E. Schubert, T. Seidl, and I. Strasík, “Preparation of the irradiation test at cave HHD of GSI Darmstadt,” presented at the Heavy Ion Accelerator Technology 2009, Venice, Italy.
[165] L. Latysheva, “Irradiation experiment in Cave HHD: Numerical estimates of the energy deposition into the samples,” GSI, Darmstadt, GSI-report DOC-2008-Nov-262-1, 2008.
[166] L. Latycheva, “Contribution of the secondary particles to the dose distribution in samples S1 and S8,” GSI, Darmstadt, GSI-report DOC-2009-Jan-47-1, 2009.

[167] B. Schuster, M. Lang, R. Klein, C. Trautmann, R. Neumann, and A. Benyagoub, “Structural phase transition in induced by swift heavy ion irradiation at high-pressure,” *Nuclear Instruments and Methods in Physics Research Section B: Beam Interactions with Materials and Atoms*, vol. 267, no. 6, pp. 964–968, Mar. 2009.
[168] T. Steckenreiter, E. Balanzat, H. Fuess, and C. Trautmann, “Chemical modifications of PET induced by swift heavy ions,” *Nuclear Instruments and Methods in Physics Research Section B: Beam Interactions with Materials and Atoms*, vol. 131, no. 1–4, pp. 159–166, Aug. 1997.
[169] H. A. Khan, N. A. Khan, K. Jamil, and R. Brandt, “Annealing of heavy ion latent damage trails in muscovite mica and CR-39 plastic track detectors,” *Nuclear Tracks and Radiation Measurements (1982)*, vol. 8, no. 1–4, pp. 377–380, 1984.
[170] J. D. Pinheiro Filho, A. X. Da Silva, and R. C. Santos, “Studies of isochronal and isothermal annealing of alpha particle tracks in CR-39 polymer detectors,” *Nuclear Instruments and Methods in Physics Research Section B: Beam Interactions with Materials and Atoms*, vol. 111, no. 1–2, pp. 104–110, Apr. 1996.
[171] D. Pacifici, E. C. Moreira, G. Franzò, V. Martorino, F. Priolo, and F. Iacona, “Defect production and annealing in ion-irradiated Si nanocrystals,” *Phys. Rev. B*, vol. 65, no. 14, p. 144109, Apr. 2002.
[172] Y. Q. Wang, L. B. Bridwell, R. E. Giedd, and M. J. Murphy, “Effects of dose rate on the electrical conductivity of ion implanted polymers,” *Nuclear Instruments and Methods in Physics Research Section B: Beam Interactions with Materials and Atoms*, vol. 56–57, Part 1, no. 0, pp. 660–663, May 1991.
[173] M. L. Kaplan, S. R. Forrest, P. H. Schmidt, and T. Venkatesan, “Optical and electrical properties of ion-beam-irradiated films of organic molecular solids and polymers,” *Journal of Applied Physics*, vol. 55, no. 3, pp. 732–742, Feb. 1984.
[174] S. Baccaro, B. Caccia, S. Onori, and M. Pantaloni, “The influence of dose rate and oxygen on the irradiation induced degradation in ethylene-propylene rubber,” *Nuclear Instruments and Methods in Physics Research Section B: Beam Interactions with Materials and Atoms*, vol. 105, no. 1–4, pp. 97–99, Nov. 1995.
[175] D. Erskine, P. Y. Yu, S. C. Freilich, D. Erskine, P. Y. Yu, and S. C. Freilich, “High pressure visible spectroscopy of polyimide film,” *Journal of Polymer Science Part C: Polymer Letters*, vol. 26, 26, no. 11, 11, pp. 465, 465–468, 468, Oct. 1988.
[176] S. Ando, T. Matsuura, and S. Sasaki, “Coloration of Aromatic Polyimides and Electronic Properties of Their Source Materials,” *Polymer Journal*, vol. 29, no. 1, pp. 69–76, 1997.
[177] T. Matsumoto, D. Mikami, T. Hashimoto, M. Kaise, R. Takahashi, and S. Kawabata, “Alicyclic polyimides – a colorless and thermally stable polymer for opto-electronic devices,” *Journal of Physics: Conference Series*, vol. APCTP–ASEAN Workshop on Advanced Materials Science and Nanotechnology, no. 187, pp. 1–11, 2009.
[178] K. Abe, C. M. Logan, K. Saneyoshi, and F. W. Clinard Jr, “Irradiation Effects in KAPTON Polyimide Film From 14 MeV Neutrons and Cobalt-60 Gamma Rays,” *Influence of Radiation on Material Properties: 13th International Symposium. II*, pp. 669–681, 1987.
[179] J. Davenas, X. L. Xu, G. Boiteux, and D. Sage, “Relation between structure and electronic properties of ion irradiated polymers,” *Nuclear Instruments and Methods in Physics Research Section B: Beam Interactions with Materials and Atoms*, vol. 39, no. 1–4, pp. 754–763, Mar. 1989.
[180] J. Davenas and P. Thevenard, “Electronic structure characterization of ion beam modified polyimide by optical absorption and reflection,” *Nuclear Instruments and Methods in Physics Research Section B: Beam Interactions with Materials and Atoms*, vol. 59–60, Part 2, no. 0, pp. 1249–1252, Jul. 1991.
[181] H. Virk, P. Chandi, and A. Srivastava, “Physical and chemical response of 70 MeV carbon ion irradiated Kapton-H polymer,” *Bulletin of Materials Science*, vol. 24, no. 5, pp. 529–534, 2001.
[182] C. Kim, K. Hakamada, and M. Endo, “Raman spectroscopy of Kapton-derived carbon film,” *Carbon*, vol. 36, no. 9, pp. 1401–1403, Sep. 1998.
[183] M. A. Alexander, D. J. T. Hill, J. W. Connell, and K. A. Watson, “A Study of the Oxidation of Two Aromatic Polyimide Fluoropolymers Containing Phenylphosphine Oxide by a Water Plasma and γ-Radiolysis in Air,” *High Performance Polymers*, vol. 13, no. 1, pp. 55–65, Jan. 2001.
[184] T. Steckenreiter, E. Balanzat, H. Fuess, and C. Trautmann, “Chemical degradation of polyimide and polysulfone films under the irradiation with heavy ions of several hundred MeV,” *Journal of Polymer Science Part A: Polymer Chemistry*, vol. 37, no. 23, pp. 4318–4329, 1999.
[185] D. Severin, E. Balanzat, W. Ensinger, and C. Trautmann, “Outgassing and degradation of polyimide induced by swift heavy ion irradiation at cryogenic temperature,” *Journal of Applied Physics*, vol. 108, no. 2, pp. 024901–024901–5, Jul. 2010.
[186] H. Hatori, Y. Yamada, M. Shiraishi, M. Yoshihara, and T. Kimura, “The mechanism of polyimide pyrolysis in the early stage,” *Carbon*, vol. 34, no. 2, pp. 201–208, 1996.
[187] T. Feurer, R. Sauerbrey, M. C. Smayling, and B. J. Story, “Ultraviolet-laser-induced permanent electrical conductivity in polyimide,” *Applied Physics A: Materials Science & Processing*, vol. 56, no. 3, pp. 275–281, 1993.
[188] N. Arnold and N. Bityurin, “Model for laser-induced thermal degradation and ablation of polymers,” *Applied Physics A: Materials Science & Processing*, vol. 68, no. 6, pp. 615–625, 1999.
[189] V. Picq and E. Balanzat, “Ion-induced molecular emission of polymers: analytical potentialities of FTIR and mass spectroscopy,” *Nuclear Instruments and Methods in Physics Research Section B: Beam Interactions with Materials and Atoms*, vol. 151, no. 1–4, pp. 76–83, May 1999.
[190] R. Mishra, S. P. Tripathy, D. Fink, and K. K. Dwivedi, “Activation energy of thermal decomposition of proton irradiated polymers,” *Radiation Measurements*, vol. 40, no. 2–6, pp. 754–757, Nov. 2005.
[191] R. Mishra, S. P. Tripathy, K. K. Dwivedi, D. T. Khathing, S. Ghosh, and D. Fink, “Dose-dependent modification in makrofol-N and polyimide by proton irradiation,” *Radiation Measurements*, vol. 36, no. 1–6, pp. 719–722, Jun. 2003.
[192] R. Mishra, S. P. Tripathy, K. K. Dwivedi, D. T. Khathing, S. Ghosh, M. Müller, and D. Fink, “Spectroscopic and thermal studies of electron irradiated polyimide,” *Radiation Measurements*, vol. 36, no. 1–6, pp. 621–624, Jun. 2003.
[193] D. W. Krevelen, *Properties of Polymers*. Amsterdam: Elsevier, 1990.
[194] G. Blyholder and H. Eyring, “Kinetics of Graphite Oxidation,” *J. Phys. Chem.*, vol. 61, no. 5, pp. 682–688, 1957.
[195] E. Jakab and M. Blazsó, “The effect of carbon black on the thermal decomposition of vinyl polymers,” *Journal of Analytical and Applied Pyrolysis*, vol. 64, no. 2, pp. 263–277, Sep. 2002.
[196] T. Steckenreiter, E. Balanzat, H. Fuess, and C. Trautmann, “Pyrolytic effects induced by energetic ions in polymers,” *Nuclear Instruments and Methods in Physics Research Section B: Beam Interactions with Materials and Atoms*, vol. 151, no. 1–4, pp. 161–168, May 1999.

[197] O. Baake, T. Seidl, U. H. Hossain, A. O. Delgado, M. Bender, D. Severin, and W. Ensinger, “An apparatus for in situ spectroscopy of radiation damage of polymers by bombardment with high-energy heavy ions,” *Review of Scientific Instruments*, vol. 82, p. 045103, 2011.
[198] G. F. L. Ehlers, K. R. Fisch, and W. R. Powell, “Thermal degradation of polymers with phenylene units in the chain. IV. Aromatic polyamides and polyimides,” *Journal of Polymer Science Part A-1: Polymer Chemistry*, vol. 8, no. 12, pp. 3511–3527, 1970.
[199] M. Statheropoulos and S. A. Kyriakou, “Quantitative thermogravimetric-mass spectrometric analysis for monitoring the effects of fire retardants on cellulose pyrolysis,” *Analytica Chimica Acta*, vol. 409, no. 1–2, pp. 203–214, Mar. 2000.
[200] U. Lappan, U. Geißler, L. Häußler, D. Jehnichen, G. Pompe, and K. Lunkwitz, “Radiation-induced branching and crosslinking of poly(tetrafluoroethylene) (PTFE),” *Nuclear Instruments and Methods in Physics Research Section B: Beam Interactions with Materials and Atoms*, vol. 185, no. 1–4, pp. 178–183, Dec. 2001.
[201] K. Humer, H. W. Weber, R. Hastik, H. Hauser, and H. Gerstenberg, “Dielectric strength of irradiated fiber reinforced plastics,” *Physica C: Superconductivity*, vol. 354, no. 1–4, pp. 143–147, May 2001.
[202] T. Seidl, A. Plotnikov, E. Mustafin, R. Lopez, D. Severin, E. Floch, C. Trautmann, A. Golubev, A. Smolyakov, D. Tommasini, and W. Ensinger, “Influence of swift heavy ion beams and protons on the dielectric strength of polyimide,” *Polymer Degradation and Stability*, vol. 97, no. 11, pp. 2396–2402, Nov. 2012.
[203] D. Fink, *Fundamentals of Ion Irradiated Polymers*. Berlin/Heidelberg: Springer, 2004.
[204] P. G.C., “Hopping conductivity in polymer matrix–metal particles composites,” *Composites Part A: Applied Science and Manufacturing*, vol. 37, no. 10, pp. 1545–1553, Oct. 2006.
[205] J. Feng and C. Chan, “Carbon black–filled immiscible blends of poly(vinylidene fluoride) and high density polyethylene: Electrical properties and morphology,” *Polymer Engineering & Science*, vol. 38, no. 10, pp. 1649–1657, Oct. 1998.
[206] X.-L. Xie, Y.-W. Mai, and X.-P. Zhou, “Dispersion and alignment of carbon nanotubes in polymer matrix: A review,” *Materials Science and Engineering: R: Reports*, vol. 49, no. 4, pp. 89–112, May 2005.
[207] J. Krauser, J.-H. Zollondz, A. Weidinger, and C. Trautmann, “Conductivity of nanometer-sized ion tracks in diamond-like carbon films,” *Journal of Applied Physics*, vol. 94, p. 1959, 2003.
[208] M. Barucci, E. Gottardi, I. Peroni, and G. Ventura, “Low temperature thermal conductivity of Kapton and Upilex,” *Cryogenics*, vol. 40, no. 2, pp. 145–147, Feb. 2000.
[209] B. Baudouy, “Kapitza resistance and thermal conductivity of Kapton in superfluid helium,” *Cryogenics*, vol. 43, no. 12, pp. 667–672, Dec. 2003.
[210] D. . Benford, T. . Powers, and S. . Moseley, “Thermal conductivity of Kapton tape,” *Cryogenics*, vol. 39, no. 1, pp. 93–95, Jan. 1999.
[211] J. Lawrence, A. . Patel, and J. . Brisson, “The thermal conductivity of Kapton HN between 0.5 and 5 K,” *Cryogenics*, vol. 40, no. 3, pp. 203–207, Mar. 2000.
[212] H. Yokoyama, “Thermal conductivity of polyimide film at cryogenic temperature,” *Cryogenics*, vol. 35, no. 11, pp. 799–800, Nov. 1995.
[213] D. L. Rule, D. R. Smith, and L. L. Sparks, “Thermal conductivity of polypyromellitimide film with alumina filler particles from 4.2 to 300 K,” *Cryogenics*, vol. 36, no. 4, pp. 283–290, Apr. 1996.
[214] B. A. Briskman, “Thermophysical Properties of Irradiated Polymers,” *Russian Chemical Reviews*, vol. 52, no. 5, pp. 469–483, May 1983.
[215] B. A. Briskman, “Radiation effects in thermal properties of polymers. An analytical review. I. Polyethylene,” *Nuclear Instruments and Methods in Physics Research Section B: Beam Interactions with Materials and Atoms*, vol. 185, no. 1–4, pp. 116–122, Dec. 2001.
[216] A. W. Smith and N. S. Rasor, “Observed Dependence of the Low-Temperature Thermal and Electrical Conductivity of Graphite on Temperature, Type, Neutron Irradiation, and Bromination,” *Phys. Rev.*, vol. 104, no. 4, pp. 885–891, Nov. 1956.
[217] D. O. Edwards, R. E. Sarwinski, P. Seligmann, and J. T. Tough, “The thermal conductivity of AGOT graphite between 0·3 and 3 K,” *Cryogenics*, vol. 8, no. 6, pp. 392–393, Dec. 1968.
[218] A. L. Woodcraft, M. Barucci, P. R. Hastings, L. Lolli, V. Martelli, L. Risegari, and G. Ventura, “Thermal conductivity measurements of pitch-bonded graphites at millikelvin temperatures: Finding a replacement for AGOT graphite,” *Cryogenics*, vol. 49, no. 5, pp. 159–164, May 2009.
[219] L. Calcagno, G. Compagnini, and G. Foti, “Structural modification of polymer films by ion irradiation,” *Nuclear Instruments and Methods in Physics Research Section B: Beam Interactions with Materials and Atoms*, vol. 65, no. 1–4, pp. 413–422, Mar. 1992.
[220] “cryogenic material properties Polyimide (Kapton).” [Online]. Available: http://www.cryogenics.nist.gov/MPropsMAY/Polyimide%20Kapton/PolyimideKapton_rev.htm. [Accessed: 19-Jul-2012].
[221] V. Zubko, “Low temperature specific heat, private communication,” IHEP, 2010.
[222] “Thermal and Mechanical Properties of Kapton.” [Online]. Available: http://www.yutopian.com/Yuan/prop/Kapton.html. [Accessed: 20-Jul-2012].
[223] E. Balanzat, N. Betz, and S. Bouffard, “Swift heavy ion modification of polymers,” *Nuclear Instruments and Methods in Physics Research Section B: Beam Interactions with Materials and Atoms*, vol. 105, no. 1–4, pp. 46–54, Nov. 1995.
[224] T. Steckenreiter, “Charakterisierung von Spuren energiereicher Ionen in Polymeren,” PhD thesis, Technische Universität Darmstadt, Darmstadt, Germany, 2007.
[225] A. Indarto, “Soot Growth Mechanisms from Polyynes,” *Environmental Engineering Science*, vol. 26, no. 12, pp. 1685–1691, Dec. 2009.
[226] A. V. Krestinin, “Detailed modeling of soot formation in hydrocarbon pyrolysis,” *Combustion and Flame*, vol. 121, no. 3, pp. 513–524, Mar. 2000.
[227] A. V. Krestinin, “Polyyne model of soot formation process,” *Symposium (International) on Combustion*, vol. 27, no. 1, pp. 1557–1563, 1998.
[228] E. Ziegler and H. Sterk, “Zur thermischen Bildung von Ketenen,” *Monatshefte für Chemie / Chemical Monthly*, vol. 99, no. 5, pp. 1958–1961, 1968.
[229] C.-K. Ni, E. A. Wade, M. V. Ashikhmin, and C. B. Moore, “Infrared Spectroscopy of Ketene by Two-Step Photodissociation,” *Journal of Molecular Spectroscopy*, vol. 177, no. 2, pp. 285–293, Jun. 1996.

[230] T. Seidl, “Abbau dünner Polyepoxid-Folien induziert durch Bestrahlung mit hochenergetischen Schwerionen,” Marburg, Diploma Thesis, 2007.
[231] C. A., “General consideration of the radiation chemistry of polymers,” *Nuclear Instruments and Methods in Physics Research Section B: Beam Interactions with Materials and Atoms*, vol. 105, no. 1–4, pp. 5–7, Nov. 1995.
[232] A. Chapiro, “Chemical modifications in irradiated polymers,” *Nuclear Instruments and Methods in Physics Research Section B: Beam Interactions with Materials and Atoms*, vol. 32, no. 1–4, pp. 111–114, May 1988.
[233] T. Seidl, O. Baake, U. H. Hossain, M. Bender, D. Severin, C. Trautmann, and W. Ensinger, “In-situ investigation of polyvinyl formal irradiated with GeV Au ions,” *Nuclear Instruments and Methods in Physics Research Section B: Beam Interactions with Materials and Atoms*, vol. 272, pp. 400–404, Feb. 2012.
[234] C. E. Klabunde and R. R. Coltman Jr., “Debonding of epoxy from glass in irradiated laminates,” *Journal of Nuclear Materials*, vol. 117, no. 0, pp. 345–350, Jul. 1983.
[235] M. B. Kasen, G. R. MacDonald, D. H. Beekman, and R. E. Schramm, “Mechanical, Electrical, and Thermal Characterization of G10CR and G11CR Glass-Cloth/Epoxy Laminates between Room Temperature and 4K,” NEMA D-1.
[236] R. P. Reed and M. Golda, “Cryogenic properties of unidirectional composites,” *Cryogenics*, vol. 34, no. 11, pp. 909–928, 1994.
[237] R. P. Reed and M. Golda, “Cryogenic composite supports: a review of strap and strut properties,” *Cryogenics*, vol. 37, no. 5, pp. 233–250, May 1997.
[238] Horizon Technologies, “Cryocomb Libraries,” *Cryodata*. www.htess.com, 1995.
[239] M. Wilson, *The QUENCH programm*. CERN/Geneva: Advanced Energy Analysis.
[240] J. P. L. Marquardt and R. Radebaugh, “Cryogenic Material Properties Database,” presented at the 11th International Cryocooler Conference, Keystone, Co, 2000.
[241] M. Jäckel, “Thermal properties of polymer/particle composites at low temperatures,” *Cryogenics*, vol. 35, no. 11, pp. 713–716, Nov. 1995.
[242] J. W. Davis and P. D. Smith, “ITER material properties handbook,” *Journal of Nuclear Materials*, vol. 233–237, Part 2, no. 0, pp. 1593–1596, Oct. 1996.
[243] V. I. Datskov and J. G. Weisend II, “Characteristics of russian carbon resistance (TVO) cryogenic thermometers,” *Cryogenics*, vol. 34, Supplement 1, no. 0, pp. 425–428, 1994.
[244] H. C. Meijer, R. W. Willekers, F. Mathu, H. Postma, L. H. Luthjens, and M. L. Hom, “Good performance of two kinds of cryogenic film-type thermometers after exposure to 107 Gy of ionizing radiation and in magnetic fields of up to 7 T at 4.2 K,” *Nuclear Instruments and Methods in Physics Research Section B: Beam Interactions with Materials and Atoms*, vol. 44, no. 2, pp. 159–165, Dec. 1989.
[245] Y. P. Filippov, V. M. Miklayev, and A. K. Sukhanova, “Irradiation of cryogenic temperature sensors by gamma dose of 1 MGy,” *Rev Sci Instrum*, vol. 78, no. 4, p. 043502, Apr. 2007.
[246] G. Heine and W. Lang, “Magnetoresistance of the new ceramic ‘Cernox’ thermometer from 4.2 K to 300 K in magnetic fields up to 13 T,” *Cryogenics*, vol. 38, no. 4, pp. 377–379, Apr. 1998.
[247] T. Barnett, Y. P. Filippov, E. Y. Filippova, N. V. Mokhov, N. Nakao, A. L. Klebaner, S. A. Korenev, J. C. Theilacker, J. Trenikhina, and K. Vaziri, “Radiation Requirements and Testing of Cryogenic Thermometers for the Ilc,” presented at the Advances in Cryogenic Engineering, 2008, vol. 985, pp. 973–980.
[248] J. Megusar, “Low temperature fast-neutron and gamma irradiation of Kapton® polyimide films,” *Journal of Nuclear Materials*, vol. 245, no. 2–3, pp. 185–190, Jun. 1997.
[249] T. Seguchi, K. Arakawa, M. Ito, N. Hayakawa, and S. Machi, “Radiation induced oxidative degradation of polymers—III: Effect of radiation on mechanical properties,” *Radiation Physics and Chemistry (1977)*, vol. 21, no. 6, pp. 495–501, 1983.

Acknowledgements

At this point I would like to thank all people who contributed to this work:

- Prof. Dr. W. Ensinger for the opportunity to perform this doctoral work under his supervision and his trustfulness and freedom of choice with respect to the scientific work, and all “gentleman agreements”.
- Prof. Dr. C. Trautmann from the GSI Helmholtz Center of Heavy Ion Research for the opportunity to be a permanent guest in the material research department of GSI, the many helpful scientific discussions and for acting as a referee in this dissertation.
- The BMBF for financing the biggest part of this work through the projects 05KK7RD1 and 06DA90251
- Dr. D. Severin for support and the introduction into the field during the beginning of my PhD.
- Dr. E. Mustafin, Dr. A. Plotnikov and E. Floch from the FAIR Theory and the Magnet Design group for support, interest and guidance concerning all FAIR relevant work.
- Dr. D. Tomassini and R. Lopez from CERN for discussions and the possibility of measuring the dielectric strength of polymers within their laboratory.
- Dr. T. Wietoska from the group of Prof. Dr. Hinrichsen (TU Darmstadt) for performing the dielectric strength measurements on non-irradiated and irradiated glass-fiber reinforced plastic samples.
- Dr. A. Golubev and A. Smolyakov from the ITEP in Russia for help during the proton beamtimes and hospitality during my stay in Moscow.
- Dr. M. Pavlovic from SUT Bratislava for the nice collaboration concerning radiation damage in FAIR relevant materials and the hospitality during my stay in Bratislava.
- Prof. Dr. Schneider and Dr. R. Hoffmann for the opportunity of the TG-MS measurements.
- Dr. S. Canfer from Rutherford Appleton Laboratories for discussions about radiation induced changes in composite materials and for TGA and DSC measurements.
- J. Tobisch from LOT GmbH and Prof. Dr. C. Felser from University of Mainz for the low temperature heat capacity measurements with their PPMS.
- B. Fischer and K.O. Voss for their versatile help especially about the construction of the low temperature thermal conductivity set up.
- M. Krause for the enormous help and being the best friend.
- Dr. B. Schuster, B. Merk and I. Alber for all the shared experiences, being best colleagues and back up during the whole PhD.
- The whole group of the Materials Research Department of GSI for the very pleasant working conditions and diverting coffee breaks.
- Prof. Dr. C. Roth, Dr. M. Rauber, F. Münch for the opportunity to participate in interesting interdisciplinary side projects.
- Prof. S. Katusic for motivating me to study chemistry and the support in all kind of chemical questions.
- Suzie for proofreading.
- Last but not least I would like to thank my partner M.G. Bernal Lujan, my family, and friends for their unrestricted support during all the time.